Modelling Benguela Niños using the Regional Oceanic Modelling System (ROMS)

Eurico Tiago Justino Queiroz

Submitted in partial fulfilment of the requirement for the degree of Master of Science.

August, 2007

Department of Oceanography

University of Cape Town

Abstract

This study is framed by three questions: firstly, could the Regional Oceanic Modelling System (ROMS) reproduce the seasonal cycle of the equatorial Atlantic? Secondly, what is the nature of the link between remote forcing in the western equatorial Atlantic and Benguela Niños/Niñas? Thirdly, what is the impact of these events on the equatorial Atlantic Ocean SST and circulation patterns?

The results obtained suggest that the model is very sensitive to different wind stress forcing, particularly in respect of the impact on the mixed layer characteristics. As a result the equatorial upwelling is overestimated in both temporal and spatial scales. The equatorial thermocline is reasonably reproduced by the model i.e., deeper in the western Atlantic (~110m) and shallower (~40m) in the eastern Atlantic. However, the thermocline depth is shallower (ERS CLIM) and deeper (COADS CLIM) than expected for each of the climatology wind forcing data. This constitutes further evidence of the model sensitivity to the vertical mixing scheme. The model outputs reveal that the equatorial Atlantic current system is reasonably reproduced in both ERS and COADS CLIM experiments. However, the model horizontal resolution (0.5°) and topography interpolation constrain the model accuracy resolving narrow coastal currents such as Angola Current (AC) and North Brazilian Current (NBC). The salinity field variability associated with the main river systems (Amazon and Congo River) is roughly reproduced by the model. Two factors influence the model salinity results: ROMS is not forced with river run off and the salinity field strongly depends on advection. Therefore, the inaccurate coastal currents will impact on the fresh plumes associated with the Amazon and Congo River.

To investigate the link between remote forcing and Benguela Niños/Niñas, sensitivity analyses were performed applying artificial wind stress anomalies to the ERS climatology. The wind stress anomalies were applied over the region off the Brazilian coast in the western Equatorial Atlantic. The results show that when the model was forced with artificial weaker winds (ERS WEAK) the model reproduces a strong subsurface positive temperature anomaly in the western Atlantic. Conversely, when an artificial strengthening was induced (ERS STRONG) the model reproduced subsurface negative temperature anomalies in the same region. The temperature anomalies propagate along the equator and as they reach the African coast they propagate southward and northward as far as the Angola-Benguela Front and Gulf of Guinea respectively. The impact of the artificial wind stress anomalies is also evident on the equatorial current system. The EUC and the central and north branches of the SEC transport undergo dramatic changes particularly in the region where the wind stress anomalies were applied. During the artificial weakening of the wind stress, the EUC and SEC show an abrupt transport reduction. In contrast, under artificial wind stress strengthening the EUC and SEC transport increase. The wind stress changes accelerate/reduce the surface current speed (SEC) and impact on the amount of water accumulated in the western Atlantic. Consequently, the eastward pressure gradient resulting from the water accumulation in the western Atlantic boundary impacts on the EUC transport, which is stronger or weaker for ERS STRONG and ERS WEAK, respectively. The model results also reveal a strengthening of the Angola Current one month after the artificial wind stress relaxation due to the baroclinic field adjustment.

The impact of the wind stress anomalies on the ocean temperature and circulation are consistent with previous studies showing that ROMS was able to reproduce artificially Benguela Niños/Niñas. The results support the remote forcing theory as the main driving force generating the Benguela Niños/Niñas and are a baseline for future ROMS simulations using realistic forcing fields.

KEY WORDS: Equatorial Atlantic, Angola Current, Angola-Benguela Frontal Zone (ABFZ), Benguela Niños/Niñas, Modeling,

Acknowledgments

I would like to express my gratitude to my supervisors Prof. frank Shillington, Dr. Pierre Florenchie and Dr. Pedro Monteiro for their support during this project. I am grateful to BCLME for the funding support and the opportunity given to me to join the regional scientific community.

I would like to thank to my family and friends back home for the unconditional support given when I decided to join this project. A final "big thank" to all the friends I made in Cape Town.

TABLE OF CONTENTS

List of Figures

Figure 5.6: Hoffmöller plot of the SSTs of a meridional section 30km offshore extending from 0 to 30°S for the period January 1982 to December 1999. Two isotherms – 16°C and 22°C – are overlaid (from Veitch *et al.*, 2006).

Figure 5.7: Averaged OI-SSTA over the ABFZ, between 14S-19°S, from 1982 to 2007. Red arrows highlight warm year events and blue arrows highlight cold year events (from BCLME State of the Ecosystem Information System (SEIS) website).

Figure 5.8: Composites of NOAA Extended SST anomalies in March for a) 1982, 1983, 1986/1987, 1991/1992 and 1997 cold events and b) 1934, 1949, 1963, 1984, 1986, 1995 and 2001 warm events *(http://www.cdc.noaa.gov).*

Figure 5.9: Vertical distribution of anomalies of (a) temperature and (b) salinity between March 1995 and March 1996 in a section parallel to the coast near the 100m isobath. Note the strong positive temperature anomalies from 14°S-20°S (from Gammelsrød *et al.*, 1998).

Figure 5.10: Maximized correlation between OI-SST anomalies averaged over the Angola Benguela Area (ABA) and ERS zonal winds anomalies over the South Atlantic for the period 1992 to 2000 (from Florenchie *et al.*, 2003).

Figure 5.11: Quikscat zonal wind anomaly averaged along the equator over the area 40°W-15°W and 2°N-2°S, from 1999 to 2007 (from BCLME State of the Ecosystem Information System (SEIS) website).

Figure 5.42: Upper panel illustrates the propagation of warm anomalies in January/February 1984 along the equator at 100, 75 and 45m depths. Bottom panel shows the warm anomaly signature along the African coast at 5, 25, 45 and 75m on 03/30/1984 (from Florenchie *et al.*, 2003).

Figure 5.13: Mechanism of surface warming vs. sub-thermocline poleward flow over the Namibian shelf. Left panel (a) shows the sub-thermocline flow response to a strong surface warming, both sub-thermocline poleward flows (over shelf and offshore) extend far south reaching the Luderitz upwelling system (Benguela Niño "death" scenario). Right panel (b) shows the opposite scenario, i.e. warm surface waters found north of Cape Frio, thus sub-thermocline poleward flows stop at Cape Frio region (Benguela Niña re-animation scenario) (courtesy of Dr. Pedro Monteiro).

Figure 5.17: Left: mean FMA SST anomalies for 1984 (a); 1986 (d) 1995 (g) and 2001 (j) contour at 0.5°C, 1.5°C and 2.5°C. Middle: mean FMA integrated moisture form the surface to 300 hPa flux anomalies for 1984 (b), 1986 (e) 1995 (h) and 2001 (k) in g/kg.m/s. Right: mean FMA rain rate normalized anomalies for 1984 (b), 1986 (f) 1995 (i) and 2001 (i) (from Rouault *et al.*, 2003).

Figure 5.5: Simulations domain and topography superimposed (colour bar).

Figure 5.6: Simulation domain. Shaded area highlights the area where the artificial anomalies were applied on the ERS climatology field. The colour gradient, brighter on the edges to darker on the centre, represents the way the artificial anomalies were applied allowing a smooth transition from the climatology values to the artificial values.

Figure 5.7: Diagram summarizing the three simulations settings evaluated using ERS climatology and artificial winds – years, artificial anomalies box, months and anomaly amplitude.

Table 4.21: Summary of the different simulation configurations and settings used to carry out the entire investigation.

Figure 4.1: a) COADS CLIM: Average kinetic energy over the entire domain (top panel) and surface kinetic energy (bottom panel), b) ERS CLIM: Average kinetic energy over the entire domain (top panel) and surface kinetic energy (bottom panel).

Figure 4.2: a) Sea Surface Temperature Annual mean; b) Sea Surface Temperature Standard Deviation. Top panel for COADS CLIM, middle panel for ERS CLIM and bottom panel for WOA01 (contour 0.5 *°C*).

Figure 4.3: Sea Surface Temperature seasonal mean a) JFM, b) AMJ, c) JAS and c) OND. Top panel for COADS CLIM, middle panel for ERS CLIM and bottom panel for WOA01 (contour 0.5 *°C*).

Figure 4.4: Vertical section of temperature along the equator, seasonal mean a) JFM, b) AMJ, c) JAS and d) OND. Top panel for COADS CLIM, middle panel for ERS CLIM and bottom panel for WOA01 (contour 20 *°C* isotherm).

Figure 4.5: Thermocline depth along the equator, seasonal mean a) JFM, b) AMJ, c) JAS and d) OND. Top panel for COADS CLIM, middle panel for ERS CLIM and bottom panel for WOA01 (contour 20 *°C* isotherm).

Figure 4.6: a) Surface Salinity Annual mean; b) Surface Salinity Standard Deviation. Top panel for COADS CLIM, middle panel for ERS CLIM and bottom panel for WOA01 (contour 0.5 *psu*).

Figure 4.7: Sea Surface Salinity seasonal mean, a) JFM, b) AMJ, c) JAS and c) OND. Top panel for COADS CLIM, middle panel for ERS CLIM and bottom panel for WOA01 (contour 0.5 *psu*).

Figure 4.8: Vertical section of salinity along the equator, seasonal mean: a) JFM, b) AMJ, c) JAS and d) OND. Top panel for COADS CLIM, middle panel for ERS CLIM and bottom panel for WOA01 (contour 0.5 *psu*).

Figure 4.9: Surface Velocity Annual mean quiver. Top panel for COADS CLIM, middle panel for ERS CLIM and bottom panel for Lumpkin 2005 drifter-derived climatology of Global Surface Currents (ms^{-1}). Shown are: North Equatorial Countercurrent (NECC), the Guinea Current (GC), the South Equatorial Current (SEC) with the northern (nSEC), central (cSEC) and southern branches (sSEC), the North Brazil Current (NBC), the Angola Current (AC).

Figure 4.10: Surface Velocity Annual mean contour. a) U component and b) V component. Top panel for COADS CLIM, middle panel for ERS CLIM and bottom panel for Lumpkin 2005 drifter-derived climatology of Global Surface Currents (contour interval $0.1ms^{-1}$, positive values correspond to eastward or northward flow).

Figure 4.11: a) Surface U component Standard Deviation; b) Surface V component Standard Deviation. Top panel for COADS CLIM, middle panel for ERS CLIM and bottom panel for Lumpkin 2005 drifter-derived climatology of Global Surface Currents (contour interval $0.1ms^{-1}$).

Figure 4.12: Surface U component seasonal mean, a) JFM, b) AMJ, c) JAS and d) OND. Top panel for COADS CLIM, middle panel for ERS CLIM and bottom panel for Lumpkin 2005 drifter-derived climatology of Global Surface Currents (contour interval $0.1ms^{-1}$, positive values correspond to eastward or northward flow).

Figure 4.13: Surface V component seasonal mean, a) JFM, b) AMJ , c) JAS and d) OND. Top panel for COADS CLIM, middle panel for ERS CLIM and bottom panel for Lumpkin 2005 drifter-derived

climatology of Global Surface Currents (contour interval 0.1ms^{-1}, positive values correspond to eastward or northward flow).

Figure 4.14: V component vertical section along 10S, seasonal mean, a) JFM, b) AMJ, c) JAS and d) OND. Top panel for COADS CLIM and bottom panel for ERS CLIM (contour interval 0.1ms^{-1}, positive values correspond to eastward flow). Shown are: Angola Current (AC).

Figure 4.15: Velocity quiver at 100m with U component superimposed, seasonal mean, a) JFM, b) AMJ, c) JAS and d) OND. Top panel for COADS CLIM and bottom panel for ERS CLIM (positive values correspond to eastward flow). Shown are: 1) Equatorial Undercurrent (EUC), 2) nSEC (north South Equatorial Current), 3) cSEC (central South Equatorial Current), 4) South Equatorial Undercurrent (SEUC) and 5) Gabon Current (GC).

Figure 4.16: U component vertical section along the equator, seasonal mean, a) JFM, b) AMJ, c) JAS and d) OND. Top panel for COADS CLIM and bottom panel for ERS CLIM (contour interval 0.1ms^{-1}, positive values correspond to eastward or northward flow).

Figure 4.17: U component vertical section along 30°W, seasonal mean, a) JFM, b) AMJ, c) JAS and d) OND. Top panel for COADS CLIM and bottom panel for ERS CLIM (contour interval 0.1ms^{-1}, positive values correspond to eastward flow). Shown are: Equatorial Undercurrent (EUC), North Equatorial Countercurrent (NECC), the South Equatorial Current (SEC) with the northern (nSEC) and southern branches (sSEC).

Figure 4.18: U component vertical section along 0E, seasonal mean, a) JFM, b) AMJ, c) JAS and d) OND. Top panel for COADS CLIM and bottom panel for ERS CLIM (contour interval 0.1ms^{-1}, positive values correspond to eastward flow). Shown are: Equatorial Undercurrent (EUC), Gabon Current (GC), the South Equatorial Current (SEC) with the northern (nSEC) and southern branches (sSEC) and the South Equatorial Undercurrent (SEUC).

Figure 4.19: Vertical section of the temperature along the equator, monthly mean a) Jan., b) Feb., c) March, d) April, e) May and f) June. Top panel for ERS CLIM, middle panel for ERS WEAK and bottom panel for ERS STRONG. Black arrows highlight the thermocline deepening or shallowing (contour 20°*C* isotherm).

Figure 4.20: Vertical section of the temperature along the equator, monthly anomaly from January to December. Top panel for ERS WEAK and bottom panel for ERS STRONG. (contour interval 1°*C*).

Figure 4.21: Temperature monthly mean anomaly averaged from surface to 100m depth from January to December. Top panel for ERS WEAK and bottom panel for ERS STRONG (contour interval 0.5°*C*).

Figure 4.22: Sea surface temperature monthly mean anomaly from January to December. Top panel for ERS WEAK and bottom panel for ERS STRONG (contour interval 0.5°*C*).

Figure 4.23: Sea surface salinity monthly mean anomaly from January to December. Top panel for ERS WEAK and bottom panel for ERS STRONG (contour interval 0.5 *psu*).

Figure 4.24: Surface U component monthly mean, a) January, b) February, c) March and d) April. Top panels for ERS CLIM, middle panels for ERS WEAK and bottom panels for ERS STRONG (contour interval 0.1ms^{-1}).

Figure 4.25: Surface Velocity monthly mean quiver from January to December. Top panels for ERS CLIM, middle panels for ERS WEAK and bottom panels for ERS STRONG (ms^{-1}).

Figure 4.26: V component vertical section along 10°S, monthly mean from January to December. Top panel for COADS CLIM and bottom panel for ERS CLIM (contour interval $0.1 ms^{-1}$, positive values correspond to eastward flow). Shown is: Angola Current (AC).

Figure 4.27: Zonal mean transport time series at 30°W, a) cSEC/nSEC and b) EUC.

Figure 4.28: Zonal mean transport time series at 30°W, a) cSEC/nSEC and b) EUC.

1 Introduction

Like the El Niños of the Pacific Ocean, Benguela Niños have a great social and economic impact on the Angola coast and on the coastal upwelling system of Namibia (Shannon *et al.*, 1986). It has therefore become desirable to understand and predict these events in order to develop contingency plans for the management of fisheries and water resources. Their impacts on biota and on the regional climate of the whole area are well documented (e.g., Shannon *et al.*, 1986; Boyer *et al.*, 2001; Rouault *et al.*, 2003; Monteiro *et al.*, 2004; Monteiro *et al.*, 2006). However, the processes driving Benguela Niños are still not fully understood, making prediction of these events difficult.

Benguela Niños result in intrusions of warm and saline waters of equatorial and tropical origins in the area of the Angola-Benguela Frontal Zone (e.g., Shannon *et al.*, 1986). These warm anomalies disrupt the Benguela upwelling system and induce a rapid decrease in fisheries as well as changes in inland rainfall patterns (e.g., Boyer *et al.*, 2001; Rouault *et al.*, 2003). Benguela Niños are also thought to be related to extremely hypoxic conditions on the Namibian shelf, which impacts on fish behaviour and mortally rate. However, this link still needs to be fully investigated (Monteiro *et al.*, 2004; Monteiro *et al.*, 2006; Monteiro and van der Plas, 2006).

Low oxygen water (LOW) in the Benguela system is an endemic and persistent phenomenon and its spatial distribution and time scales within the Benguela region have been addressed in different studies (Monteiro *et al.*, 2004; Monteiro *et al.*, 2006; Monteiro and van der Plas, 2006). There are two time scales affecting LOW in the

Benguela system: seasonal and interannual. The seasonal time scale is related to the seasonal relaxation of the trade winds over the eastern equatorial Atlantic, which enhances the Angola current, thereby advecting warm, saline and low oxygen waters of equatorial origin to the Benguela system (Monteiro *et al.*, 2004). The interannual time scale of LOW, characterized as extreme events of hypoxia and anoxia in the Benguela System are thought to be driven by Benguela Niños. In contrast with the seasonal time-scale events, Benguela Niños are thought to be triggered by a relaxation of the winds over the western Atlantic (Shannon et al., 1986; Carton and Huang, 1994; Gammelsrod et al., 1998; Florenchie et al., 2003, 2004). Although the forcing mechanisms driving the seasonal and interannual LOW events have different origins, their impacts are similar i.e., advection of warm, saline and low oxygen waters of equatorial origin to the Benguela system (Monteiro *et al.*, 2004).

The ability to predict Benguela Niños, in order to set up an early warning system for the Benguela region and to assure appropriate management strategies, requires an understanding of the mechanisms driving Benguela Niños and changes in circulation patterns during these events.

The first aim of this project is to assess the ability of the Regional Oceanic Modelling System (ROMS) to reproduce the seasonal cycle of the Equatorial Atlantic Ocean. The second objective is to investigate the equatorial remote forcing of Benguela Niños, i.e., the impact of changes in the trade winds over the western Atlantic, as well as the impact of this forcing on the Equatorial and Angola current systems. The following questions are addressed:

- Does ROMS reproduce the upper ocean Equatorial and South Atlantic climatology fields in a realistic way?
- Can wind stress anomalies over the western Atlantic trigger Benguela Niños?
- What are the impacts of Benguela Niños on the Equatorial and Angola current systems?
- Are there significant differences in the poleward transport of water masses along the African coast during Benguela Niño events?

A literature review regarding features within the Equatorial and South Atlantic atmospheric and oceanic circulation is found in **Chapter two**. It focuses on the mechanisms associated with Benguela Niños and their impacts on the Equatorial and eastern South Atlantic oceanic systems.

In **chapter three** the ROMS model and the different numerical model experiments are described, as well as the various observation datasets used to validate the model outputs. **Chapter four** comprises the results and discussion, and conclusions are provided in **Chapter five.**

2 Literature Review

2.1 South Atlantic Bathymetry

The South Atlantic Ocean lies between the continents of Africa and South America, and extends from the equator to the Antarctic region where an openings to the Pacific and Indian Oceans can be found. The basin is divided by the Mid-Atlantic Ridge, which reaches 1000m depth in some regions, thus strongly influencing bottom circulation (Tomczak and Godfrey, 2001).

The Brazil basin comprises most of the western part of the South Atlantic with depths exceeding 3000 meters. It extends meridionally from the equator to the Rio Grande Rise near 30°S, which rises to depths of 650m. However, west of the Rio Grande Rise, the Rio Grande Gap with depths exceeding 4000 meters, is a region of water mass exchange with the Argentinean Basin (south of Rio Grande Gap, not shown in **Figure 2.1**) (Reid *et al.*, 1977; Tomczak and Godfrey, 2001).

South of 25°S the South American continental shelf is considerably broad but narrows to a few kilometres in the north, contributing to the intensification of the North Brazil Current (NBC). North of 5°S the continental shelf becomes less steep and broad, and joins the equatorial region through the Romanche Fracture Zone. At depths of 4000-7500m, the Romanche Fracture Zone is the deepest area in the equatorial region and is the main water mass connecting the eastern and western Atlantic basin (Tomczak and Godfrey, 2001).

In the eastern Atlantic basin the Walvis ridge is the main topographic feature south of 20°S; it is north-east orientated and extends from the coast to as far as 30°S, rising to depths of 700m. The Walvis ridge divides the eastern basin into the Angola Basin (in the north) and the Cape Basin (in the south) and is a barrier for deep water mass flow. The Angola Basin occupies the largest and deepest area in the eastern basin, with depths reaching 5000m (Reid, 1989; Tomczak and Godfrey, 2001).

The African continental shelf is 150-200km wide between 32°S and 20°S. Between 20S-12°S it becomes narrow and steeper (20km) while north of 12°S it becomes progressively broader, having its maximum width at the Gulf of Guinea (Shannon and Nelson, 1996).

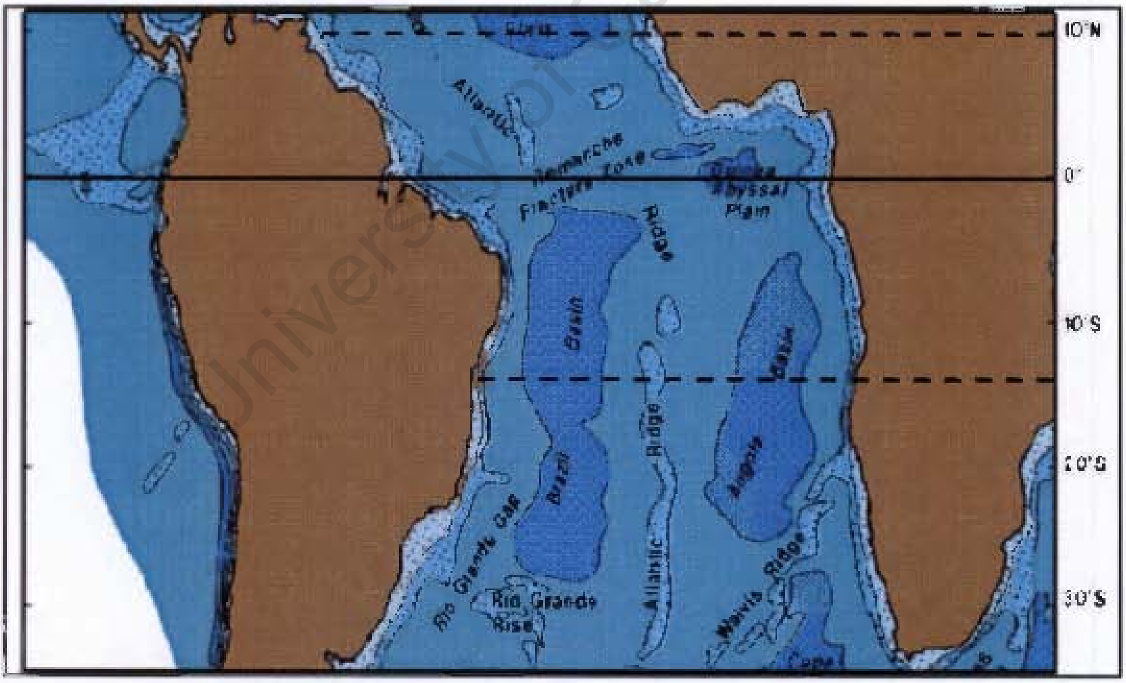

Figure 2.1: Topography of the South Atlantic Ocean. Dashed lines correspond to the model domain (10N-15°S). The 1000m, 3000m and 5000m isobaths are shown, and regions < 300m deep are shaded. (adapted from Tomczak and Godfrey, 2001).

2.2 *Atmospheric Elements*

The Intertropical Convergence Zone

The ocean-atmosphere coupled processes play key roles in determining oceanographic features of the South Atlantic Ocean. Hardman-Mountford *et al.* (2003) identified three main atmospheric circulation patterns and their interaction in the region: the Intertropical Convergence Zone (low pressure belt), the South Atlantic high-pressure system and the thermal low-pressure system over the African continent.

The semi-permanent South Atlantic high-pressure system (anticyclone) is centred around 32°S -5°W in the austral summer and 27°S-10°W in winter (Peterson and Stramma, 1991). Tyson (1986) (cited in Shannon and Nelson, 1996) reported seasonal latitudinal and longitudinal changes on the anticyclone position of 6° and 13° respectively (**Figure 2.2**). The position of the South Atlantic anticyclone is important as it will affect wind patterns of both the southern and Equatorial Atlantic region.

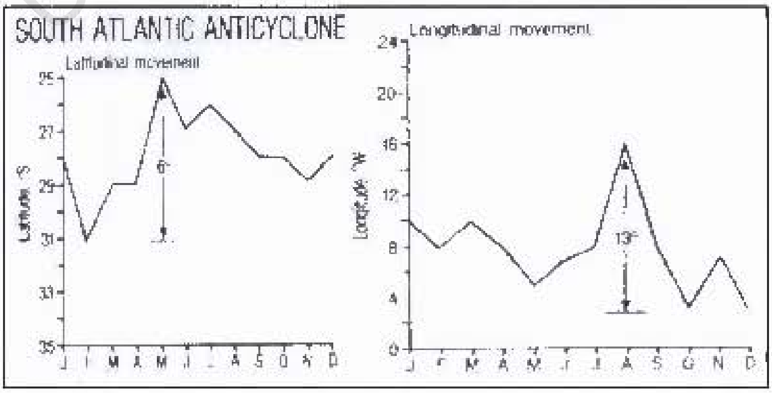

Figure 2.2: Annual variation in the position of the South Atlantic anticyclone (Peterson and Stramma, 1991).

During the austral summer, warming of African continent causes a strong thermal low-pressure system to develop (Shannon and Nelson, 1996). This seasonal low-pressure system interacts with the South Atlantic anticyclone. In its most southward position (during the austral summer) the South Atlantic anticyclone interacts with this seasonal low-pressure system, creating a strong pressure gradient. This in turn results in strong southerly winds along the south-west coast of Africa, which drives the upwelling system in the region (Peterson and Stramma, 1991; Shannon and Nelson, 1996).

The position of the South Atlantic anticyclone also modulates the strength and position of the equatorial trade winds and consequently the position of the Intertropical Convergence Zone (ICTZ) (e.g. Shannon and Nelson, 1996; Carton and Zhou, 1997). Since the South Atlantic cyclone is centred over the eastern basin, the trade winds near the African continent are generally stronger than in the western Atlantic basin (Peterson and Stramma, 1991). Furthermore, the ICTZ reaches its northern/southern-most position during the austral autumn/summer, coinciding with the northern/southern-most position of the South Atlantic anticyclone and strongest/weakest south-eastern trade winds. The seasonal meridional migration of the ITCZ as well as rainfall and SST are depicted in **Figure 2.3**.

Since the equatorial surface currents are mainly wind-driven, the seasonal variability of the ITCZ and trade winds have implications on the current system and also on the ocean heat content and storage patterns (Schott *et al.*., 2004, *CLIVAR panel white paper*). However, the atmospheric forcing on the Tropical Atlantic region shows different cycles, i.e., in the western Atlantic the dominant cycle is the annual cycle

(Stramma *et al.*, 2003), while in the central and eastern Atlantic a semi-annual cycle is the dominant mode (Philander and Pacanowski, 1986; Stramma *et al.*, 2003).

For instance, the seasonal time scale driving LOW in the eastern Atlantic (mentioned in **Chapter 1**) depends on the wind conditions over the eastern equatorial Atlantic, i.e. it is a combination of the strengthening (equatorial upwelling) and relaxation (carbon flux advection) of the trade winds over the eastern equatorial Atlantic.

The appearance of the North Equatorial Counter Current (NECC, eastward flow) is directly related to the northward migration of the ITCZ during the austral autumn (Stramma and Schott, 1999). Furthermore, Stramma *et al.* (2003) found that the strong signal in the annual cycle of the zonal velocity anomaly (ZVA) in the western Atlantic matched the signal of the NECC. However, no evidence was found that the ITCZ had a direct influence on the zonal field variability south of the equator. This result supports the findings from Merle and Arnault (1985) (cited in Veitch, 2004), who stated that the influence of the ITCZ in the south equatorial currents is felt as a remote response that manifests as local thermodynamic effects (Veitch, 2004).

The inter-decadal variability of the ITCZ complex is linked to interannual events on the south-eastern Africa coast, such as Benguela Niños (e.g., Philander, 1986; Shannon *et al.*, 1986, Florenchie *et al.*, 2003, 2004; Shillington *et al.*, 2006). A review of Benguela Niños, their sources and their impacts will be discussed in **Section 2.6** of this chapter.

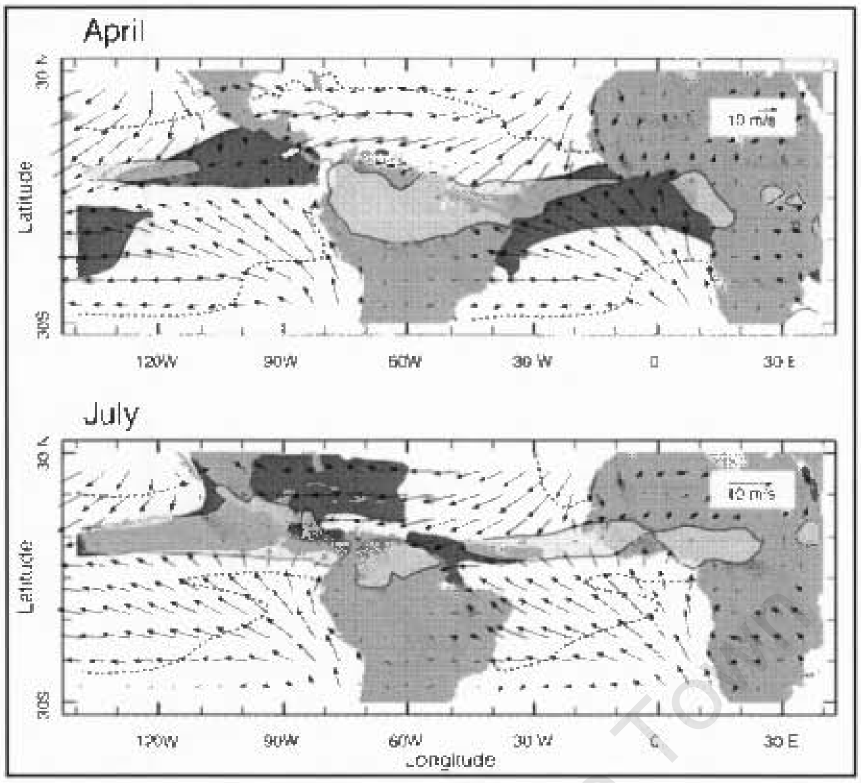

Figure 2.3: April and July climatologies of the tropical Atlantic and eastern Pacific. Dark shaded areas have SST = 28°C. Light, semi-transparent areas are regions with rainfall = 6mm/day (the ITCZ). The arrows depict the surface (10m) wind vectors with scale indicated in the Figure. Doted contour is the 24°C isotherm demarking the regions of relatively cold water and the eastern cold tongues (from Schott *et al.*, 2004, *CLIVAR panel white paper*).

2.3 Equatorial Currents

The Tropical Atlantic plays an important role on the inter-hemispheric water masses exchange and consequently on the net heat transport, which in this case, is a northward net heat transport (Stramma *et al.*, 2003). The heat budget in the Tropical Atlantic is controlled by a complex network of processes such as advection, equatorial and coastal upwelling/downwelling and equatorial wave guide (Schott *et al.*, 2004, *CLIVAR panel white paper*).

The heat budget in the Tropical Atlantic is important because of its impact on the SST field variability, which is directly linked to convection and trade winds strength and ultimately controls the climate variability of the region (Carton *et al.*, 1996; Carton and Zhou, 1997). For example, the variability in rainfall regimes over north-east Brazil and West Africa strongly depends on the SST fields over the western and eastern Tropical Atlantic respectively.

The inter-hemispheric water exchange (meridional exchange) can be summarized as a transport from the South Atlantic to North Atlantic of warm waters on the surface and cold dense water on the bottom. In the central layer (North Atlantic Deep Water) the south-north transport in the upper and bottom layer is compensated with a north-south transport of cold dense water. This inter-hemispheric water masses exchange is part of the well known Thermohaline Circulation (e.g., Gordon, 1986, cited in Peterson and Stramma (1991); Rahmstorf, 2006).

The Atlantic equatorial upper-ocean circulation mainly consists of bands of eastward and westward zonal currents along the equator, and poleward/coastal currents along the western and eastern boundaries of the Atlantic Ocean (Stramma *et al.*, 2003). As mentioned in the previous section, these zonal flows are strongly dependent on the variability of trade winds. Both zonal flows have impacts on the western and eastern Tropical Atlantic. For example, the equatorial and northern-most branches of the South Equatorial Current (SEC) feed the North Brazilian Current (NBC), which through eddy formation in the NBC retroflection area accounts for a large amount of inter-hemispheric heat exchange (e.g., Stramma *et al.*, 2003). Another relevant aspect of these zonal flows is that they constitute the north and south boundaries of the South and North Sub-tropical Gyres, respectively (e.g., Stramma and Schott, 1999).

Figure 2.4 illustrates the Tropical Atlantic upper-ocean circulation. The characteristics and variability of the currents will be discussed in this section.

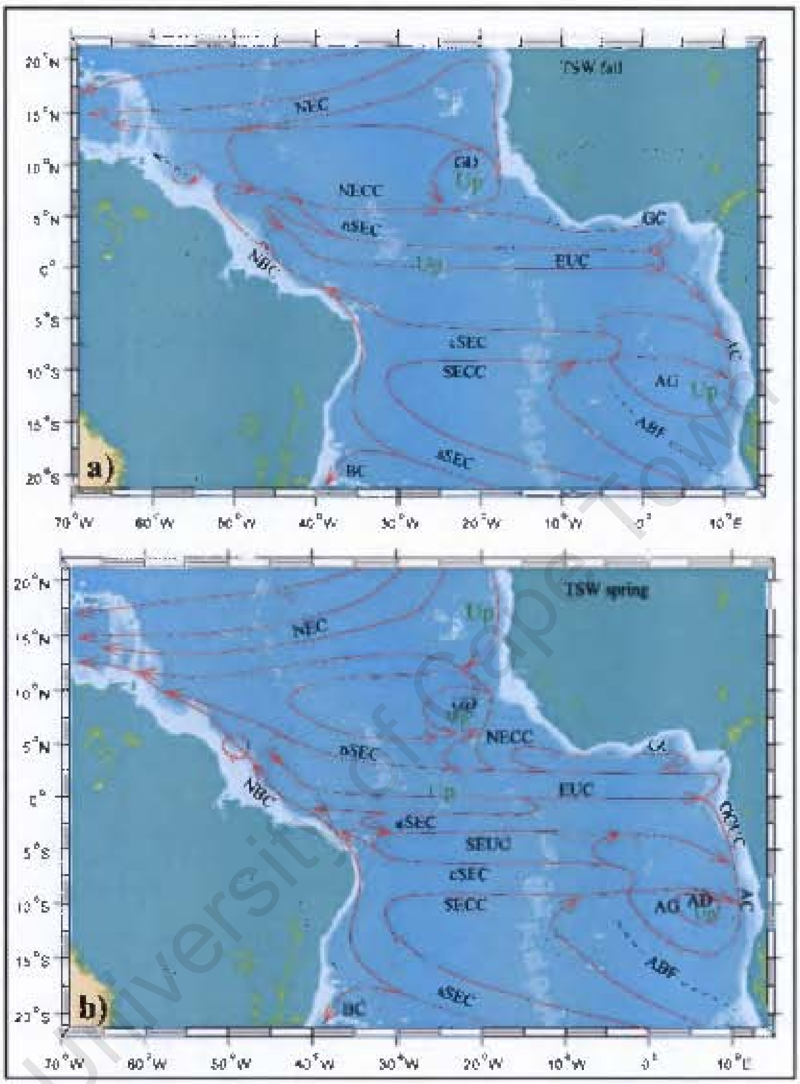

Figure 2.4: Schematic maps showing the horizontal distribution of the major tropical currents for the Tropical Surface Water layer at about 0-100m depth: a) austral fall and b) austral spring. Shown are: North Equatorial Current (NEC), the Guinea Dome (GD), the North Equatorial Countercurrent (NECC), the Guinea Current (GC), the South Equatorial Current (SEC) with the northern (nSEC), equatorial (eSEC), central (cSEC) and southern branches (sSEC), the Equatorial Undercurrent (EUC), the North Brazil Current (NBC), the Gabon-Congo Undercurrent (GCUC), the Angola Gyre (AG), the Angola Current (AC), the Angola Dome (AD), the South Equatorial Undercurrent (SEUC), the South Equatorial Countercurrent (SECC) and the Brazil Current (BC). The Angola-Benguela Front (ABF) is included as a dashed line. "Up" marks possible areas of upwelling, but not exact places (from Stramma *et al.*, 2003; modified after Stramma and Schott, 1999 and Stramma and England, 1999).

South Equatorial Current (SEC)

According to Molinari (1982) (cited in Stramma and Schott, 1999) the South Equatorial Current can be divided into four branches: southern (sSEC), central (cSEC), equator (eSEC) and northern (nSEC) branch (see **Figure 2.4**).

The sSEC, which is an extension of the Benguela Current (BC), flows north-westward across the South Atlantic until it reaches the Brazil shelf. It has been suggested that this broad sluggish flow of water between 10°S and 25°S east of 30°W (Peterson and Stramma, 1991; Stramma *et al.,* 2003) was the northern part of the South Atlantic Sub-Tropical gyre (Stramma and Schott, 1999). Recently it was suggested that the sSEC carries important climatic signals from the subtropics to the tropics (Lazar *et al.*, 2001, cited in Stramma *et al.*, 2003). West of 30°W and between 20°S and 15°S the sSEC has different fates. One portion feeds the poleward Brazil Current (BC) and another feeds the North Brazil Undercurrent (NBUC). Finally, a smaller portion re-circulates and feeds the eastward South Equatorial Counter Current (SECC) (Stramma *et al.*, 2003). Early estimations of the sSEC transport showed that this current carries 16Sv across 30°W and that as it diverts into the NBUC and BC; 12Sv feeds the NBUC and 4Sv feeds the BC (Stramma *et al.*, 1990; cited in Peterson and Stramma, 1991). Schott *et al.* (1998) (cited in Stramma and Schott, 1999) did not find strong seasonal cycle in the sSEC and recently Stramma *et al.* (2003) confirmed these results.

The cSEC can be found between the South Equatorial Counter Current (SECC) and the South Equatorial Undercurrent (SEUC) and is fed by the re-circulation of the

SECC. The cSEC flows westward until it reaches the Brazil shelf (west of 30°W), where merges with the NBUC to form the surface-intensified North Brazil Current (NBC). The cSEC feeds the NBC with 7Sv (Schott *et al.*, 2003).

The eSEC and nSEC are directly fed by the Equatorial Undercurrent (EUC) and can be regarded as a compensation flow of the latter. However there are no estimations quantifying the EUC contribution in the eSEC and nSEC (Stramma and Schott, 1999). The nSEC was estimated as carrying +- 11Sv; 3.4Sv in the surface layer and 7.7Sv in a second core just underneath the surface layer (Schott *et al.*, 2003).

North Brazil Current (NBC)

The NBC is one of the most important western boundary currents and results from the merging of the NBUC and the cSEC. It is a surface-intensified north-westward current and is responsible for most of the meridional heat transport across the equator (Stramma and England, 1999). Its seasonal cycle is linked to the ITCZ seasonal meridional migration. During the austral summer (**Figure 2.4a**), when the ITCZ reaches its northern-most position, the NBC retroflects eastward, feeding the North Equatorial Countercurrent (NECC) (Stramma and Schott, 1999). In the retroflection area, between 6°N-10°N, several observations found the formation of anti-cyclonic eddies which are regarded as an important means for inter-hemispheric heat transport to the North Atlantic (Stramma and Schott, 1999). Schott *et al.* (2003) estimated an associated transport of 32.4Sv south of 4°S and 39.2Sv north of 4°S.

North Equatorial Counter Current (NECC)

As mentioned above, the NECC is one of the currents that show stronger seasonal variations in the equatorial region. Following the ITCZ seasonal cycle, the NECC is present and well developed as an eastward flow across the entire Atlantic Basin during the austral winter (**Figure 2.4a**) when it also shows maximum velocities (Stramma and Schott, 1999). During the austral fall, the presence of the NECC is restricted to the eastern side of the Atlantic basin, in contrast to the absence or reverse flow on the western side of the basin (**Figure 2.4b**). The origin of the NECC is a result of the convergence of the NBC retroflection and NEC, the former with a transport of 16Sv and the latter of 8Sv (Wilson *et al.*, 1994; cited in Stramma and Schott, 1999). As the NECC meets the African continent promontory and shelf, it accelerates, forming the Guinea Current.

Equatorial Undercurrent (EUC)

The Equatorial Undercurrent is the strongest eastward flow along the equator and crosses the entire Atlantic Basin. Peterson and Stramma (1991) described the EUC as a narrow jet having a half-width of about 1.5° latitude, a velocity maxima of 100cms^{-1}, centred at 100m depth and a transport decrease due to frictional loss as it moves eastward.

The driving mechanism is a direct response to the zonal wind field over the western Atlantic basin surface layer. The accumulation of water on the western boundary due to frictional action of the easterlies over this area creates a subsurface eastward pressure gradient (Arthur, 1960; cited in Peterson and Stramma, 1991).

The EUC is a saline, oxygenated current and is mainly formed by South Atlantic water masses, which is consistent with the fact that the main source of the EUC is the NBC (Tsuchiya, 1986; Philander and Pacanowski, 1986; cited in Peterson and Stramma, 1991).

Earlier observations of the EUC showed that the current was stronger on the western Atlantic side, losing its strength as it moved eastward (Düing *et al.*, 1975; cited in Peterson and Stramma, 1991). More recently Brandt *et al.* (2006) reported mean transport values of 20Sv (5.4Sv surface layer + 14.6Sv thermocline layer) at 35°W and 13.8Sv (3.1Sv surface layer + 10.7Sv thermocline layer) at 26°W. This shows that in 11° of longitude the EUC looses a quarter of its strength.

The seasonal cycle of the EUC was described as a deepening and shallowing of the core current, rather than transport/velocity variations (Weisberg and Colin, 1986; Philander and Pacanowski, 1986; Peterson and Stramma, 1991). However, Stramma and Schott (1996) (cited in Stramma and Schott, 1999) reported lower transport values during austral autumn.

The seasonal cycle is also reflected in the Atlantic eastern basin, near the African coast, where the EUC terminates and bifurcates northward and southward, feeding the nSEC to the north and the eSEC to the south (Stramma and Peterson, 1999). The position along the equator where the bifurcation takes place was suggested to depend on the EUC core depth. During the austral winter, when the EUC core is deeper, the EUC terminates near the African coast, forming a well-defined Gabon-Congo Undercurrent (GCUC), whereas in the austral summer, the EUC bifurcates before 1°E, flowing south-eastward between 2°S and 8°S, and eventually merging with GCUC (Wacongne and Piton, 1992; cited in Stramma and Schott, 1999). However, based on ADCP observations Mercier *et al.* (2003) suggested that the EUC might have small contribution to the GCUC.

Guinea Current (GC)

The GC is an extension of the NECC and results from the acceleration of the latter as it approaches the African Continental shelf. The GC can be found around 2°-4°N/10°W extending until 9°E, and is well pronounced in depths greater than 1000m (Artamonov *et al.*, 2002; Lumpkin and Garzoli, 2005).

The geostrophic component of the GC shows a seasonal cycle, i.e. from December to March it shows an eastward flow and during the austral winter and spring it reverses as a westward flow. In addition, the seasonal cycle of the GC is directly linked to the zonal wind semi-annual cycle over the eastern Atlantic basin (Philander and Pacanowski, 1986; Artamonov *et al.*, 2002).

Artamonov e*t al.* (2002) estimated a geostrophic eastward current of approximately 12cms^{-1} and a westward current of 20cms^{-1}. More recently, Garzoli and Lumpkin (2005) estimated an average geostrophic current of about 57cms^{-1} between 3-6°N and a total (Ekman component included) eastward current of approximately 65cms^{-1}.

As it flows eastward, west of 5°W, the GC diverts southward, feeding the nSEC and closing the tropical gyre on the eastern Atlantic basin. It also continues flowing until it reaches the African coast, where it turns south and merges with the Angola Current (AC) (Lumpkin and Garzoli, 2005).

South Equatorial Countercurrent (SECC)

The SECC is a geostrophic eastward current centred at 10°S. It can be found between the surface and ~275m with subsurface geostrophic maximum velocity of 10cms^{-1} (Peterson and Stramma, 1991). Wacongne and Piton (1992) suggested that the main mechanism maintaining the SECC is the wind stress curl.

Moroshkin *et al.* (1970) observed that in the region of 8-9°E/10°S the SECC turned southward, feeding the Angola Current. More recently Mercier *et al.* (2003) confirmed the early findings of Moroshkin *et al.* (1970), i.e., reporting a well developed eastward geostrophic current between the surface and 300m depth with an estimated transport of 4.2Sv. In addition, Mercier *et al.* (2003) observed re-circulations of the SECC feeding the westward cSEC and sSEC as well as its contribution to the northern limb of the Angola gyre system between 100m and 200m.

South Equatorial Undercurrent (SEUC)

The SEUC can be found between 3-8°S and 200m-500m depth range. It flows below the SEC and its low-oxygen waters, west of 35°W, are likely to have originated from the SEC re-circulation pattern (Schott et al, 1995; cited in Stramma and Schott, 1999).

However, east of 35°W the SEUC also carries a high-oxygen layer originating from sSEC (Tsuchiya, 1986; cited in Stramma and Schott, 1999). Tsuchiya (1986) (cited in Mercier *et al.*, 2003) also suggested that the SEUC is part of the equatorial thermostad.

The SEUC transport increases as it flows eastward. Schott *et al.* (2003) gave an estimated transport of 2.8Sv at 35°W, while Mercier *et al.* (2003) estimated the transport to be 7.5Sv at 9°W. However, the SEUC geostrophic transport shows high variability (Molinari, 1982; cited in Mercier *et al.*, 2003) and other authors reported larger values for the SEUC transport, especially east of 25°W (Stramma and Schott, 1999).

The SEUC meridional position also varies. As it moves eastward the SEUC bends southward, and as it reaches the Atlantic eastern basin and the EUC at 8°S it forms the northern limb of the Angola Gyre (Peterson and Stramma, 1999). This has been directly linked to the formation of the Angola Dome (Voituriez, 1981; cited in Peterson and Stramma, 1999).

During the austral winter the SEUC is weaker in the eastern basin while stronger in the western basin (Reverdin *et al.*, 1991, cited in Stramma and Schott, 1999) and since minimum values of wind stress curl can be observed over the same period and area, Wacongne and Piton (1992) suggested that the seasonal cycle of the SEUC must be driven by the wind stress curl.

2.4 Angola System

Angola Gyre (AG)

Earlier observations over the eastern Atlantic basin showed a closed cyclonic geostrophic gyre centred at 13°S-4°E, less than 1000km across and extending from the surface to 300m depth (Moroshkin *et al.*, 1970). Moroshkin *et al.* (1970) suggested that its southern and western limb were the Benguela Current and its north-westward flow respectively. They attributed the northern boundary to the SECC, which together with EUC and SEUC would form the Angola Current (AC) and the eastern boundary of the gyre (see **Figure 2.4**).

Gordon and Bosley (1991) also found the presence of cyclonic circulation in observations conducted during 1983-1984. They found the gyre centred over 13S-5°E, which was in agreement with Moroshkin *et al.* (1970), but they reported that the gyre extended 2000km across. In addition, Gordon and Bosley found that the gyre had a southward shift at depth; at 500m the gyre was found near 18°S-5°E but was still 2000km wide. The southern boundary of the AG was suggested to be the Angola-Benguela Front (ABF) instead of the BC as suggested by Moroshkin *et al.* (1970). Within the gyre, Gordon and Bosley (1991) found high salinity and oxygen-depleted waters and suggested that this could be a consequence of high productivity as well as excess regional evaporation (Voituriez and Herbland, 1982; cited in Gordon and Bosley, 1991).

The driving mechanism of the AG was suggested to be associated with negative wind stress curl (Sverdrup dynamics). However, Gordon and Bosley (1991) and Wacongne and Piton (1992) stated that the effect of the wind (Ekman divergence) in the region masked the gyre on ship drift data. Gordon and Bosley (1991) also argued that the negative wind stress curl would not be enough to drive the gyre, suggesting that the eastward equatorial currents (EUC, SEUC and SECC) together with local negative wind stress curl would be the driving mechanisms. In fact, Wacongne and Piton (1992) and more recently Mercier *et al.* (2003), using observations from the north-eastern Atlantic, confirmed that the SEUC and SECC form the northern boundary of the AG, and that their southward bending contributes to the AC as well as the Gabon Congo Undercurrent (GCUC).

Angola Dome (AD)

Within the AG, the "Angola Dome" is a seasonal subsurface feature of the thermocline that can not be detected from SST field. It is centred near 10°S-9°E (Mazeika, 1967, cited in Peterson and Stramma, 1991). It is a cyclonic feature and can be observed during the austral summer as the thermocline uplifts from 150m depth to 20m (Mazeika, 1967, cited in Peterson and Stramma, 1991). However, Voituriez (1981) and Voituriez and Herbland (1982) (cited in Peterson and Stramma, 1991) showed evidence that it is a permanent sub-thermocline feature induced by the SEUC. It outcrops when negative wind stress curl creates upwelling in the region (see **Figure 2.5**).

Stramma and Schott (1999) suggested that the AD and AG would have independent driving mechanisms; the first driven by the local wind field (as mentioned above) and the second driven by the large-scale current system. **Figure 2.5** depicts the Guinea **(a)** and Angola **(b)** Domes temperature signature respectively during July/September and January/April.

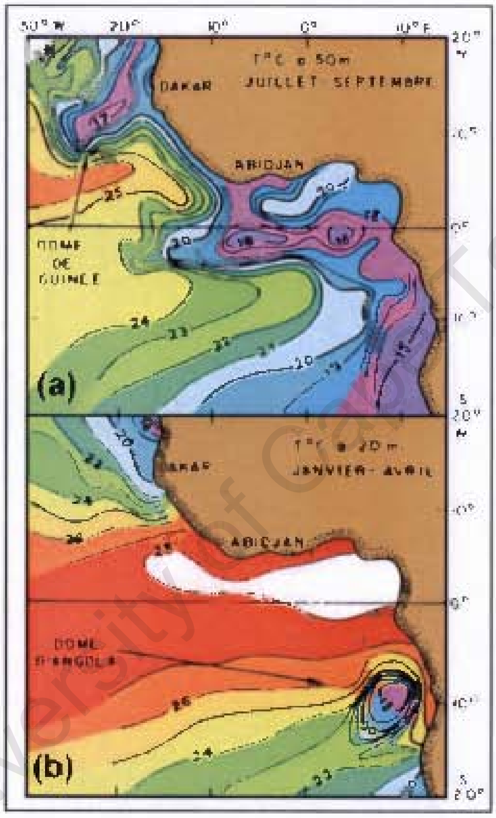

Figure 2.5: **Angola/Guinea Dome as observed from temperature fields between 20m and 50m depths (from Tomczak and Godfrey, 2001; adapted from Peterson and Stramma, 1991).**

Gabon-Congo Undercurrent (GCUC)

The GCUC was named after Wacongne and Piton's (1992) observations on the continental shelf and slope off Gabon and Congo. The mean currents revealed a seasonal and highly variable undercurrent driven by local upwelling as well as by the

EUC and partially by the SEUC (see **Figure 2.4**). Wacongne and Piton (1992) suggested that the GCUC would be stronger during the boreal summer, in phase with a stronger EUC which surges inertially along the equator, creating a deep poleward zonal pressure gradient forcing on the eastern boundary. This pressure gradient force would result in a well-defined saline south-eastward GCUC along the shelf break. When the EUC is weaker, Wacongne and Piton (1992) suggested that the gradient forcing would branch before 1°E, resulting in an eastward flow which would eventually merge with the GCUC around 4-6°S, or with the Angola Current further south.

Angola Current (AC)

As mentioned above, the AC is the eastern boundary of the AG (see **Figure 2.4**). From *in situ* data, Moroshkin *et al.* (1970) suggested that the AC would be fed by the SEUC and SECC re-circulations. Shannon *et al.* (1987) described the AC as a permanent poleward-flowing current in the upper 200m over the Angolan continental slope. They also found that the current is weaker during the late austral winter/early spring and stronger during the late summer/early autumn, disrupting the Angola Benguela Front (ABF).

More recently Mohrholz *et al.* (2001) and Mercier *et al.* (2003) suggested, from ADCP observations, that this current would be the result of the convergence of the EUC and SEUC. Mohrholz *et al.* (2001) measured a 40cms^{-1} current and the transport of the AC was estimated as being 16Sv (Mercier *et al.*, 2003).

Mercier *et al.* (2003) suggested two fates for the AC: one would form the Angola Benguela Frontal Zone as the AC meets the cold waters of the Benguela upwelling system and turns westwards (southern boundary of the AG), and the second would continue as a poleward undercurrent and flow onto the Namibian shelf.

2.5 Angola-Benguela Frontal Zone

Descriptions of the dynamics and behaviour of the Angola-Benguela Frontal Zone (ABFZ) appear in many studies (e.g., Hart and Currie, 1960; Shannon *et al.*, 1987; Shannon and Agenbag, 1987; Meeuwis and Lutjeharms, 1990; Kostianoy, 1994; Kostianoy and Lutjeharms, 1999; Mohrholz *at al.*, 2001; Pichevin *et al.*, 2005; Veitch *et al.*, 2006).The ABFZ was first recognized by Hart and Currie (1960) (cited in Peterson and Stramma, 1991).

Shannon and Nelson (1996) defined the ABFZ as the northern boundary of the Benguela upwelling system. According to Meeuwis and Lutjeharms (1990), the convergence of the warm poleward Angola current with the cold waters from the Benguela upwelling system is the main factor maintaining the ABFZ. However, the wind curl has also been regarded as a key factor for maintaining the frontal zone (Shannon and Nelson, 1996). Bathymetry, coastal orientation and stratification have been identified as playing an important role on the ABFZ dynamics (Shannon and Nelson, 1996).

From the studies mentioned above one can summarize the ABFZ as an area of permanent steep meridional temperature gradients (4°C per 1° of latitude) (Shannon *et al.*, 1996). During the austral summer the ABFZ shows a stronger temperature gradient (1° per 34km) than during the winter (1° per 40km) (Veitch *et al.*, 2006). Veitch *et al.* (2006) reported an average north-west orientation. However; the ABFZ can present other orientations (Meeuwis and Lutjeharms, 1990; Shannon *et al.*, 1996). The strong thermal and salinity signatures can be observed down to 50m but the front remains visible down to 200m depth (Shannon *et al.*, 1996). The zonal/meridional extensions as well as its seasonal fluctuations were investigated in detail by Veitch *et al.* (2006). They concluded that the ABFZ is well defined 250km offshore throughout the year but can extend further than 700km during the summer with weak thermal gradients. Its latitudinal extension varies between 16°S and 17°S during the austral winter and between 15.5°S and17°S in the summer. In addition, based on a paleoclimate study Pichevin *et al.* (2005) showed that the position of the ABFZ was further north (6-9°N) during the glacial period.

The impact of the Benguela Niños/Niñas on the ABFZ in terms of its position and thermal gradients was also investigated by Veitch *et al.* (20060 (see **Figure 2.6**). They observed that during years of Benguela Niños, and also during minor warm events, the ABFZ was displaced poleward and could be found as far south as 25°S, with steeper thermal gradients. Their study found no significant impact of cold events on the ABFZ latitude but with slightly weaker thermal gradients.

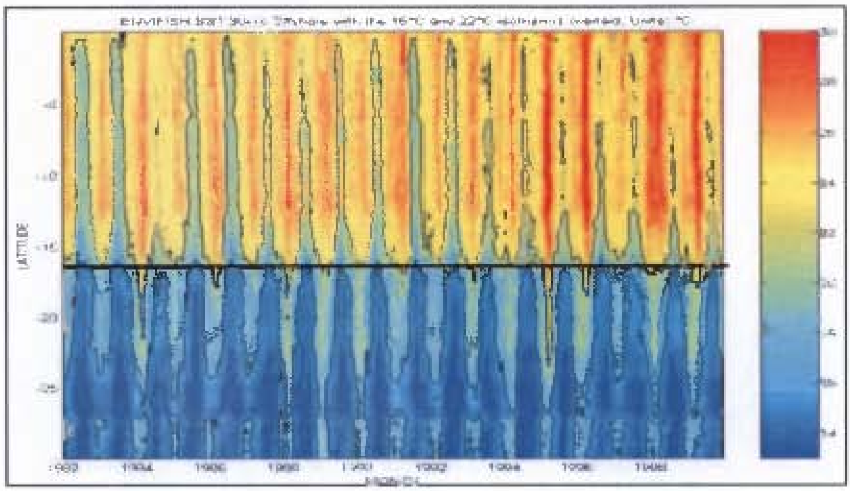

Figure 2.6: Hoffmöller plot of the SSTs of a meridional section 30km offshore extending from 0 to 30°S for the period from January 1982 to December 1999. Two isotherms – 16°C and 22°C – are overlaid (from Veitch *et al.*, 2006).

2.6 Benguela Niños/Niñas

The South Atlantic Ocean experiences abnormal events that resemble the Pacific El Niño/Niña and are characterized by SST anomalies (SSTA) along the equator and further south along the coast of Angola and Namibia (Shannon et al., 1986). For instance, SSTA observed during the 1984 Benguela Niño (see below) show geographical patterns that are quite similar to those observed during ENSO events in the Equatorial Pacific.

The similarities between warm events in the Atlantic and Pacific oceans were first directly observed during the SEQUAL/FOCAL programme (Katz *et al.*, 1989). The aim of this programme was to understand the annual cycle of the Equatorial Atlantic. However; during 1984 the oceanic and atmospheric conditions were clearly abnormal and appeared to be comparable to El Niño conditions in the Pacific (Philander, 1986), with southward shift of the ICTZ, weaker equatorial trade winds and development of an eastward current advecting saline warm waters in the Atlantic eastern basin.

Weisberg and Colin (1986) described the zonal behaviour of the thermocline along the equator during 1983-84, using *in situ* data as well as SST and zonal velocity anomalies. In 1984 they observed thermocline response to the relaxation of the easterlies: the shoaling in the western Atlantic basin and deepening of the eastern basin. They also noted the disappearance of the equatorial SST horizontal gradient between the western and eastern basin.

Hisard *et al.* (1986) also reported anomalous upper ocean temperature along meridional sections from 5°S to 15°N at different longitudes at the equator. Their observations, conducted during 1983 and 1984, showed that during 1984 the thermocline was systematically deeper than in 1983, especially in the eastern Atlantic basin. Another striking anomalous feature was the appearance of an eastward surface current between the equator and 5°S, which resulted in an accumulation of warmer water in the eastern Atlantic. This accumulation of warm water was suggested to be responsible for the 1984 Benguela Niño as it was advected poleward along the African coast, disrupting the Benguela upwelling system (Hisard *et al.*, 1986, Shannon *et al.*, 1986).

During the SEQUAL/FOCAL programme, Katz *et al.* (1986) investigated the sea slope along the equator. Using various methods they reported an unusual sea surface sloping upwards to the east during January-March 1984, reaching a maximum of 20dcm (dynamic cm) in the eastern Atlantic Basin.

The changes in the entire Equatorial Atlantic during 1984 were linked to unusual atmospheric conditions. Horel *et al.* (1986) reported that during 1984 the trade winds were weaker, there was an enhanced equatorial convection, and the ITCZ was displaced further south than its usual position between the equator and 15°N. This resulted in enhanced rainfalls over north-east Brazil and south-west Africa, in contrast to a persistent Sahel drought.

After the SEQUAL/FOCAL programme, several warm events were identified by different authors: 1934, 1949, 1963 and 1984 (Shannon *et al.*, 1986), 1995 (Gammelsrød *et al.*, 1998), and 1986 and 2001 (Rouault *et al.*, 2003; Florenchie *et al.* 2004; Rouault *et al.*, 2007). Cold events were also reported in 1982, 1983, 1986/1987, 1991/1992 and 1997 by Florenchie *et al.* (2004). **Figure 2.7** shows the time series from 1982-2007 of OI-SST anomalies averaged over the Angola/Benguela frontal zone, whereas **Figure 2.8** displays the SST anomaly composites of major cold and warm events during the last century.

Gammelsrød *et al.* (1998) provided the first *in situ* observations of an extreme warm event, the 1995 Benguela Niño. During a cruise along the coasts of Angola and Namibia they noticed an enhanced poleward current as well as an unusually high amount of warm saline water in entire area. **Figure 2.9** shows the strong subsurface positive temperature and salinity anomalies measured in March 1995 over the Namibian shelf.

Like their Pacific counterparts, warm/cold extreme events in the eastern tropical Atlantic are generated by remote zonal wind anomalies along the equator. However, some warm/cold events could be locally forced. A weakening of southerly winds or an unusual strengthening of the Angola Current (AC), leading to an intrusion of warm waters into the Benguela upwelling system, can not be ruled out. It is important to note that the eastern Atlantic has a seasonal warming that occurs after July-August when the trade winds start decreasing again over the equatorial eastern Atlantic. It results in the enhancement of the AC and consequently advection of warm and saline waters of equatorial origin.

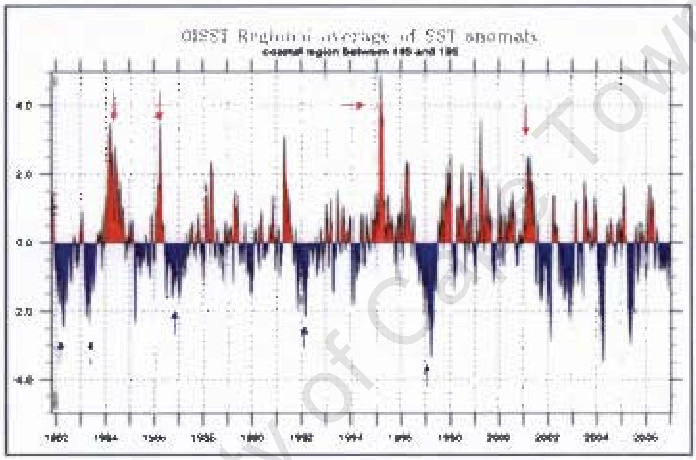

Figure 2.7: Averaged OI-SSTA over the ABFZ, between 14°S-19°S, from 1982 to 2007. Red arrows highlight warm year events and blue arrows highlights cold year events (from BCLME State of the Ecosystem Information System (SEIS) website).

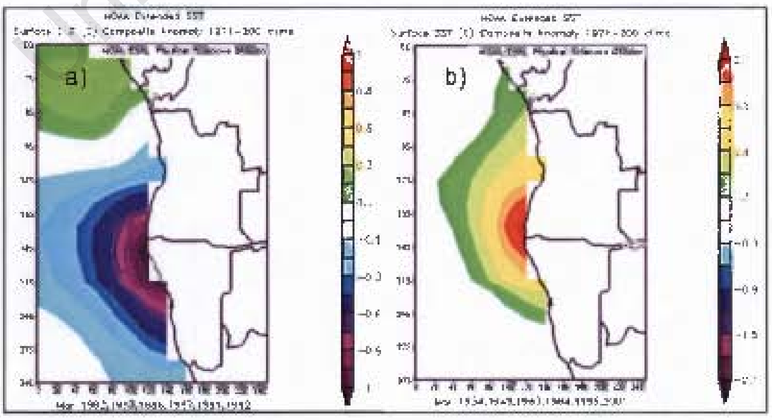

Figure 2.8: Composites of NOAA Extended SST anomalies in March for a) 1982, 1983, 1986/1987, 1991/1992 and 1997 cold events and b) 1934, 1949, 1963, 1984, 1986, 1995 and 2001 warm events *(http://www.cdc.noaa.gov).*

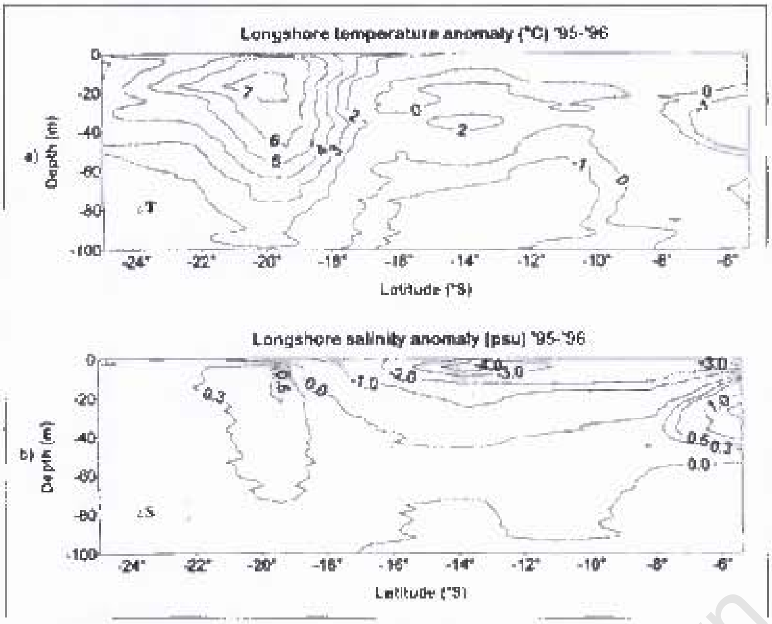

Figure 2.9: Vertical distribution of anomalies of (a) temperature and (b) salinity between March 1995 and March 1996 in a section parallel to the coast near the 100m isobath. Note the strong positive temperature anomalies from 14°S-20°S (from Gammelsrød *et al.*, 1998).

In recent studies Florenchie *et al.* (2003, 2004) confirmed that, prior to Benguela Niños or Niñas (warm/cold events), wind negative/positive anomalies are observed off the Brazilian coast in the beginning of the austral summer (see also Carton and Huang, 1994). These anomalies trigger trapped equator downwelling or upwelling Kelvin waves that propagate along the equatorial thermocline. **Figure 2.10** shows the correlation between zonal wind anomalies off the Brazil coast and SST anomalies averaged over the Angola-Benguela Frontal Zone (ABFZ) while **Figure 2.11** shows the zonal wind anomalies averaged from 40°W to 15°W and from 2°N to 2°S, from 1999 to present. As the Kelvin wave reaches the African coast it turns into a trapped coastal wave, propagating poleward along the African coast until it outcrops in the ABFZ (Meeuwis and Lutjeharms, 1990). The behaviour of the anomaly propagation, particularly the temperature anomalies only manifesting at the surface as they reach the ABFZ, is explained by the equatorial Atlantic thermocline depth. While the equatorial thermocline depth in the Eastern Basin is to deep to allow the temperature anomalies to reach the surface, along the southern Angolan coast the thermocline depth is shallow enough to allow the sub-surface temperature anomalies to out-crop. **Figure 2.12** shows the propagation of the warm anomaly along the equator as well as its signature along the African coast, as simulated by the OPA model.

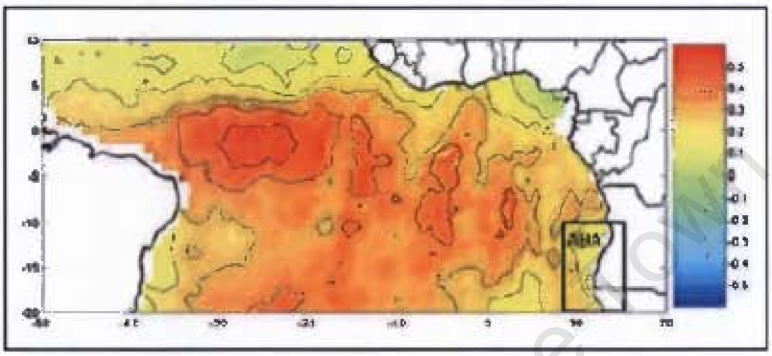

Figure 2.10: Maximized correlation between OI-SST anomalies averaged over the Angola Benguela Area (ABA) and ERS zonal winds anomalies over the South Atlantic for the period 1992 to 2000 (from Florenchie *et al.*, 2003).

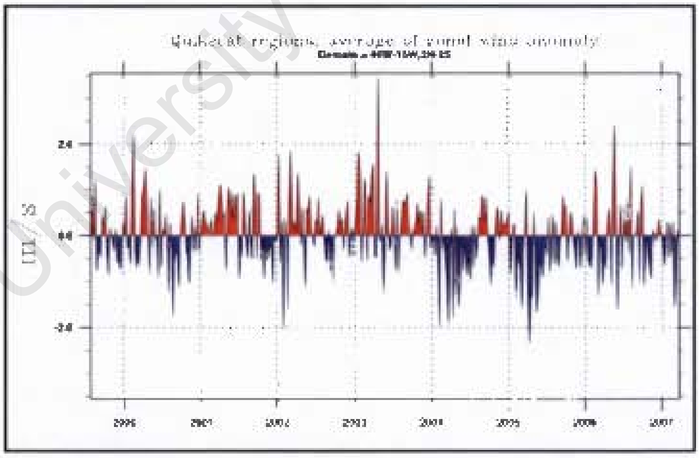

Figure 2.11: Quikscat zonal wind anomaly averaged along the equator over the area 40W-15°W and 2N-2°S, from 1999 to 2007 (from BCLME State of the Ecosystem Information System (SEIS) website).

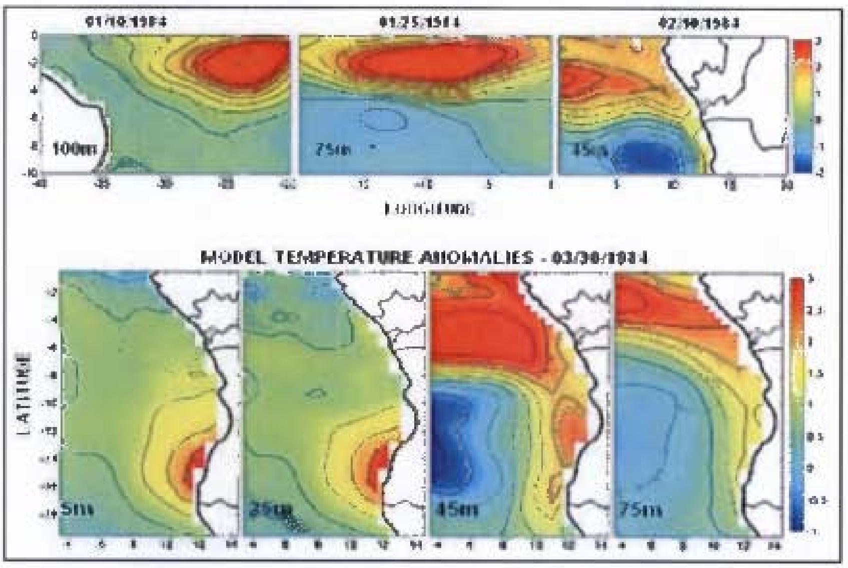

Figure 2.12: Upper panel illustrates the propagation of warm anomalies in January/February 1984 along the equator at 100, 75 and 45m depths. Bottom panel shows the warm anomaly signature along the African coast at 5, 25, 45 and 75m on 03/30/1984 (from Florenchie *et al.*, 2003).

The implications of the surface warming and its impacts on the sub-thermocline poleward flow over the Namibian shelf were addressed in a recent study by Monteiro *et al.* (2006b, submitted). They suggested that the surface warming caused by a warm event (either seasonal warming or a Benguela Niño) disrupts the barotropic equilibrium established under upwelling conditions, and the new baroclinic conditions enhance the poleward sub-thermocline flow over the Namibian shelf. Strong and persistent surface warming results in a stronger poleward flow therefore warm saline waters of equatorial and tropical origins will reach the Luderitz upwelling system and be upwelled, disrupting the cold, nutrient-rich system (Monteiro *et al.*, 2006b; submitted). **Figure 2.13** shows a diagram summarizing the mechanism of surface warming vs. sub-thermocline flow suggested by Monteiro *et al.* (2006b, submitted).

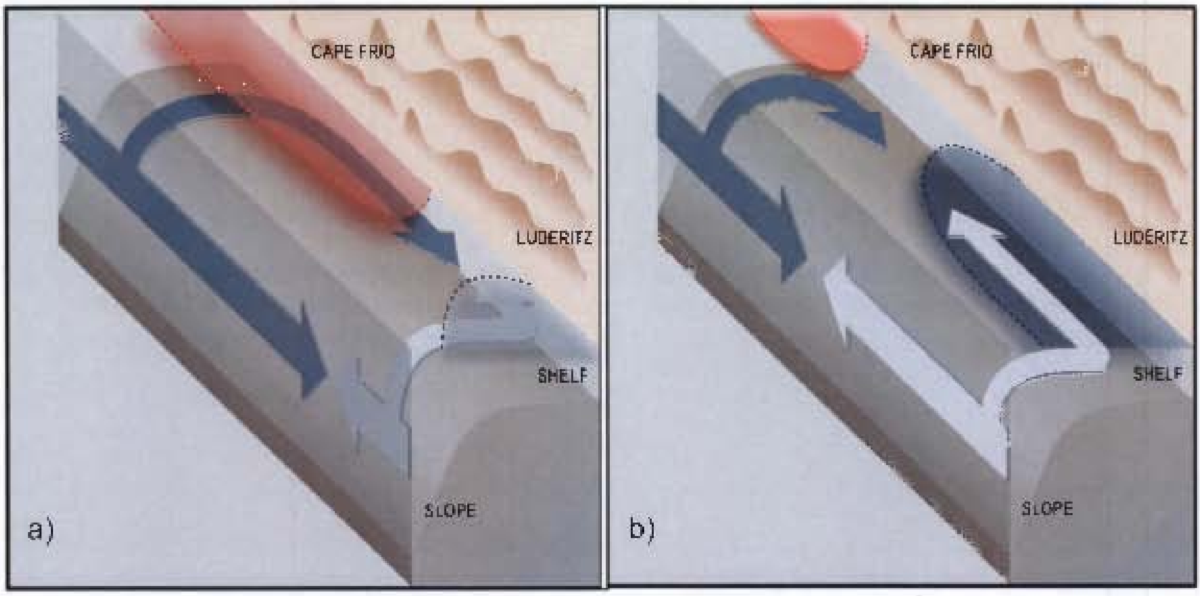

Figure 2.13: Mechanism of surface warming vs. sub-thermocline poleward flow over the Namibian shelf. Left panel (a) shows the sub-thermocline flow response to a strong surface warming, both sub-thermocline poleward flows (over shelf and offshore) extend far south reaching the Luderitz upwelling system (Benguela Niño "death" scenario). Right panel (b) shows the opposite scenario, i.e. warm surface waters found north of Cape Frio, thus sub-thermocline poleward flows stop at Cape Frio region (Benguela Niña re-animation scenario) (courtesy of Dr. Pedro Monteiro).

Extreme events like the 1995 Benguela Niño have a drastic impact on the local fisheries and climate, and consequently have a great social impact as well. During warm events dramatic collapse and change in fisheries stocks have been reported (Boyer *et al.*, 2001; Boyer and Hampton, 2001), whereas floods and heavy rainfall have occurred over land in Angola and Namibia (Rouault *et al.*, 2003). **Figure 2.14** shows the relationship between SST anomalies, moisture flux and rainfall during Benguela Niño years. However, the impact on rainfall is not linear and depends on other regional factors like the South Indian Ocean dipole (Reason et al., 2001).

Although extreme warm or cold events are clearly triggered remotely by an abnormal relaxation or strengthening of the zonal winds off the Brazilian coast, a clear distinction between moderate warm or cold events in the ABA and Benguela Niños or Niñas is still to be defined, raising discussion among the scientific community.

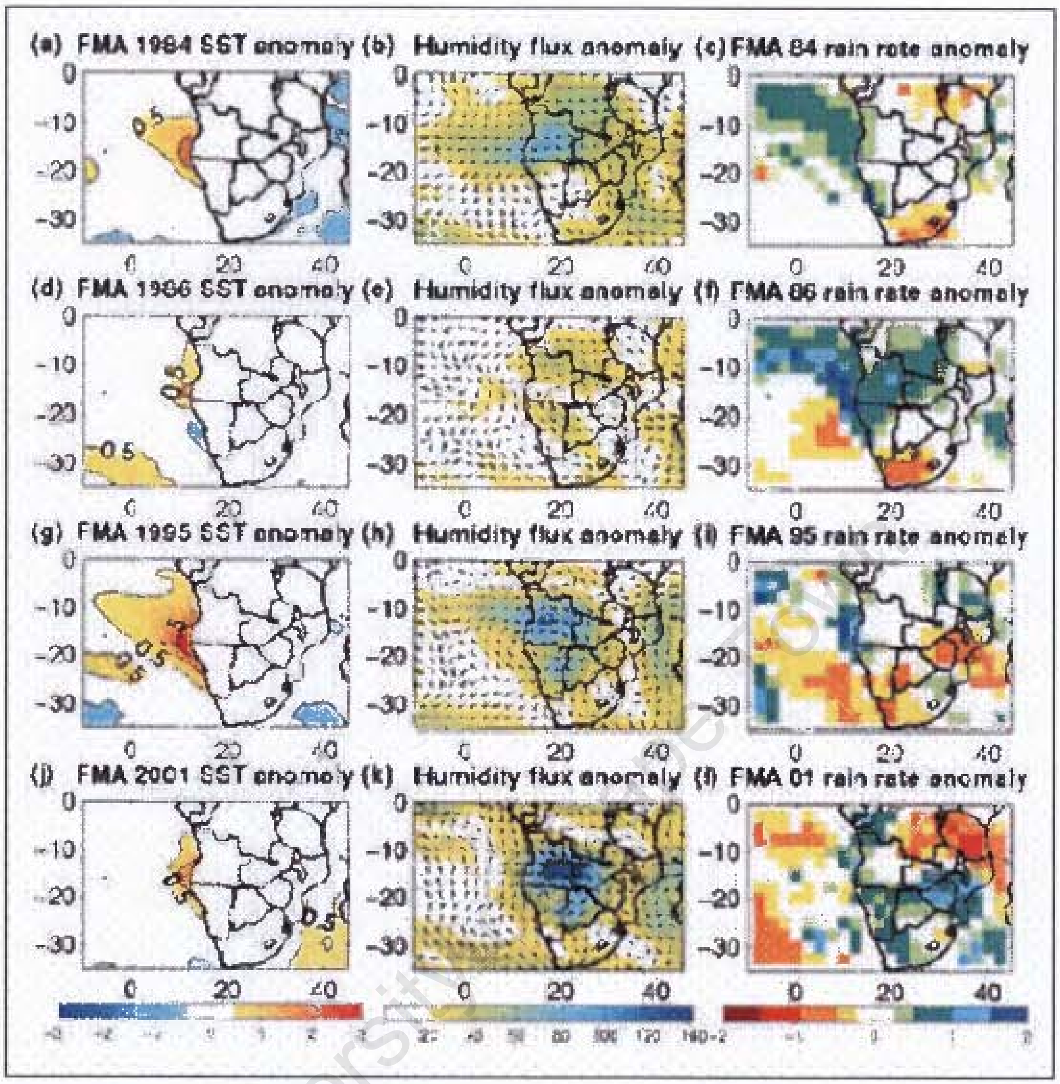

Figure 2.17: Left: mean FMA SST anomalies for 1984 (a); 1986 (d) 1995 (g) and 2001 (j) contour at 0.5°C, 1.5°C and 2.5°C. Middle: mean FMA integrated moisture form the surface to 300 hPa flux anomalies for 1984 (b), 1986 (e) 1995 (h) and 2001 (k) in g/kg.m/s. Right: mean FMA rain rate normalized anomalies for 1984 (b), 1986 (f) 1995 (i) and 2001 (i) (from Rouault *et al.*, 2003).

3 Data and Methods

In order to answer the questions raised in **Chapter 1**, the numerical model "Regional Oceanic Modeling System" (ROMS) was used to carry out this investigation. **Section 3.1** is dedicated to the main characteristics of the ROMS model. **Section 3.2** describes the setup and configuration of the first control simulations of the Equatorial Atlantic, as well as the different sensitivity tests performed. **Section 3.3** provides information on the various datasets used to validate the results obtained with ROMS, while in **Section 3.4** describes the statistical methods employed.

3.1 Regional Oceanic Modeling System (ROMS)

The **R**egional **O**ceanic **M**odeling **S**ystem (**ROMS**) has been developed at the University of California, Los Angels (**UCLA**) and Rutgers University. It allows resolving large-scale features as well as meso-scale and coastal features through its high-order numerics and high resolution nesting capacities. ROMS has been widely used in different physical applications and regional backgrounds (e.g. Colberg, 2006; Penven *et al.*, 2006; Speich *et al.*, 2006; Marchesiello *et al.*, 2003; Blanke *et al.*, 2002; Penven *et al.*, 2000).

ROMS is a split-explicit free-surface oceanic model with sigma vertical coordinates that solves the primitive equations of fluid dynamics by applying the hydrostatic and Boussinesq approximation for the vertical momentum balance (Shchepetkin and McWilliams, 2005).

The split-explicit technique provides a separation of the barotropic and baroclinic fields, i.e., allows the barotropic mode to be resolved by short time steps and the baroclinic mode, temperature and salinity by larger time steps (Shchepetkin and McWilliams, 2005). The baroclinic mode is discretized applying a third-order accurate predictor (Leap-Frog) and corrected using time-step algorithm (Adams-Molton). In the barotropic mode, in order to satisfy the 3D continuity equation, a special two-way time-average is applied (Shchepetkin and Mc Williams, 2005).

The horizontal advection scheme is a third-order and upstream-biased scheme, which allows the generation of steep pressure gradients. The vertical mixing scheme applied is the K-profile planetary (KPP) parameterization boundary-layer scheme (Large *et al.*, 1994).

The open boundaries are active (flow-adaptive), implicit, upstream-biased with outward radiation conditions (Marchesiello *at al.*, 2001). The vertical coordinates are terrain-following (sigma-coordinates), while the horizontal coordinates are orthogonal or curvilinear.

3.2 Model Setup

The four simulations carried out are based on the same ocean configuration except for the wind fields (see below for more information). Domain, topography, vertical and horizontal resolution, heat and salt fluxes, initialization, open boundaries conditions plus various other parameters are identical between the four simulations.

The domain extends from 15°S-10°N in latitude and 58°E-16°W in longitude (see **Figure 3.1**). It covers the entire equatorial Atlantic in order to follow the eastward propagation of thermocline warm/cold anomalies along the equator, and the subsequent poleward coastal propagation into the BCLME area.

The simulations use a 0.5 degree horizontal regular resolution, which means that the model grid has 149x52 points (longitude-latitude). The vertical resolution has 30 sigma-coordinate levels, with more levels near the surface where more resolution is required compared to deeper layers. The topography used was ETOPO-2, which has a 1/12° resolution and is widely used in the modelling community.

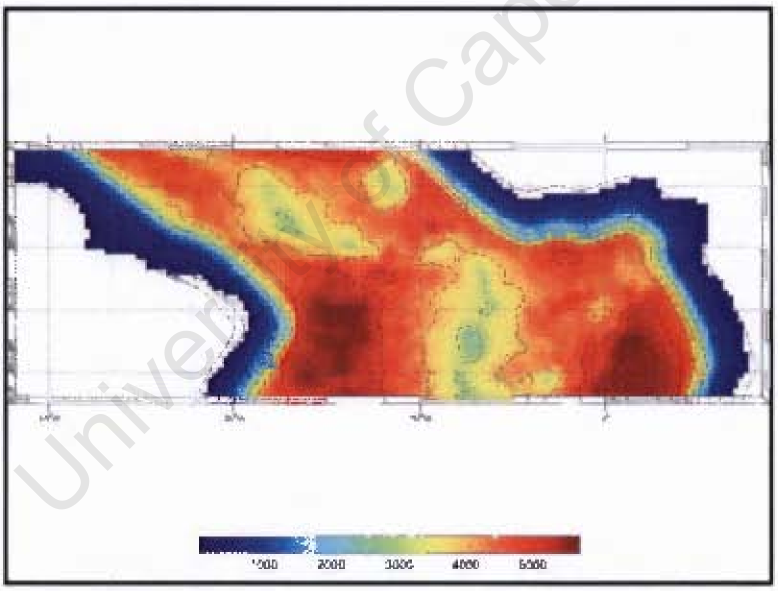

Figure 3.1: Simulations domain and topography superimposed (colourbar).

COADS (Comprehensive Ocean-Atmosphere Data Set) data have been used to force the model. COADS includes the climatologies of heat flux, fresh water flux, surface atmospheric density, surface atmospheric temperature, wind speed at 10m, sea level specific humidity, sea surface salinity and short wave radiation (heat and salt fluxes). Note that the sea surface temperature is computed by the model in each iteration, which in turn is used in the calculation of the restoring force of the heat flux (Penven *et al.*, 2001). Over the surface the salt flux is forced by a surface restoring term in salinity, implying that the salinity is relaxed towards COADS climatology (Penven *et al.*, 2001).

The model was initialized from rest (currents: $0ms^{-1}$) while geostrophic currents referred to 500m were applied at the boundaries. The initial and boundary conditions of both temperature and salinity are from the World Ocean Atlas 2001 (WOA01) climatology. The spatial coverage of the **ERS-1/ERS-2** wind fields is nearly global, extending from 80°N- 80°S in latitude, and from 180°W-180°E in longitude. The **ERS-1/ERS-2** mean wind fields are provided on a rectangular 1°x1° resolution grid. **ERS1** made measurements from 08/05/1991 to 06/02/1996, whereas **ERS2** was active from 03/25/1996 to 01/15/2001. **ERS2** measurements have been chosen during the overlapping period. Note also that the first seven months of **ERS1** were removed from the climatology calculation (i.e. data used span the period January 1992 to December 2000). *These data were obtained from CERSAT, at IFREMER, Plouzané (France).*

As mentioned above, four different simulations have been run using ROMS:

- Two control simulations: one using COADS wind climatology and the other using ERS wind climatology. In both cases a 10 year run was performed (see **Figure 3.4(a)**).

The purpose of these two simulations was to test ROMS ability to reproduce realistic temperature, salinity and current fields. The sensitivity simulations applying artificial wind anomalies were based on the ERS climatology:

- Two simulations using artificial wind anomalies were applied to the ERS wind climatology. In the first simulation, wind forcing has been reduced by 75% during January, February and March over an area off the Brazil coast (see **Figure 3.2** caption, **Figure 3.3** and **Figure 3.4(b)** for further details). In the second simulation, an artificial strengthening of 75% has been applied to the wind climatology during the same months and over the same area.

These sensitivity tests were carried out to analyse the model response to different wind anomalies in a region where wind anomalies are believed to trigger Benguela Niños/Niñas or warm/cold anomalies. The two sensitivity tests cover a one-year period using initial conditions provided by the climatological run, and their results are compared to the ones obtained from the ERS climatology control simulation (also see **Table 3.1**).

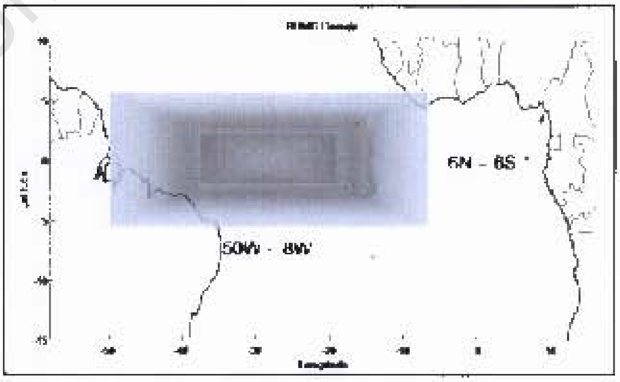

Figure 3.2: Simulation domain. Shaded area highlights the area where the artificial anomalies were applied on the ERS climatology field. The colour gradient, brighter on the edges to darker on the centre, represents the way the artificial anomalies were applied, allowing a smooth transition from the climatology values to the artificial values.

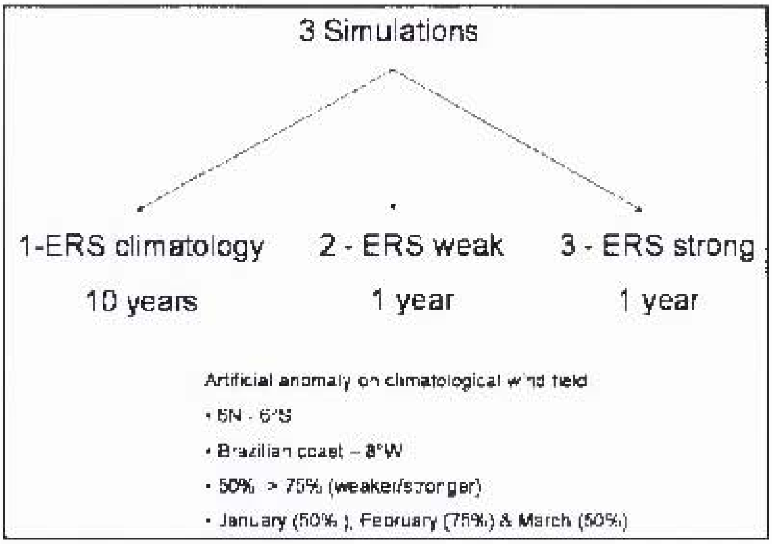

Figure 3.3: Diagram summarizing the three simulation settings evaluated using ERS climatology and artificial winds – years, artificial anomalies box, months and anomaly amplitude.

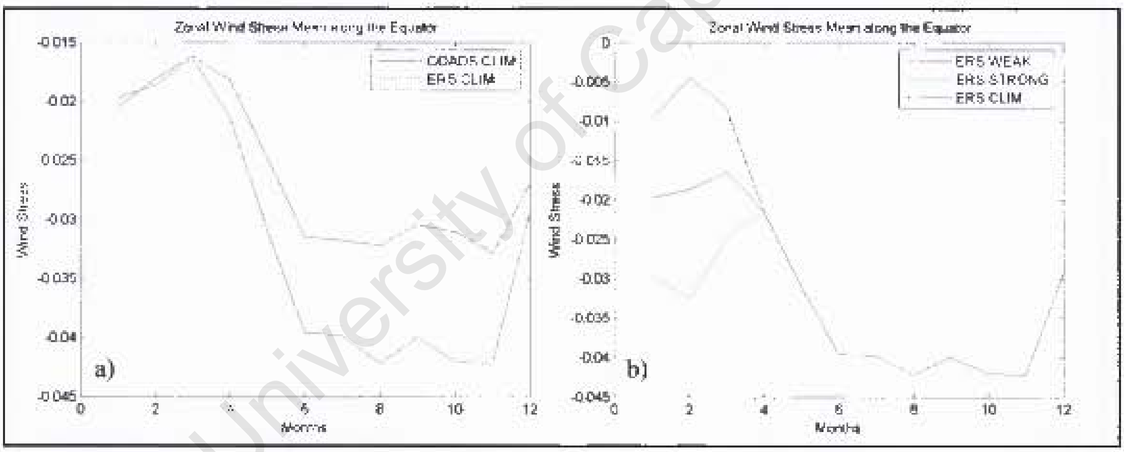

Figure 3.4: Zonal wind stress averaged along the equator, a) COADS and ERS climatologies time series and b) ERS CLIM, WEAK and STRONG time series.

	COADS CLIM	ERS CLIM	ERS WEAK	ERS STRONG
Duration (years)	10	10	1	1
Surface Forcing (heat and salt fluxes)	COADS	COADS	COADS	COADS
Surface Forcing (wind stress)	COADS	ERS	ERS artificial weakening	ERS artificial strengthening
Initial Conditions (currents)	0 ms^{-1}	0 ms^{-1}	ERS CLIM FIELDS	ERS CLIM FIELDS
Initial Conditions (temp. & sal.)	WOA01	WOA01	ERS CLIM FIELDS	ERS CLIM FIELDS
Boundary Conditions (currents)	Geostrophy (ref. level 500m)	Geostrophy (ref. level 500m)	Geostrophy (ref. level 500m)	Geostrophy (ref. level 500m)
Boundary Conditions (temp. & sal.)	WOA01	WOA01	WOA01	WOA01
Validation/Comparison (temp. & sal.)	Levitus 2001	Levitus 2001	ERS CLIM	ERS CLIM
Validation/Comparison (currents)	Lumpkin 2005	Lumpkin 2005	ERS CLIM	ERS CLIM

Table 3.21: Summary the different simulation configurations and settings used to carry out the entire investigation.

3.3 Datasets

The datasets used to validate the model results are the **WOA01** dataset for temperature and salinity and **Lumpkin 2005** dataset (Lumpkin and Garraffo, 2005) for the surface currents.

The monthly data from **WOA01** have a 1° latitude and 1° longitude with a global coverage at various depths: 0.0m, 10.0, 20.0, 30.0, 50.0, 75.0, 100.0, 125.0, 150.0, 200.0, 250.0, 300.0, 400.0, 500.0, 600.0, 700.0, 800.0, 900.0, 1000.0, 1100.0, 1200.0, 1300.0, 1400.0 and 1500.0m. *NODC (Levitus) World Ocean Atlas 2001 data provided by the NOAA-CIRES Climate Diagnostics Center, Boulder, Colorado, USA, from the website htpp://www.cdc.noaa.go/.*

The **Lumpkin 2005** dataset (Lumpkin and Garraffo, 2005) contains global near-surface currents and SST global field with a 1° resolution (from 1° to 360° and from 70°S to 70°N). The dataset is derived from satellite-tracked surface drifting buoy observations from the *Global Drifter Program* and provides monthly mean climatology for U, V and STT (observed variables). The north and eastward Ekman removed speeds (U_g/V_g) are also available and were computed subtracting local wind stress (from NCEP/NCAR reanalysis) and Coriolis parameter. *Lumpkin 2005 data provided by the AOML–NOAA from the website:*

http://www.aoml.noaa.gov/phod/dac/drifter_climatology.html

3.4 Methods

Different methods were applied to the results obtained from the two control simulations and the sensitivity simulations. In both control simulations, temperature, salinity and velocity field climatologies were computed using the last eight years of the 10-year simulations. In the sensitivity experiments the anomalies were calculated using as a reference the ERS CLIM experiment.

In order to evaluate significant differences between the simulations using different climatological wind forcing (COADS and ERS respectively), the sea surface temperature fields from the two control simulations were compared and validated using WOA01 and drifter-derived surface currents.

A key aspect of the project is to investigate various oceanic anomalies (salinity, currents, temperature and zonal transport) and their propagation during Benguela Niños. The analysis was limited between the surface and 200 meters depth. The two sensitivity wind simulations with artificial wind anomalies were compared with the ERS control run at different locations along the equator.

The results obtained are described in detail in the next chapter. **Section 4.1** compares the results of the control simulations (COADS and ERS CLIM) and the observation datasets. In **Section 4.2** the results obtained in the sensitivity study (Benguela Niños/Niñas like events) are described and discussed.

4 Results & Discussion

The results and discussion derived from the model experiments will be presented in this chapter. **Section 4.1** addresses the results of the two control simulations (COADS and ERS CLIM), and a comparison with WOA01 (temperature and salinity) and Drifter-derived climatology of Global Surface Currents (Lumpkin and Garzoli, 2005) will be discussed. The outputs of the simulations will be presented as seasonal composites in horizontal and vertical sections.

In **Section 4.2** the results obtained with the wind sensitivity tests (Benguela Niños and Niñas-like events) will be shown and compared with the control simulation (ERS CLIM). The discussion will be focused on monthly anomalies of temperature, salinity and transport at the surface and along vertical meridional/zonal sections.

4.1 Climatology Simulations

The seasonal cycle of the equatorial and tropical Atlantic obtained by the control simulations is described and compared with WOA01 observations datasets (temperature and salinity) and drifter-derived climatology (surface currents; Lumpkin and Garzoli, 2005). The description of the seasonal cycle of temperature, salinity and currents will be based on the analysis of the sea surface layer, at a section along the equator and the meridional sections along 30°W and 0°E.

The first task performed was to compute and analyse the total and surface kinetic energy (averaged over the entire domain) from the two control simulations, hereafter referred to as COADS CLIM and ERS CLIM (**Figure 4.1**). The kinetic energy is used as a proxy for the model spin-up (model initial adjustment/stabilization), which in both simulations (COADS and ERS CLIM) occurs during the first two years of the simulations' runs. The monthly means (climatologies) were computed for both simulations excluding the spin-up period period. The climatology was then used to compute seasonal composites for: JFM (January, February and March), AMJ (April, May and June), JAS (July, August and September) and OND (October, November and December). It is worth noting to note that by analysing the kinetic energy time series one can observe that both COADS and ERS CLIM represent the biannual cycle of the equatorial and tropical Atlantic.

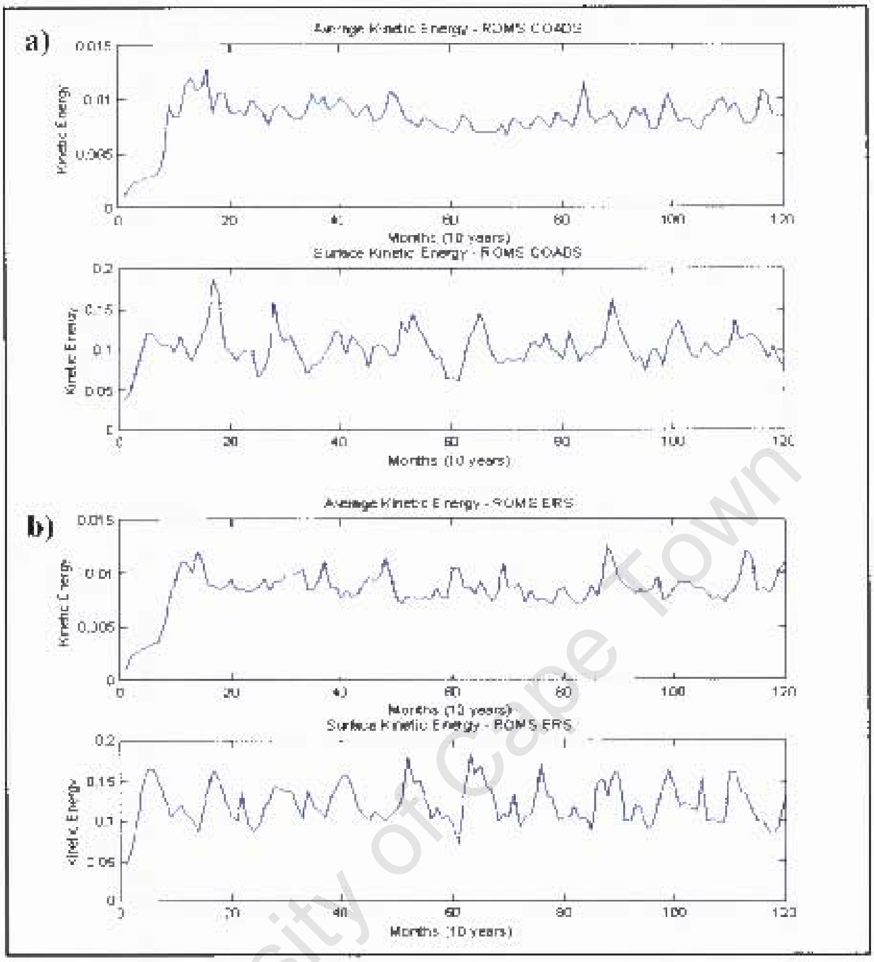

Figure 4.1: a) COADS CLIM: Average kinetic energy over the entire domain (top panel) and surface kinetic energy (bottom panel). b) ERS CLIM: Average kinetic energy over the entire domain (top panel) and surface kinetic energy (bottom panel)

4.1.1 Temperature

The sea surface temperature (SST) annual mean, and the standard deviation from both model outputs (COADS and ERS CLIM) and from the WOA01 dataset are shown in **Figure 4.2**. As can be seen in **Figure 4.2(a),** the model captures the main features of maximum SST variability, i.e. the seasonal equatorial cold tongue in the eastern and central Atlantic (Carton and Zhou, 1997; Grodsky and Carton, 2003) and the horizontal temperature gradients associated with the ABF (e.g., Shannon and Nelson, 1996; Meeuwis and Lutjeharms, 1990). However the model is clearly overestimating the equatorial upwelling that occurs during the austral winter (Carton and Zhou, 1997). In the model outputs the region of the equatorial cold tongue shows SST annual mean values of 25°C and 24°C for the COADS and ERS CLIM respectively, whereas the WOA01 dataset indicates SST annual mean reaches 27°C in the area. The spatial westward extension of the cold tongue (24°C<SST<25°C) is also overestimated by the model, particularly in the ERS CLIM results, where the cold tongue pattern extends as far as 25°W. In the ABF region, both the models and the observations have very similar temperature gradients. In the model results, the low SST values (SST<23°C) associated with the southern/central Benguela cold waters extend as far as 10°W, whereas the observations reveal a westward limit near 5°E. **Figure 4.2(b)** confirms that the areas mentioned above have the highest variability i.e., the eastern and central Atlantic (cold tongue) and the ABF region. The western Atlantic north of the equator has the lowest variability in both the experiments and the observations, with values of 0.5°C. In the eastern Atlantic the variability is higher, with values reaching 3°C.

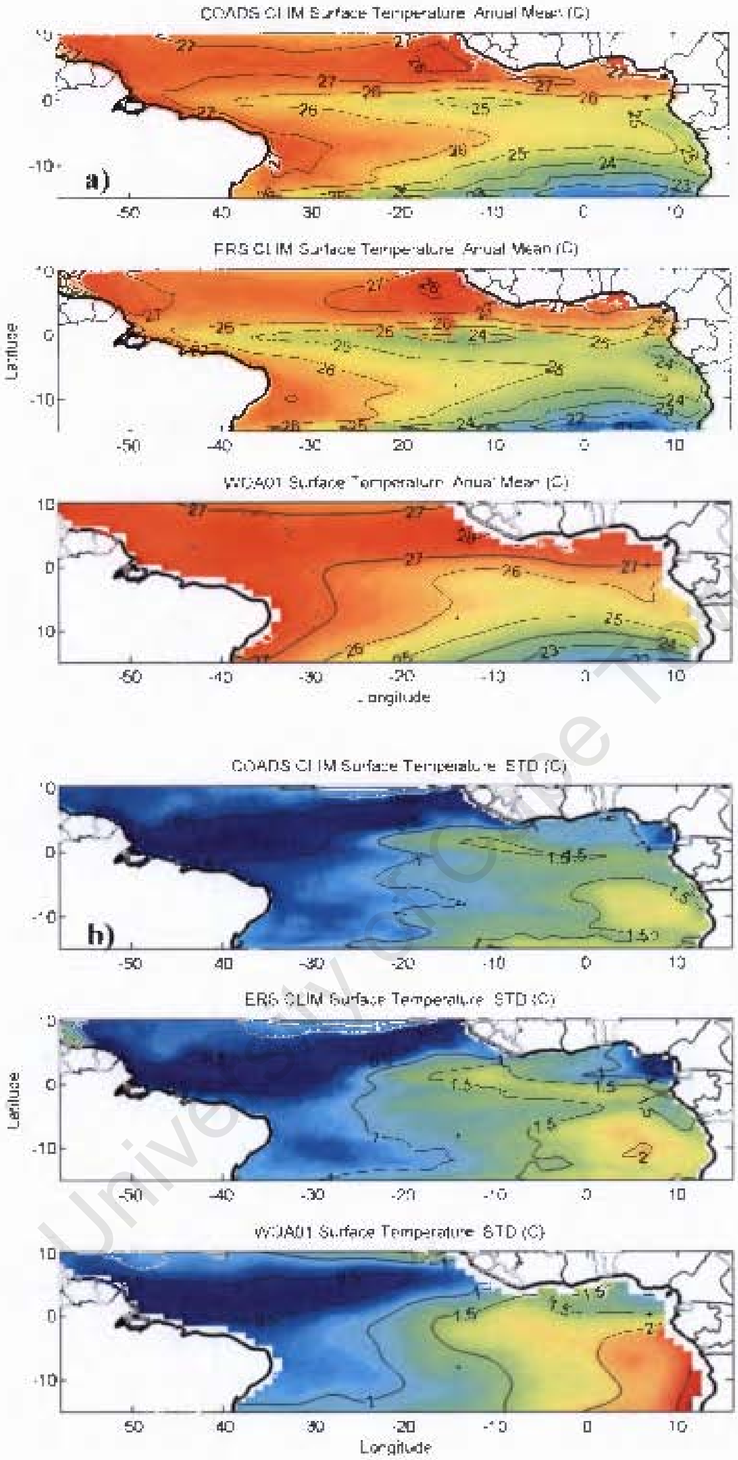

Figure 4.2: a) Sea Surface Temperature Annual mean; b) Sea Surface Temperature Standard Deviation. Top panel for COADS CLIM, middle panel for ERS CLIM and bottom panel for WOA01 (contour 0.5 °C).

Eastern and central equatorial variability (cold tongue)

The variability of the SST over the central and eastern Atlantic is tightly linked to the seasonal cycle of trade winds over this region (Carton and Zhou, 1997). During the austral summer (JFM) the trade winds are weak and, as a result, the equatorial and tropical Atlantic is generally warm. As seen in **Figure 4.3(a)**, both model results show warm water (25°C<SST<27°C) in the eastern and central Atlantic, whereas in the same region the observations show SST values of 28°C. Despite the differences in the SST values between the numerical results and observations, the model captures the general warming of the equatorial/tropical Atlantic observed during JFM.

In AMJ the simulation results reveal a strong cooling along the equator, particularly in the ERS CLIM experiment, where the cold tongue (24°C<SST<23°C) extends as far as 25°W (see **Figure 4.3(b)**). The model results from COADS CLIM exhibit a weaker cooling than ERS CLIM and the cold tongue (SST<24°C) only extends to 15°W. Compared to the numerical results, the observations have higher SST values (27°C<SST<28°C).

During the austral winter (JAS) the strengthening of the trade winds over the eastern Atlantic causes a strong surface divergence, which results in the development of the equatorial cold tongue (Carton and Zhou, 1997). As seen in **Figure 4.3(c)**, this feature is clearly evident in the observations, with SST values lower than 24°C along the eastern and central Atlantic. The results from the model represent the intense upwelling system in the equatorial region, but SSTs are colder by 2°C and 1°C compared to the observations in both the ERS and COADS CLIM runs (see **Figure**

4.3(c)). In both simulation outputs the equatorial cold tongue (24°C<SST<23°C) extends as far as 25°W; the observations, however, reveal a spatial extension as far as 15°W.

In the last quarter of the year (OND), the equatorial upwelling diminishes due to the relaxation of the trade winds, and the observations show a warming of the eastern and central equatorial Atlantic basin (see **Figure 4.3(d)**). The model results also illustrate a warming over these regions, but with SST values are slightly colder ($\sim 1°C$) than the observations.

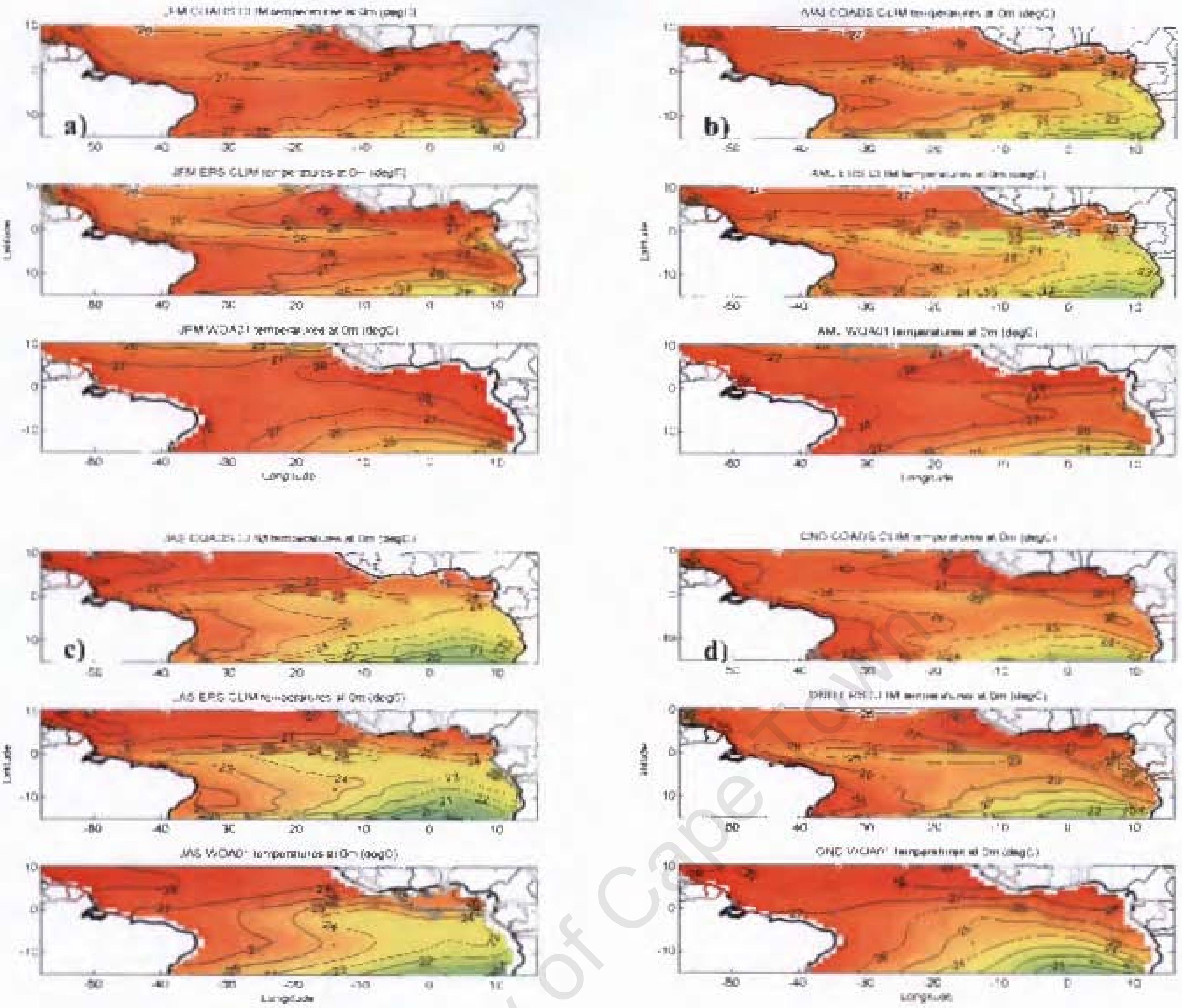

Figure 4.3: Sea Surface Temperature seasonal mean a) JFM, b) AMJ, c) JAS and e) OND. Top panel for COADS CLIM, middle panel for ERS CLIM and bottom panel for WOA01 (contour 0.5 °C).

Equatorial Thermocline

The seasonal variability of the temperature field in a vertical section along the equator is shown in **Figure 4.4**. The numerical results illustrate a well-represented equatorial thermocline structure, i.e. deeper in the western equatorial Atlantic than in the eastern equatorial Atlantic. However, the thermocline depth is not the same for the two simulations and also differs to the observations.

Figure 4.5 illustrates a more detailed seasonal variation of thermocline depths along the equator. During JFM (see **Figure 4.5(a)**) the ERS CLIM thermocline is generally shallower than COADS CLIM and WOA01. The difference between ERS and COADS CLIM thermocline depths reaches a maximum value of ~40 metres and the WOA01 thermocline lies between the other two.

As seen in **Figure 4.4(b)** and **Figure 4.5(b)**, in AMJ there is an obvious steep shallowing of the thermocline in the eastern Atlantic (with deepening in the western Atlantic) and cooler temperatures in the mixed layer for both ERS and COADS CLIM results. In contrast, the observations reveal a near-horizontal thermocline structure and warm temperatures in the mixed layer. **Figure 4.5(b)** shows that the thermocline uplift resulting form equatorial upwelling, begins to develop during AMJ in the model results, whereas in the observations this process becomes evident only from JAS.

During JAS the 20°C isotherm from the observations is shallower in the eastern Atlantic, where the equatorial upwelling system uplifts the thermocline to a depth of 40m (see **Figure 4.4(c)** and **Figure 4.5(c)**). It is important to note that between the two simulated temperature fields along the equator, COADS CLIM results exhibit a deeper thermocline than ERS CLIM.

In the austral spring (OND) the vertical section along the equator reveals that the COADS CLIM 20°C isotherm is remarkably similar to the observations, while that the thermocline of the ERS CLIM is shallower (see **Figure 4.5(d)**. In OND the observations suggest a deepening of the thermocline in the eastern Atlantic, whereas the western Atlantic thermocline does not undergo significant changes. In contrast, the ERS CLIM exhibits a deepening of the thermocline in the western Atlantic from JAS to OND.

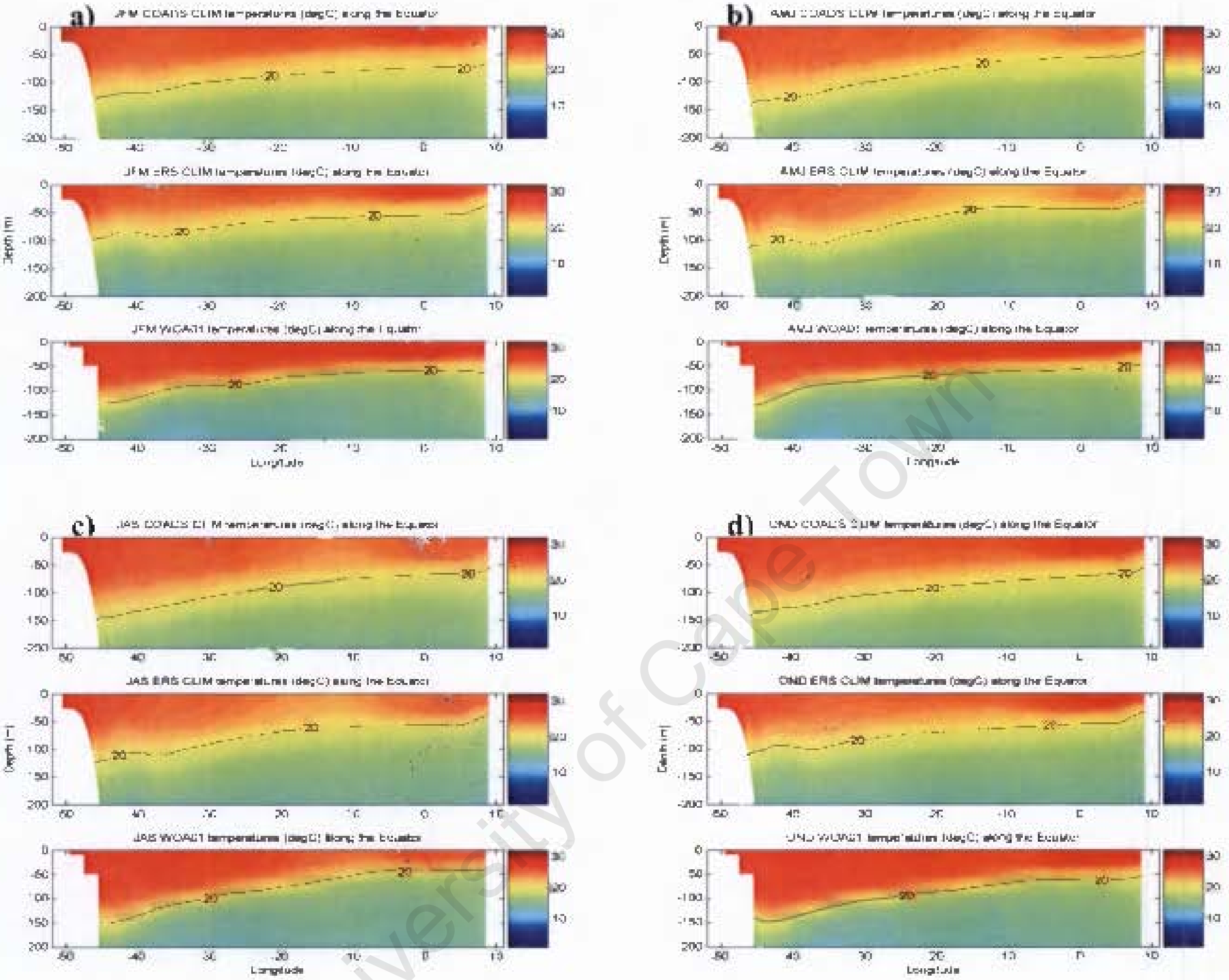

Figure 4.4: Vertical section of temperature along the equator, seasonal mean a) JFM, b) AMJ, c) JAS and d) OND. Top panel for COADS CLIM, middle panel for ERS CLIM and bottom panel for WOA01 (contour 20 °C isotherm).

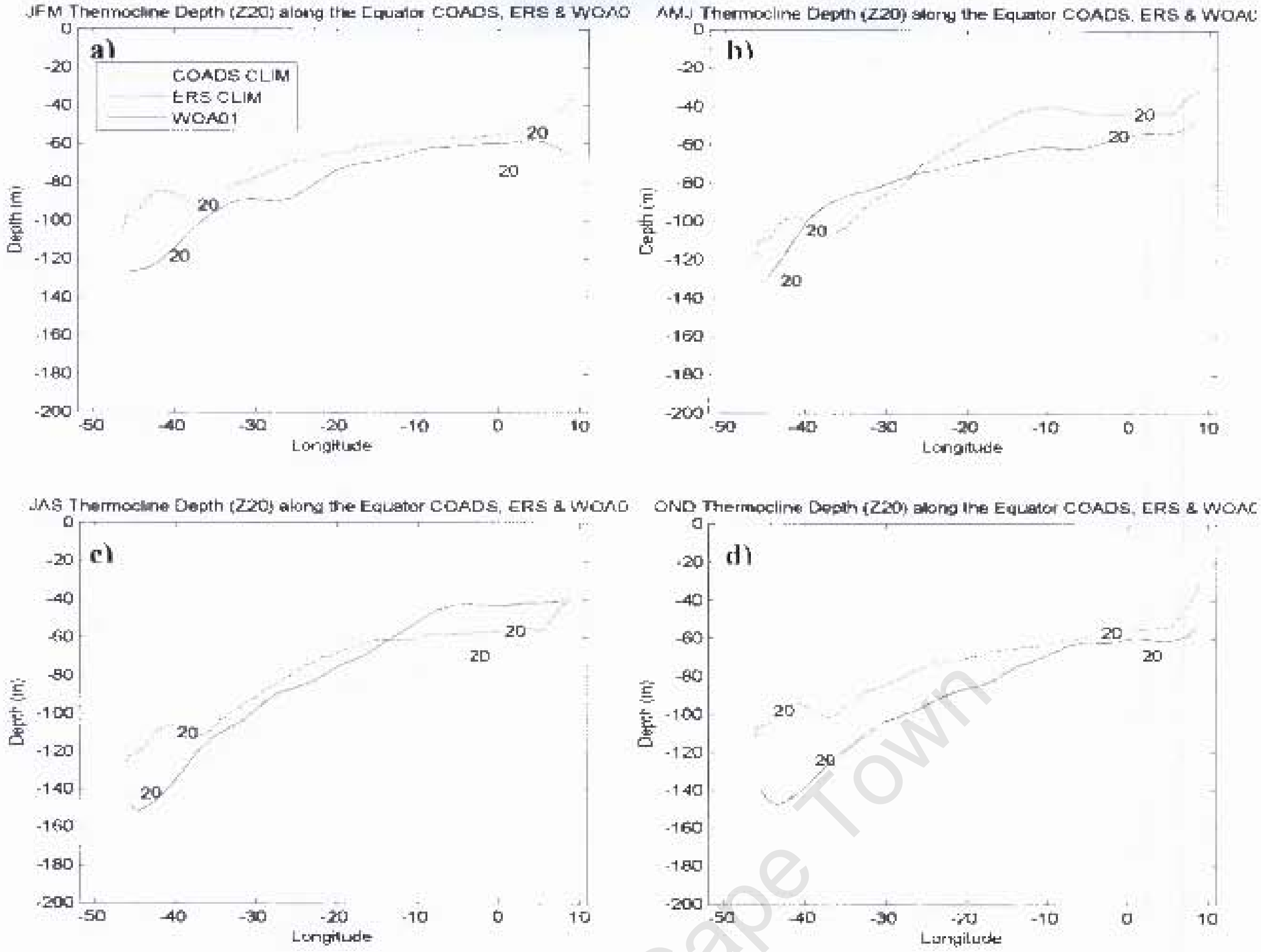

Figure 4.5: Thermocline depth along the equator, seasonal mean a) JFM, b) AMJ, c) JAS and d) OND. Top panel for COADS CLIM, middle panel for ERS CLIM and bottom panel for WOA01 (contour 20 °C isotherm).

4.1.2 Salinity

Figure 4.6(a) illustrates the sea surface salinity (SSS) annual mean and standard deviation from model outputs (COADS and ERS CLIM) and from the WOA01 dataset. The main features related to the SSS variability are captured by the model in both experiments. In the western Atlantic basin, the fresh water tongue associated with the Amazon River is clearly present (Levitus, 1986; Dessier and Donguy, 1994). In the eastern Atlantic, the SSS minimum at 8°N and east of 20°W, which is linked to heavy strong rainfall caused by ITCZ meridional migration, is also visible in the two simulations (Levitus, 1986; Dessier and Donguy, 1994). Further south, the fresh water pool resulting from to the Congo River and Biafra Bay is evident (Levitus, 1986;

Dessier and Donguy, 1994). As can be seen in **Figure 4.6(b)**, the areas of highest variability reproduced by the model are the ones mentioned above. In the western Atlantic the highest SSS variability has values of 3*psu* while in the eastern Atlantic the variability is lower with SSS values of 1*psu*.

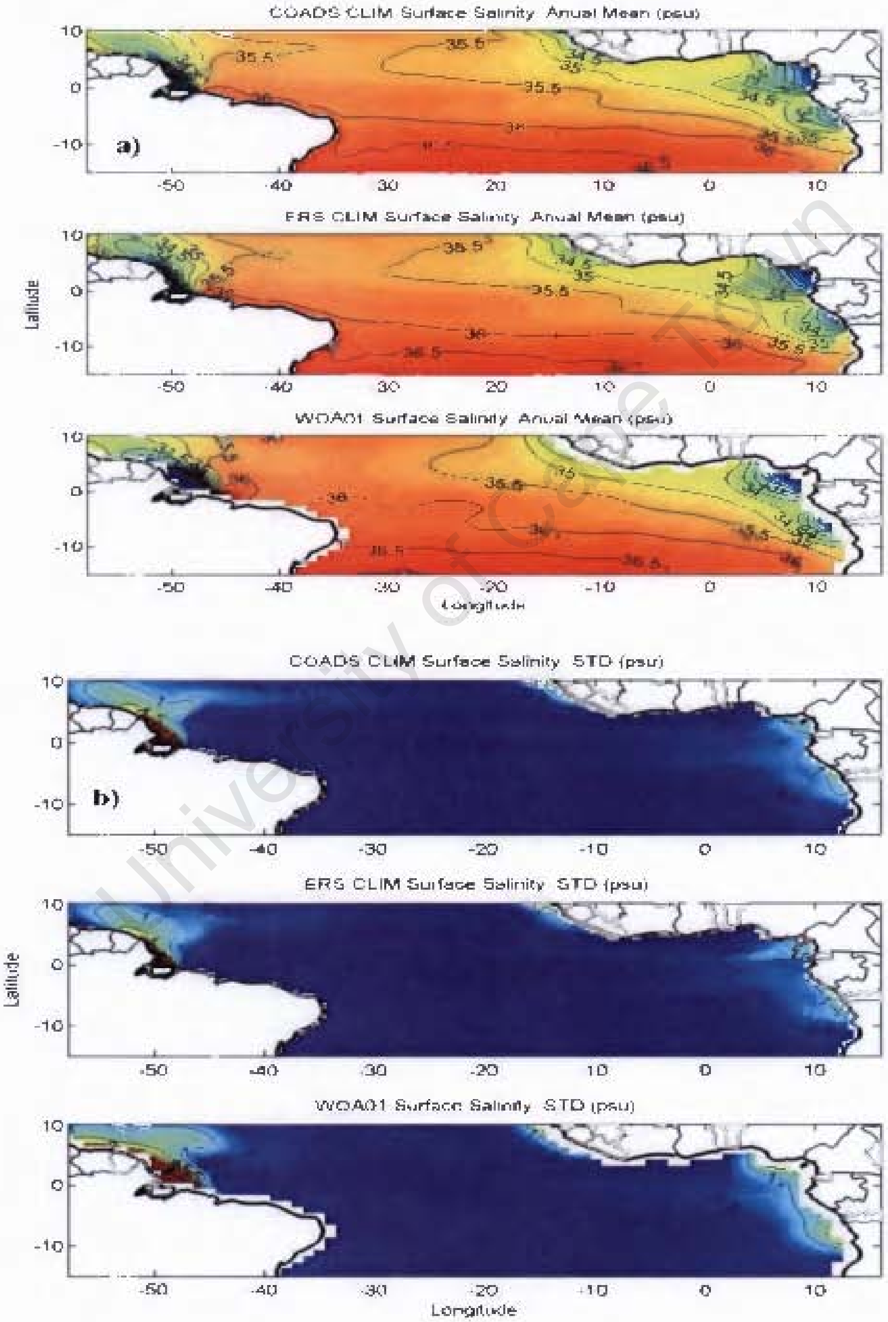

Figure 4.6: a) Surface Salinity Annual mean; b) Surface Salinity Standard Deviation. Top panel for COADS CLIM, middle panel for ERS CLIM and bottom panel for WOA01 (contour 0.5 *psu*).

Amazon River freshwater plume

As seen in **Figure 4.7(a)** the Amazon freshwater plume signature (SSS<35*psu*) is present in the austral summer (JFM). However, in both experiments the spatial extension of the plume is overestimated. In the observations the plume is constrained to the area of the river mouth, but the simulation outputs show the plume extending as far as 10°N. In the vertical section along the equator, the freshwater plume is apparent near the Amazon River in COADS and ERS CLIM (see **Figure 4.8(a)**). In the observations this plume is masked by the coarse shelf resolution. Nevertheless the 36*psu* isohaline associated with the Equatorial Undercurrent (EUC) is evident from the Brazilian coast extending as far as 15°W. The numerical outputs underestimate the spatial extension of the EUC signature to 25°W and 35°W for the COADS and ERS CLIM respectively.

In the second quarter of the year (AMJ) the Amazon River reaches its maximum runoff, i.e. three months after the January floods (Masson and Delecluse, 2001). The minimum SSS and the maximum spatial extension are visible both in the model outputs and in observations (see **Figure 4.7(b)**). During this season the plume extends as far as 10°N and the simulations and observations are in agreement.

During the austral winter (JAS) the Amazon River runoff decreases and the NBC retroflection advects the freshwater plume into the NECC, which in turn creates a zonal belt of <36 *psu* north of the equator, extending from the Amazon River coastal area to the African coast (Dessier and Donguy, 1994; Masson and Delecluse, 2001;

Delcroix *et al.*, 2005). The model reveals a reduction of the spatial extension of the freshwater plume and the SSS gradients are weak and constrained to an area close to the coast (see **Figure 4.7(c)**). In contrast the observations exhibit greater northward spatial extension and stronger SSS gradients. Despite the poor representation of the Amazon plume, the zonal salinity belt (<36 *psu*) north of the equator is clearly seen in the model results from JAS to OND.

In OND, the Amazon River runoff is at its minimum and its associated plume is limited to the coastal area around the river mouth. During this season the simulation results are in agreement with the WOA01 SSS observations.

Biafra Bay and Congo River freshwater plumes

In the eastern Atlantic basin during JFM the model exhibits similar SSS patterns to the observations, and the SSS minimum associated with the Congo River and Biafra Bay is visible (see **Figure 4.7(a)**). **Figure 4.8(a)** depicts the salinity field in a section along the equator and in both the simulation results and observations the Biafra Bay freshwater plume core (salinity<34*psu*), extending as far as 0°E and reaching depths of 50m, is apparent.

As seen in **Figure 4.7(b),** during AMJ the freshwater plumes related to the Biafra Bay and the Congo River are reduced, particularly in the numerical results where the SSS minimum is mainly limited to the coastal areas. This is also evident in the vertical section along the equator, where the salinity minimum core (salinity<34 *psu*) is limited to the shelf area and gradually, due to mixing processes, becomes saltier (34< *psu* <35) as it moves offshore (see **Figure 4.8(b)**).

In JAS the observations show that the Biafra Bay and the Congo River plumes reach their minimum spatial extension and SSS gradient values, corresponding to the dry season in this region (see **Figure 4.7(c)**). The vertical section along the equator confirms the spatial extension of the salinity minimum in the observations, and the Biafra Bay plume (34< *psu* <35) can be seen east of 0°E and limited to the surface. In the model results, both COADS and ERS CLIM reveal that the plume has a deeper signature and has a greater spatial extension than in the observations. During the austral winter (JAS), in the area around 10°W and 8°N, a pool of fresh water is present on the salinity surface fields of both numerical simulations and of the observations (see **Figure 4.7(c)**). This freshwater pool is associated with the meridional migration of the ITCZ, which during this season lies over the region, enhancing precipitation (Yoo and Carton, 1990).

Figure 4.7(d) illustrates the SSS field in OND, and it is apparent that in the eastern Atlantic basin the model results and observations are in agreement. The Biafra Bay and Congo River plumes reach greater offshore spatial extension than in JAS, which resulting from the December floods (Dessier and Donguy, 1994). This is also evident in **Figure 4.8(d)**, where the zonal extension of the plume along the equator reaches 0°E in the observations and extends further west in the results from the model. The freshwater pool around 10°W-8°N, formed as a result of increased rainfall associated with the ICTZ migration, is still evident in the both simulations and observations (see **Figure 4.7(d)**).

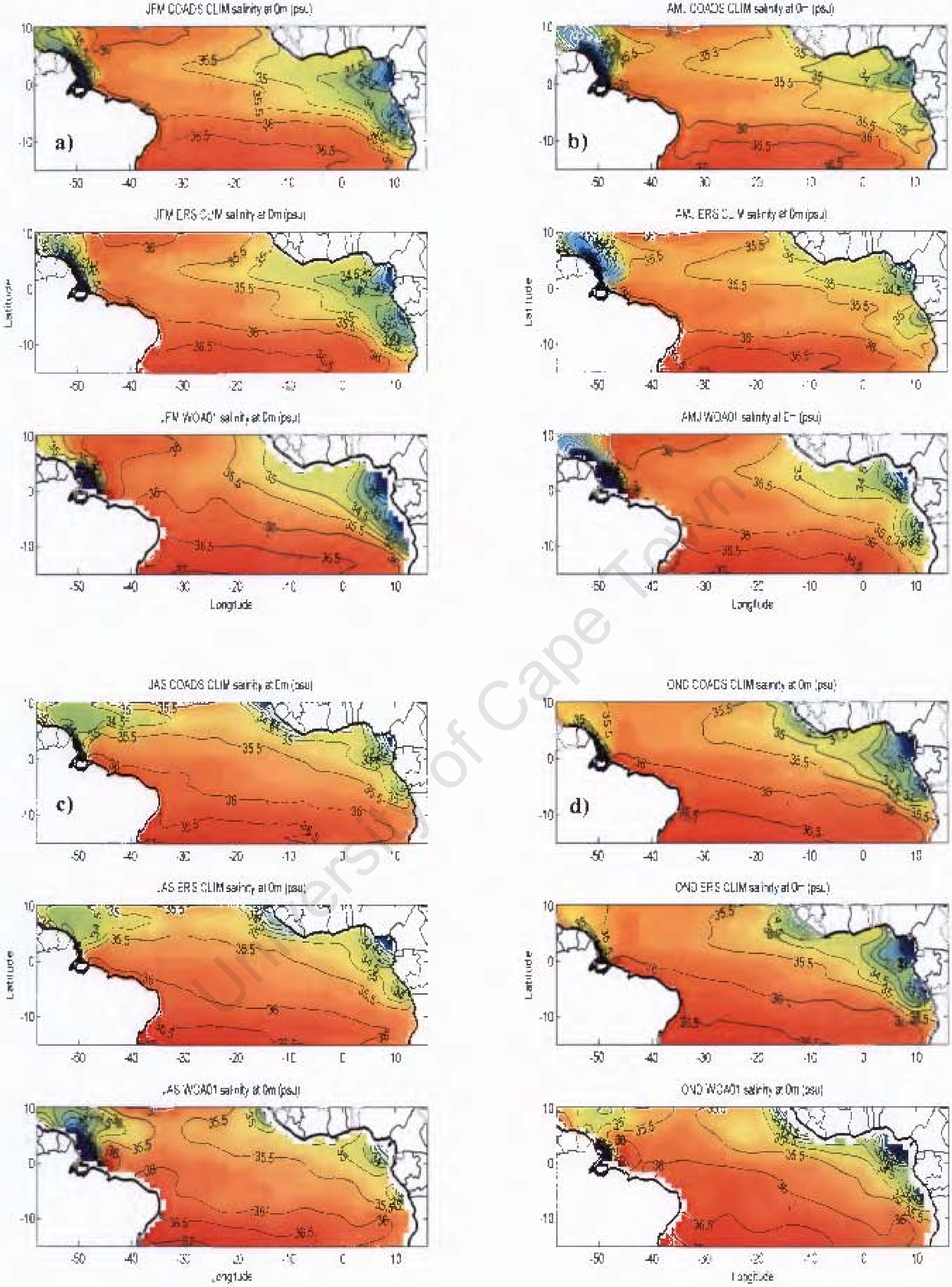

Figure 4.7: Sea Surface Salinity seasonal mean, a) JFM, b) AMJ, c) JAS and e) OND. Top panel for COADS CLIM, middle panel for ERS CLIM and bottom panel for WOA01 (contour 0.5 *psu*).

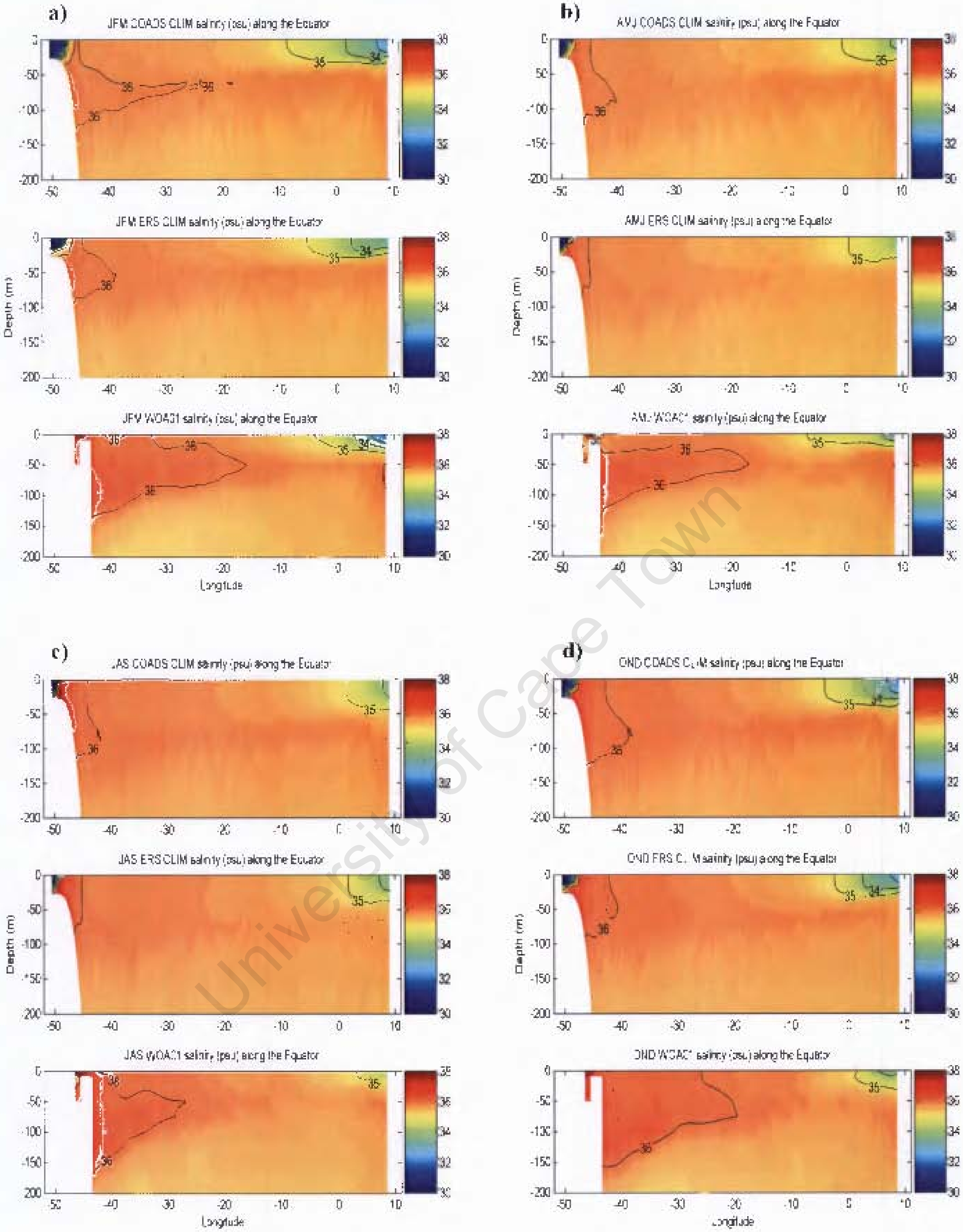

Figure 4.8: Vertical section of salinity along the equator, seasonal mean: a) JFM, b) AMJ, c) JAS and d) OND. Top panel for COADS CLIM, middle panel for ERS CLIM and bottom panel for WOA01 (contour 0.5 *psu*).

4.1.3 Velocity

The surface velocity annual mean is shown in **Figure 4.9** and **Figure 4.10(a-b)**. The zonal flow band associated with the SEC south, central and north branches is present between 15°S and 5°N in both COADS and ERS CLIM results. However, the numerical results do not give a clear separation of the central and north branches of the SEC in the western Atlantic, which is visible in the observations. Near the Brazilian coast (2°S) the simulation outputs have a stronger central SEC (0.4ms^{-1}) compared to the observations (0.2ms^{-1}).

The NBC is represented in both model experiments and is in agreement with the observations as far as the Amazon River mouth. North of the Amazon River mouth the model tends to overestimate the NBC, implying that the NBC retroflection occurs as far as 10°N-55°W, whereas it was expected to occur around 5°N and between 45°W-50°W (Johns *et al.*, 1998).

North of 5°N, the eastward NECC and GC are clearly evident in the observations as a zonal flow of 0.2ms^{-1} and 0.5ms^{-1} respectively. The simulation results have a slightly weaker NECC and GC. In the south-eastern Atlantic the results from the model show a weak northward flow (0.2ms^{-1}).

In contrast the observations show a weak AC southward flow (0.2ms^{-1}). As seen in **Figure 4.11(a-b),** the currents that exhibit a highest variability are the nSEC, NECC and GC in both model and observations. However the model results show lower variability than the observations particularly in the nSEC/NECC system.

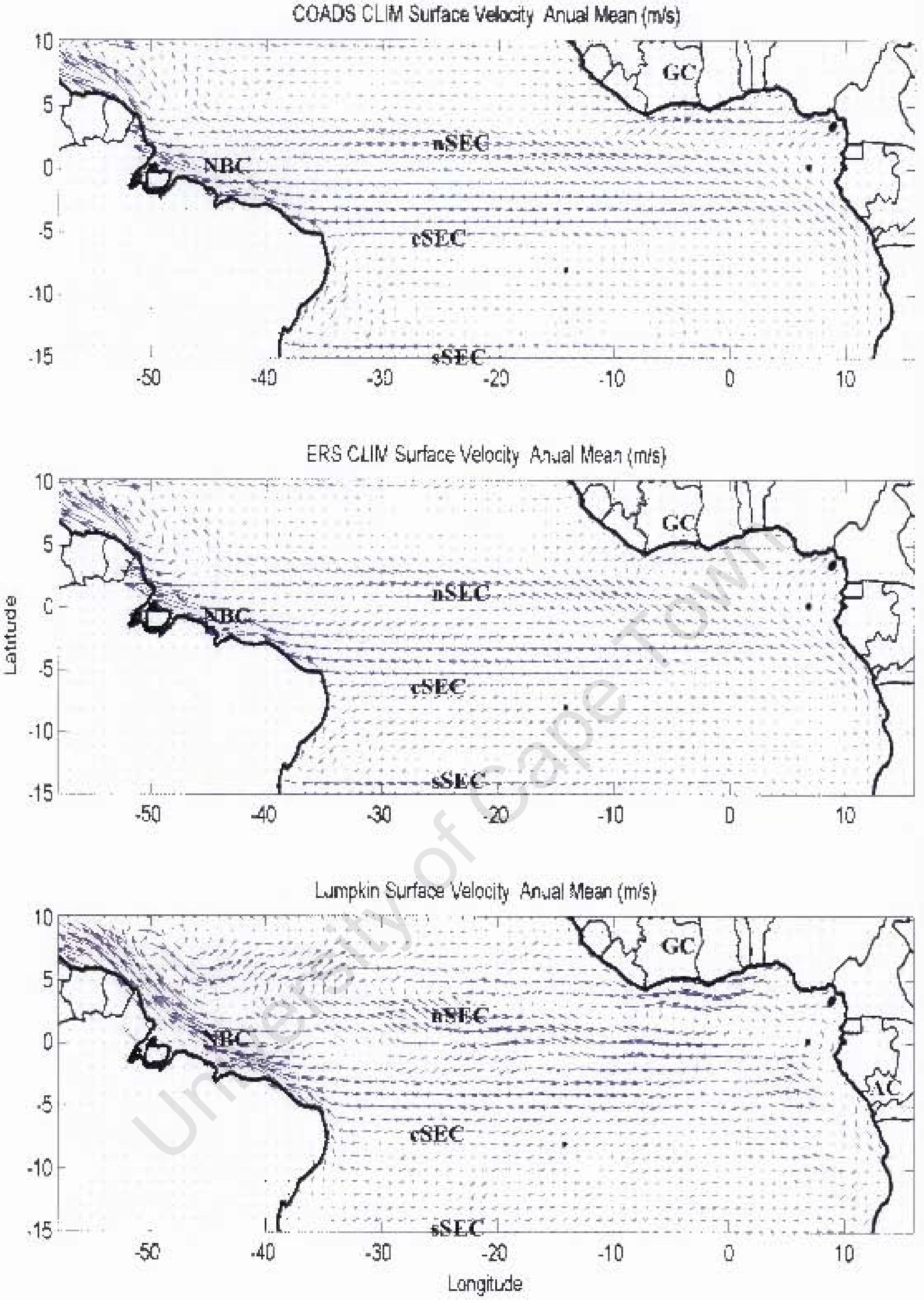

Figure 4.9: Surface Velocity Annual mean quiver. Top panel for COADS CLIM, middle panel for ERS CLIM and bottom panel for Lumpkin 2005 drifter-derived climatology of Global Surface Currents (ms^{-1}). Shown are: North Equatorial Countercurrent (NECC), the Guinea Current (GC), the South Equatorial Current (SEC) with the northern (nSEC), central (cSEC) and southern branches (sSEC), the North Brazil Current (NBC), the Angola Current (AC).

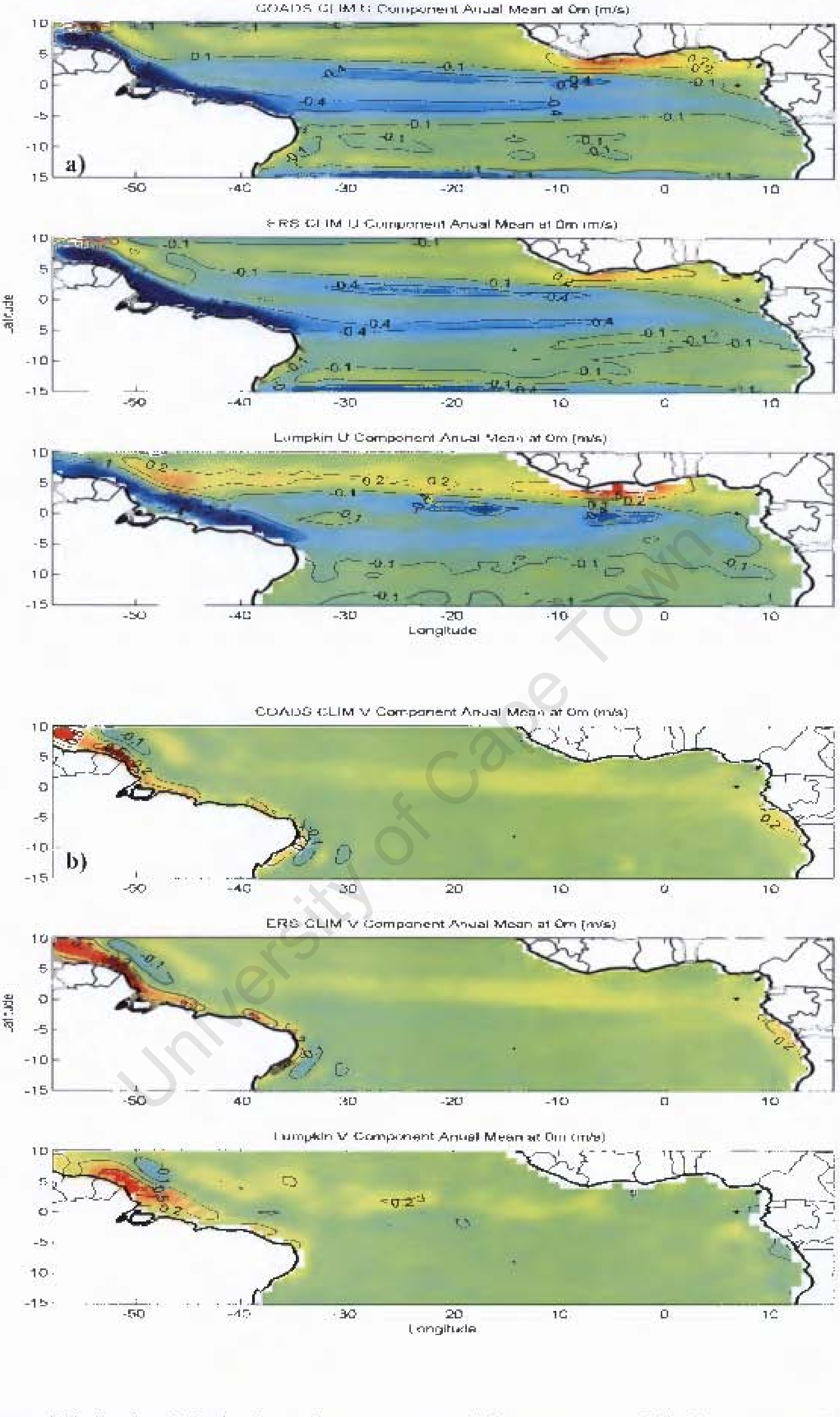

Figure 4.10: Surface Velocity Annual mean contour. a) U component and b) V component. Top panel for COADS CLIM, middle panel for ERS CLIM and bottom panel for Lumpkin 2005 drifter-derived climatology of Global Surface Currents (contour interval 0.1ms^{-1}, positive values correspond to eastward or northward flow).

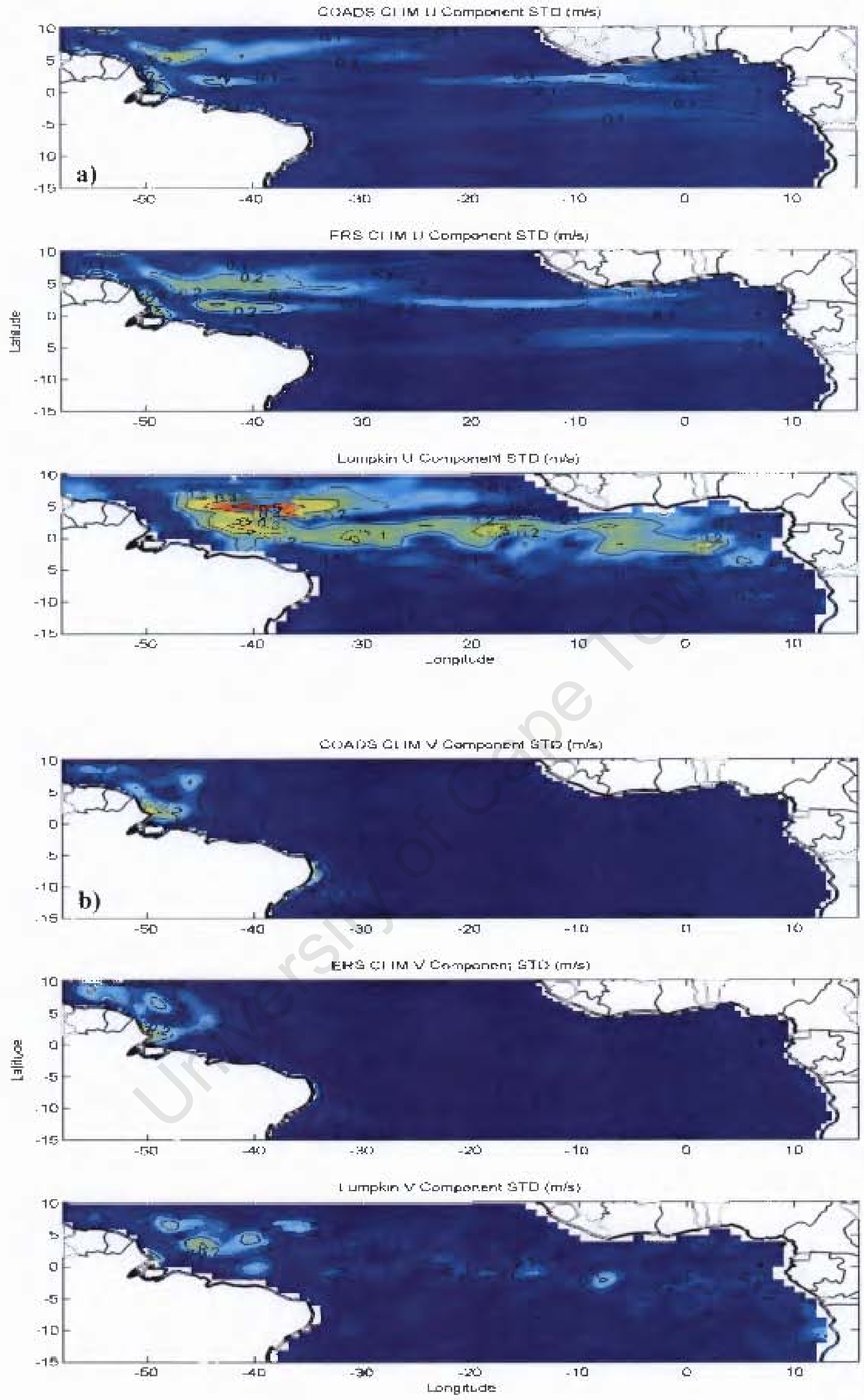

Figure 4.11: a) Surface U component Standard Deviation; b) Surface V component Standard Deviation. Top panel for COADS CLIM, middle panel for ERS CLIM and bottom panel for Lumpkin 2005 drifter-derived climatology of Global Surface Currents (contour interval $0.1 ms^{-1}$).

Western and Central Atlantic basin

The observations reveal a clear zonal eastern flow from the NBC retroflection region to the African promontory, where the NECC merges with the GC (see **Figure 4.12(a)**). The model results are not in agreement with these observations in that a stronger NBC is found along the northern Brazilian coast. The position of the NBC retroflection is also farther north-west than in the observations (**Figure 4.12(a)** and **Figure 4.13(a)**). Consequently, the presence of the NECC is not visible in the model results during the austral summer.

During AMJ, the simulation results and the observations reveal a well-developed NECC/GC system (see **Figure 4.12(b)** and **Figure 4.13(b)**). However, both COADS and ERS CLIM results show that the NBC north-westward flow and its retroflection are found approximately south of 10°N and west of 50°W. As seen in **Figure 4.12(b)**, in AMJ the observations have a less well-defined nSEC and cSEC compared to the numerical outputs.

In the austral winter the NBC in the observations is weaker in the retroflection region and, consequently, the NECC in the western Atlantic is replaced by the nSEC westward flow (see **Figure 4.12(c)**). During this season the model results differ from the observations, particularly with respect to the position of the NECC. The simulation outputs show a clear NECC (but it is weaker than in AMJ) between 5°N-10°N and from the NBC retroflection region to 10°W.

From JAS to OND the observations reveal an intensification of the cSEC, the presence of a stronger eastward flow between the cSEC/nSEC system, and the NECC flow signature only visible east of 20°W (see **Figure 4.12(d)**). In contrast, in the model results the cSEC/nSEC system is clearly visible, there is no evidence of an eastward flow between cSEC and nSEC, and the presence of the NECC is very weak (**Figure 4.12(d)**).

Eastern Atlantic basin

The seasonal intensification of the GC during JFM in the drifter-derived climatology ($0.5ms^{-1}$) is not represented by the model (see **Figure 4.12(a)**). In the south-eastern Atlantic the observations indicate a weak surface poleward flow associated with the AC (**Figure 4.13(a)**). However, the model generates a surface northward current instead of a southward current and fails to represent the AC at the surface. **Figure 4.14(a)** depicts the velocity meridional component in a vertical section along 10°S, and the numerical results show a weak ($0.1ms^{-1}$) subsurface poleward flow.

In AMJ the conditions observed at the surface in the south-eastern Atlantic are very similar to those observed in the austral summer (JAS) (see **Figure 4.13(b)**). The GC in the numerical results reaches its maximum values ($0.5ms^{-1}$) during AMJ. By inspecting the vertical section along 10°S both results from the model reveal a broader AC flow ($0.1ms^{-1}$) near the coast (see **Figure 4.14(b)**)..

During the austral winter the GC is clearly evident in the observations, with velocities of $0.5ms^{-1}$ (see **Figure 4.12(c)**). The ERS CLIM results exhibit a weaker GC ($0.3ms^{-}$

^{1}), compared to COADS CLIM (0.4ms^{-1}). In JAS the drifter-derived surface current observations show a strengthening of the AC at the surface (see **Figure 4.12(c)**). In this season neither COADS nor ERS CLIM produce the AC at the surface (see **Figure 4.13(c)**), and the subsurface signature of the AC (0.1ms^{-1}) is a narrow flow confined to the coast (**Figure 2.14(c)**).

In OND the GC reflected by the simulations is in accordance with the observations, particularly the results obtained by COADS CLIM, although the results obtained by ERS CLIM tend to underestimate the current (see **Figure 4.12(d)**). From JAS to OND the simulation results are not significantly different for the AC.

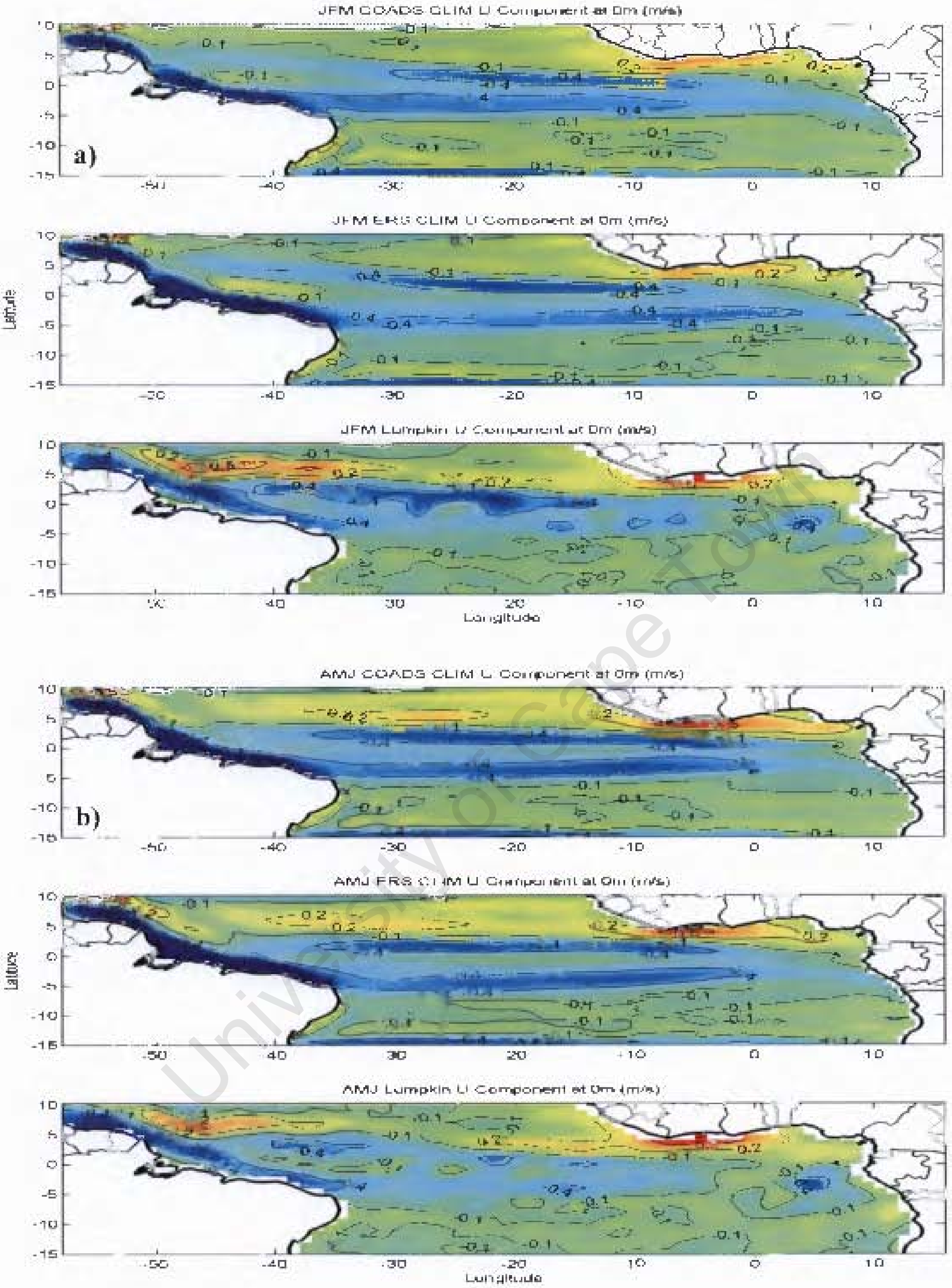

Figure 4.12: Surface U component seasonal mean, a) JFM and b) AMJ. Top panel for COADS CLIM, middle panel for ERS CLIM and bottom panel for Lumpkin 2005 drifter-derived climatology of Global Surface Currents (contour interval 0.1ms^{-1}, positive values correspond to eastward or northward flow).

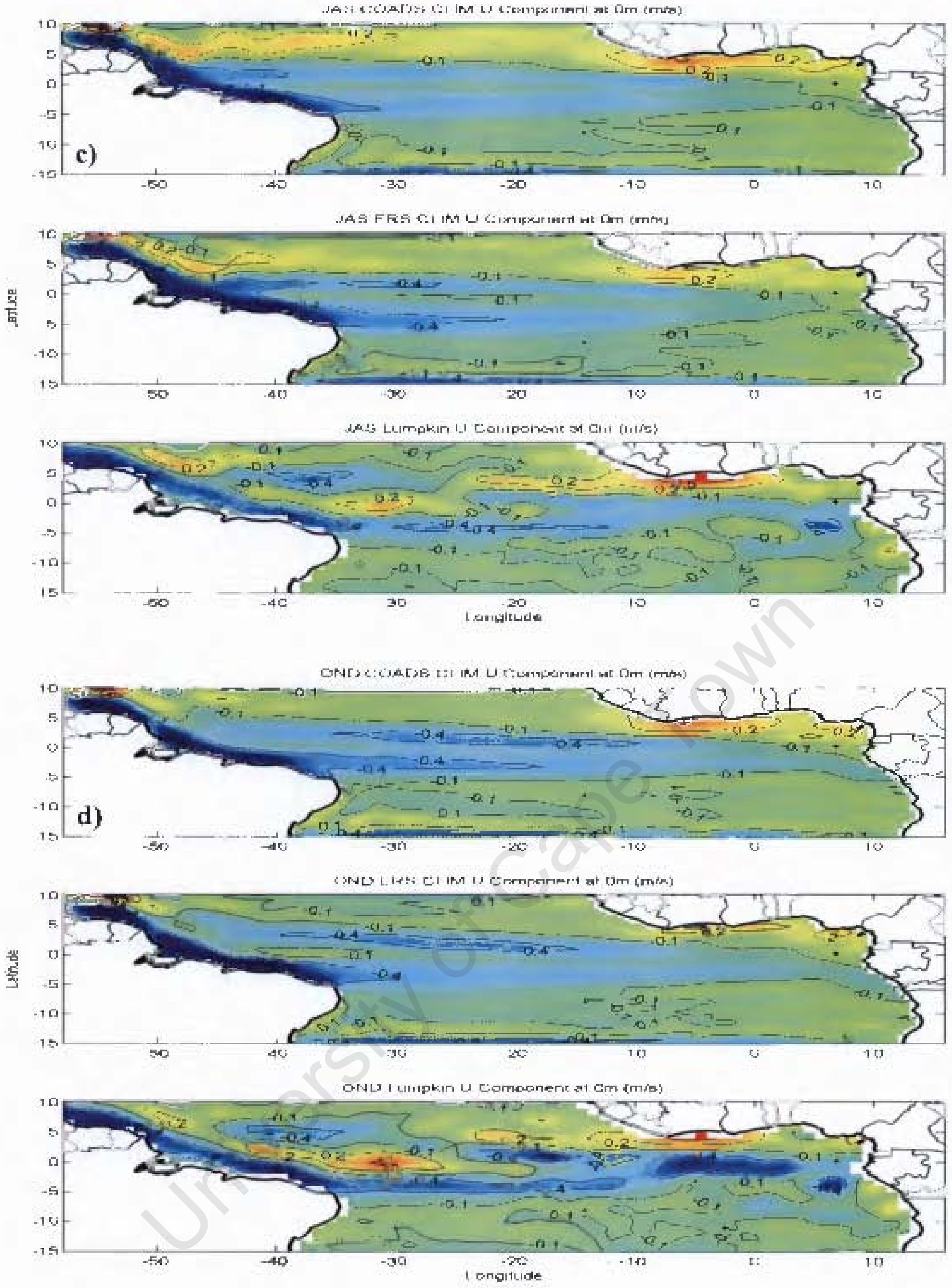

Figure 4.12: cont., c) JAS and d) OND. Top panel for COADS CLIM, middle panel for ERS CLIM and bottom panel for Lumpkin 2005 drifter-derived climatology of Global Surface Currents (contour interval 0.1ms^{-1}, positive values correspond to eastward).

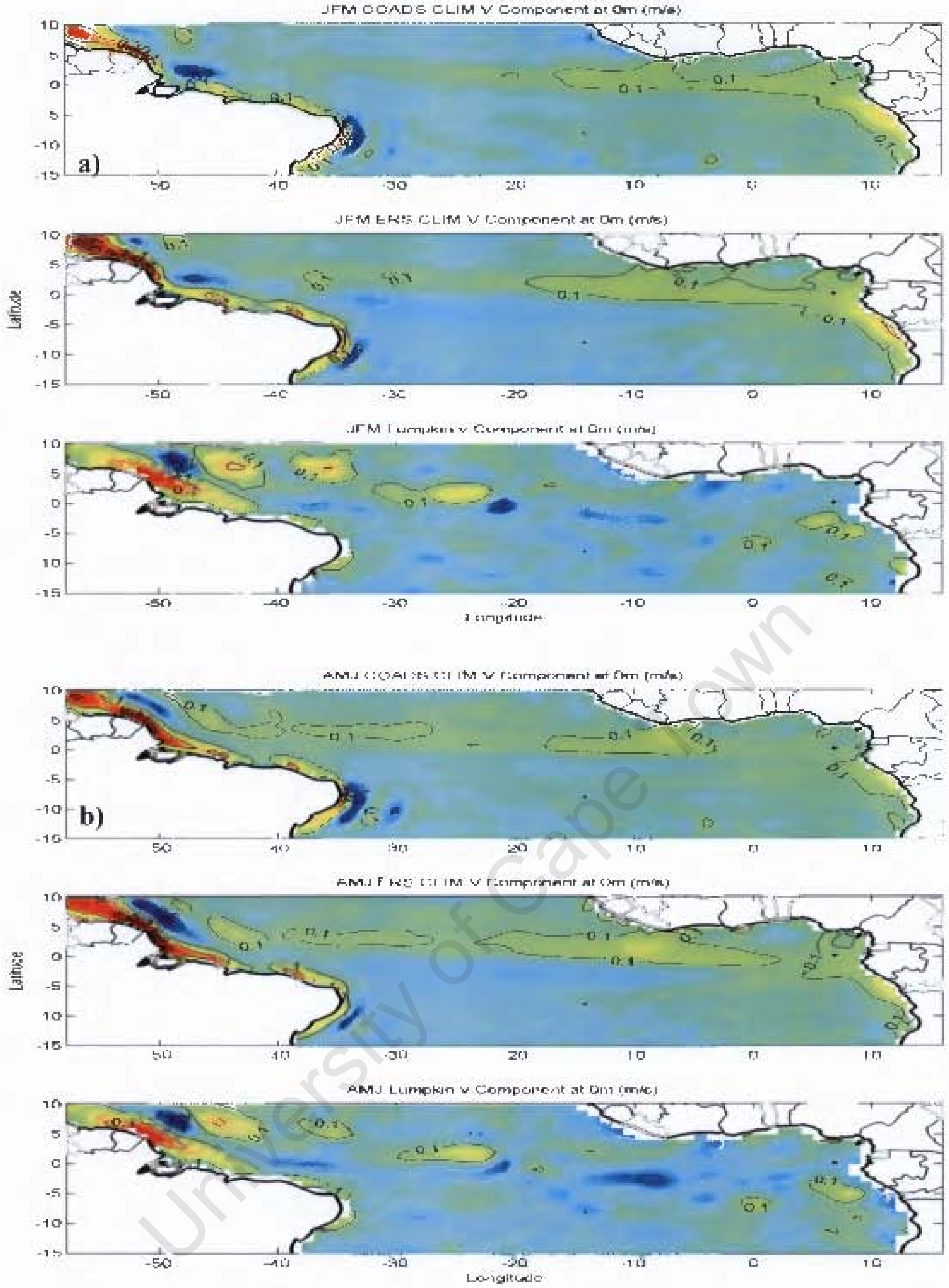

Figure 4.13: Surface V component seasonal mean, a) JFM and b) AMJ. Top panel for COADS CLIM, middle panel for ERS CLIM and bottom panel for Lumpkin 2005 drifter-derived climatology of Global Surface Currents (contour interval 0.1ms^{-1}, positive values correspond to eastward or northward flow).

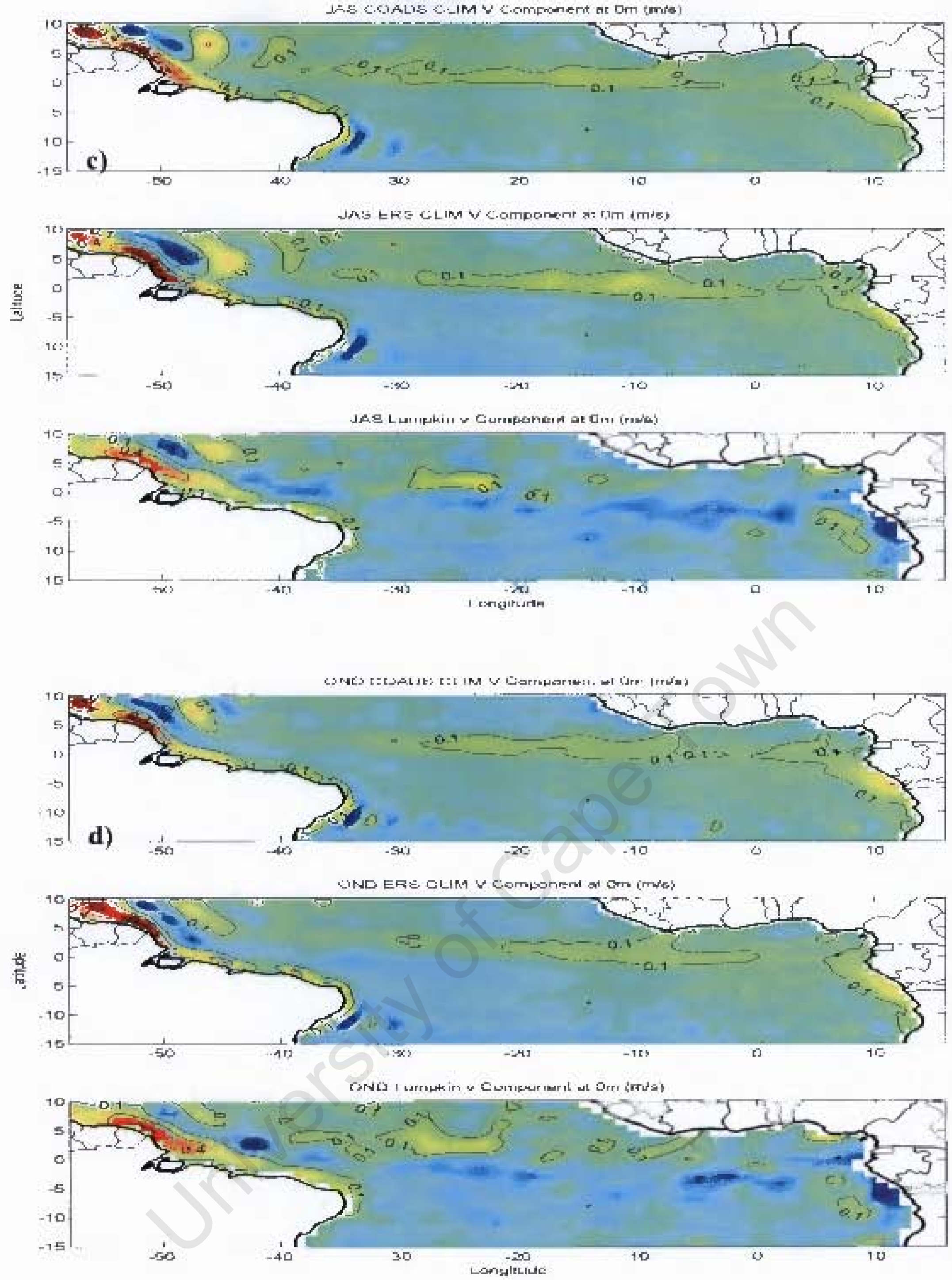

Figure 4.13: cont., c) JAS and d) OND. Top panel for COADS CLIM, middle panel for ERS CLIM and bottom panel for Lumpkin 2005 drifter-derived climatology of Global Surface Currents (contour interval 0.1ms^{-1}, positive values correspond to eastward or northward flow).

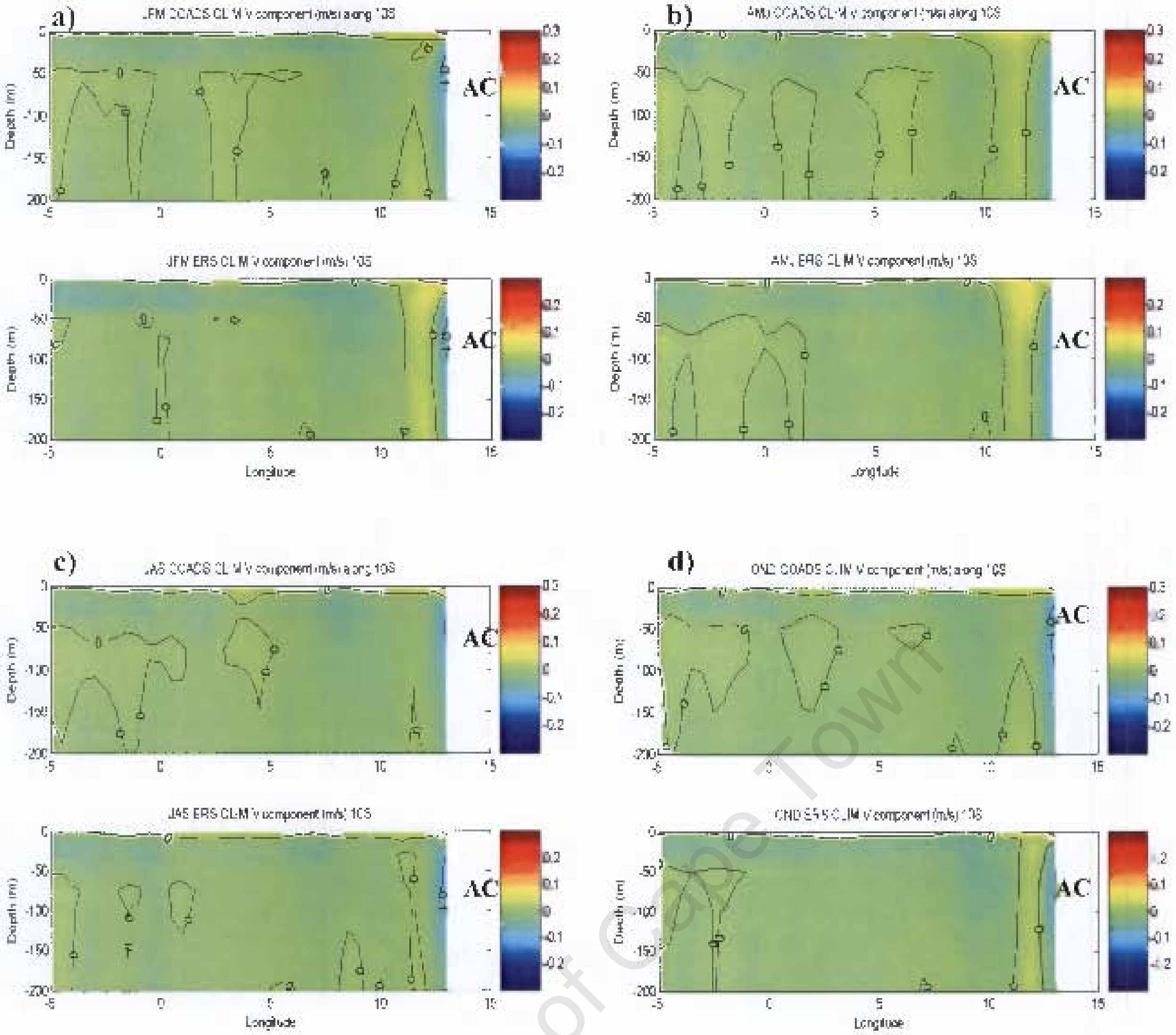

Figure 4.14: V component vertical section along 10S, seasonal mean, a) JFM, b) AMJ, c) JAS and d) OND. Top panel for COADS CLIM and bottom panel for ERS CLIM (contour interval 0.1ms^{-1}, positive values correspond to eastward flow). Shown are: Angola Current (AC).

Equatorial Undercurrent (EUC)

In a section along the equator the model results indicate the EUC, a strong eastward flow centred at 100m across the entire Atlantic (Peterson and Stramma, 1991) (**Figure 4.16**). The numerical outputs show a core velocity of 0.9ms^{-1} and 1ms^{-1} for COADS and ERS CLIM respectively, gradually weakening and shallowing as it approaches the eastern Atlantic basin.

The bifurcation of the EUC during JFM is around 9°E in the simulation outputs (**Figure 15(a)**). In the western Atlantic basin, in a section along 30°W, the core of the EUC ($0.9ms^{-1}$) is centred between 80-100m depth and 1°S and 1°N (see **Figure 4.17(a)**). The meridional section along 0°E and the EUC core ($0.8ms^{-1}$) is clearly centred between 60-80m and 1°S and 1°N (**Figure 4.18(a)**), i.e. weaker and shallower than in the section along 30°W.

In AMJ the EUC is shallower and weaker ($0.7ms^{-1}$) in the eastern Atlantic and its bifurcation occurs around 5°E (see **Figure 4.15(b)** and **Figure 4.16(b)**). The EUC weakening and shallowing is also evident in the section along 0°E (see **Figure 4.18(b)**). **Figure 4.16(b)** illustrates that in the section along 30°W the EUC position and strength, when compared to that of JFM, do not show significant differences.

In **Figure 4.15(c)** the bifurcation of the EUC in JAS is found further east than in AMJ. Furthermore, the sections along the equator reveal a deepening and strengthening of the EUC core in the eastern Atlantic during JAS compared to AMJ (see **Figure 4.16(c)**). This is also evident in the section along 0°E, where in both experiments the EUC core ($0.8ms^{-1}$) is stronger than that in AMJ (see **Figure 4.18(c)**).

During OND the simulation outputs reveal an intensification of the EUC in the eastern Atlantic. This is visible in the section along the equator (see **Figure 4.16(d)**) and at 100m depth, where the bifurcation of the EUC occurs near the African coast (see **Figure 4.15(d)**).

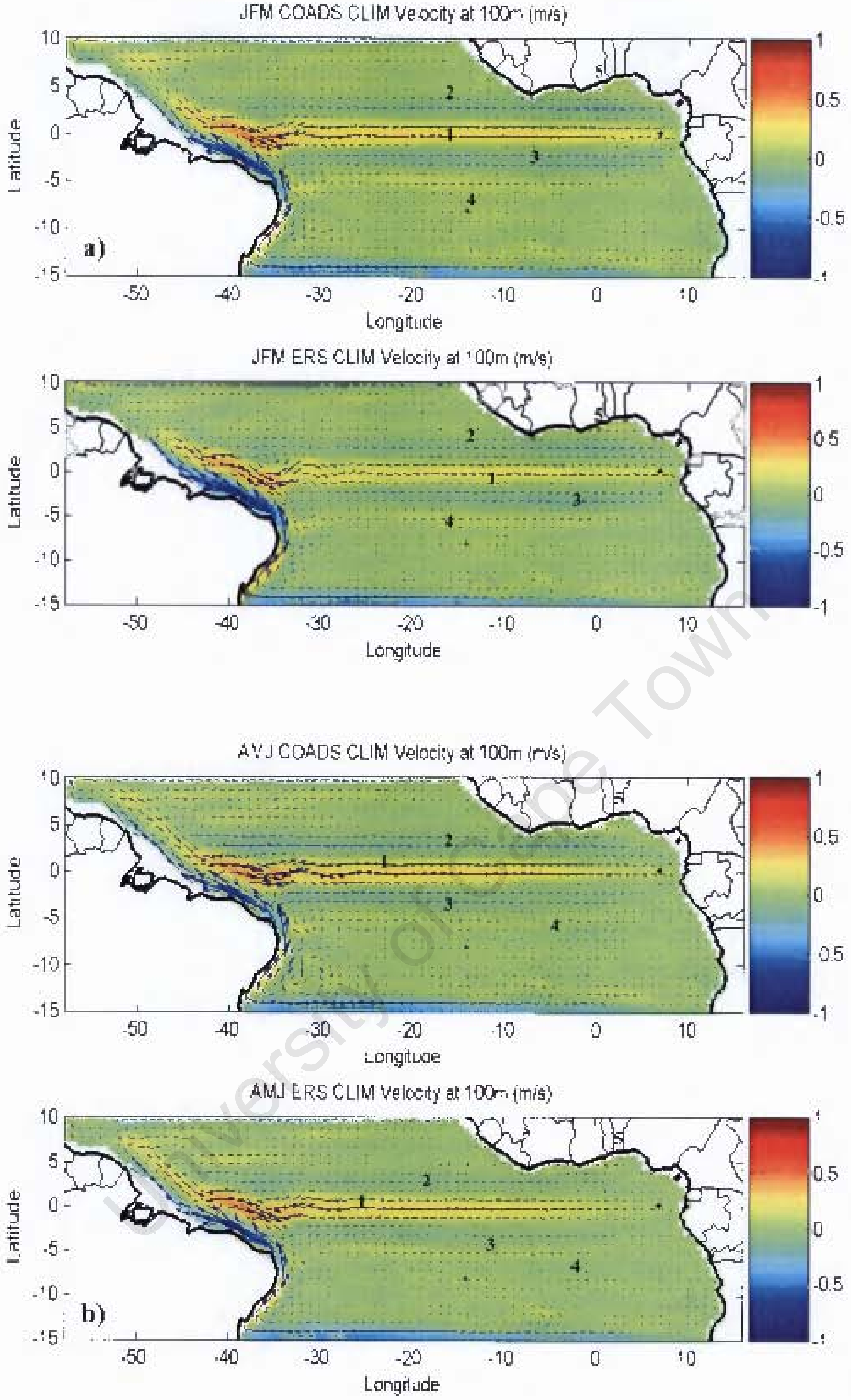

Figure 4.15: Velocity quiver at 100m with U component superimposed, seasonal mean, a) JFM and b) AMJ. Top panel for COADS CLIM and bottom panel for ERS CLIM (positive values correspond to eastward flow). Shown are: 1) Equatorial Undercurrent (EUC), 2) nSEC (north South Equatorial Current), 3) cSEC (central South Equatorial Current), 4) South Equatorial Undercurrent (SEUC) and 5) Gabon Current (GC).

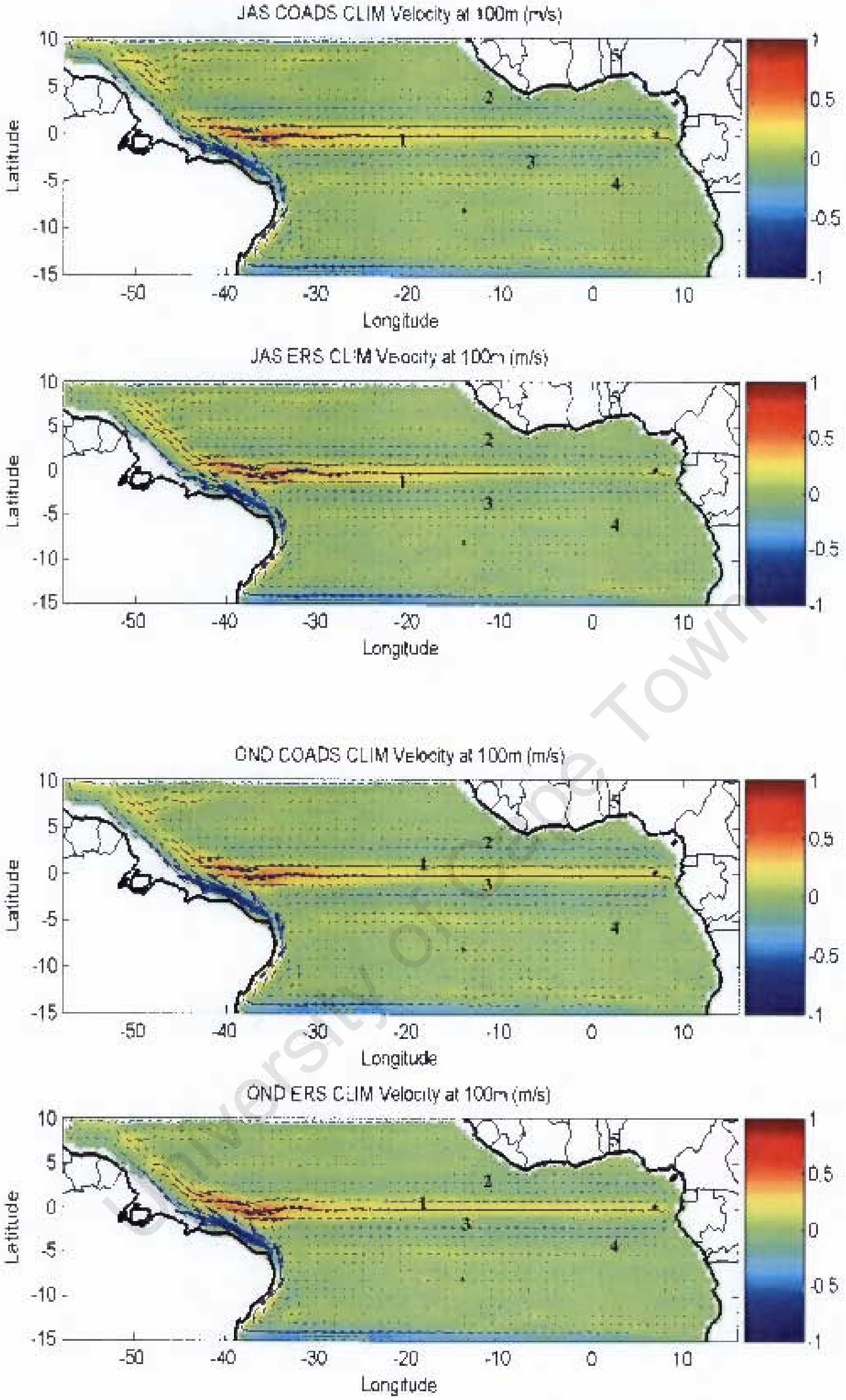

Figure 4.15: cont., c) JAS and d) OND. Top panel for COADS CLIM and bottom panel for ERS CLIM (positive values correspond to eastward flow). Shown are: 1) Equatorial Undercurrent (EUC), 2) nSEC (north South Equatorial Current), 3) cSEC (central South Equatorial Current), 4) South Equatorial Undercurrent (SEUC) and 5) Gabon Current (GC).

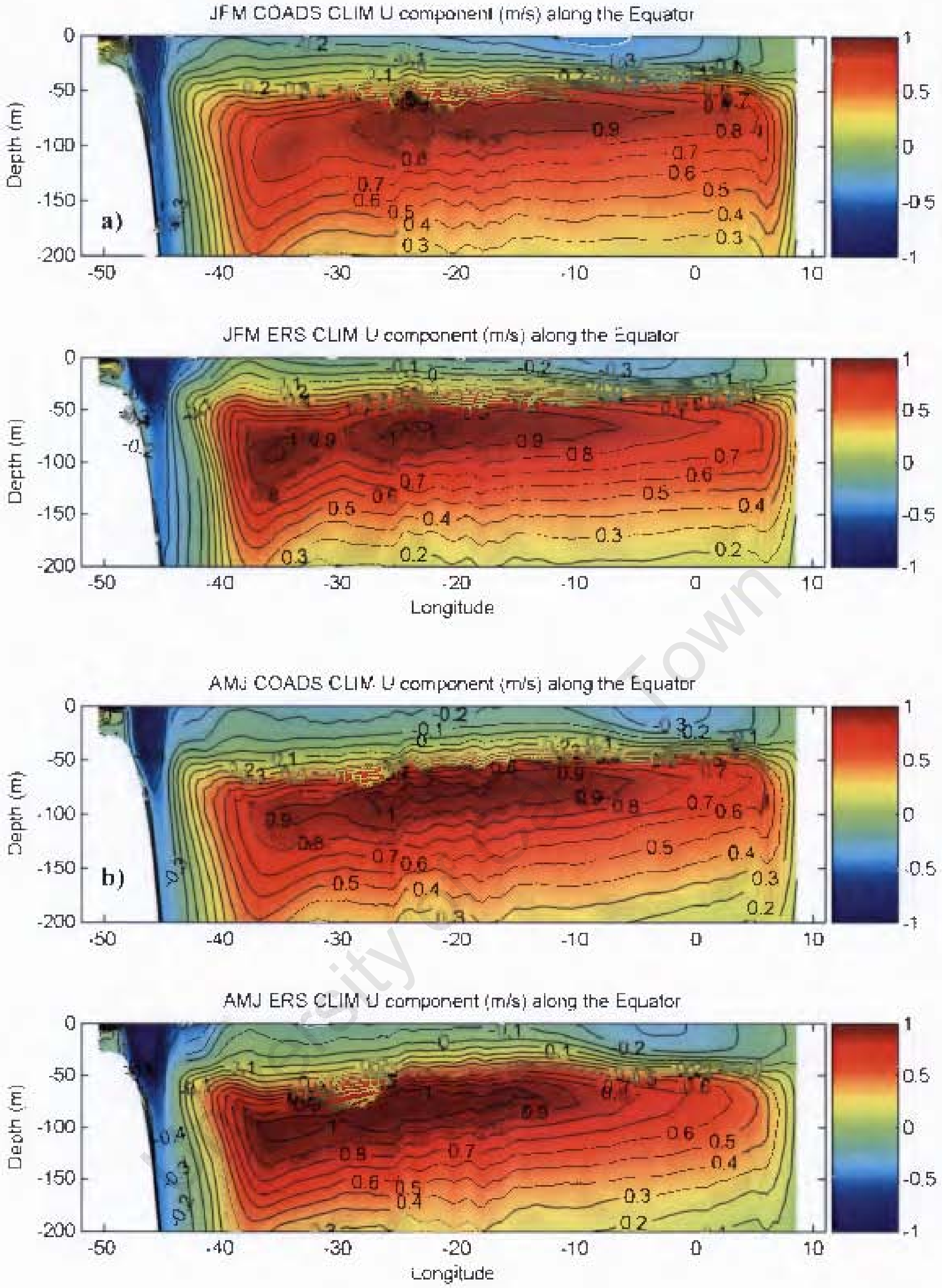

JFM COADS CLIM U component (m/s) along the Equator

JFM ERS CLIM U component (m/s) along the Equator

AMJ COADS CLIM U component (m/s) along the Equator

AMJ ERS CLIM U component (m/s) along the Equator

Figure 4.16: U component vertical section along the equator, seasonal mean, a) JFM and b) AMJ. Top panel for COADS CLIM and bottom panel for ERS CLIM (contour interval 0.1ms^{-1}, positive values correspond to eastward or northward flow).

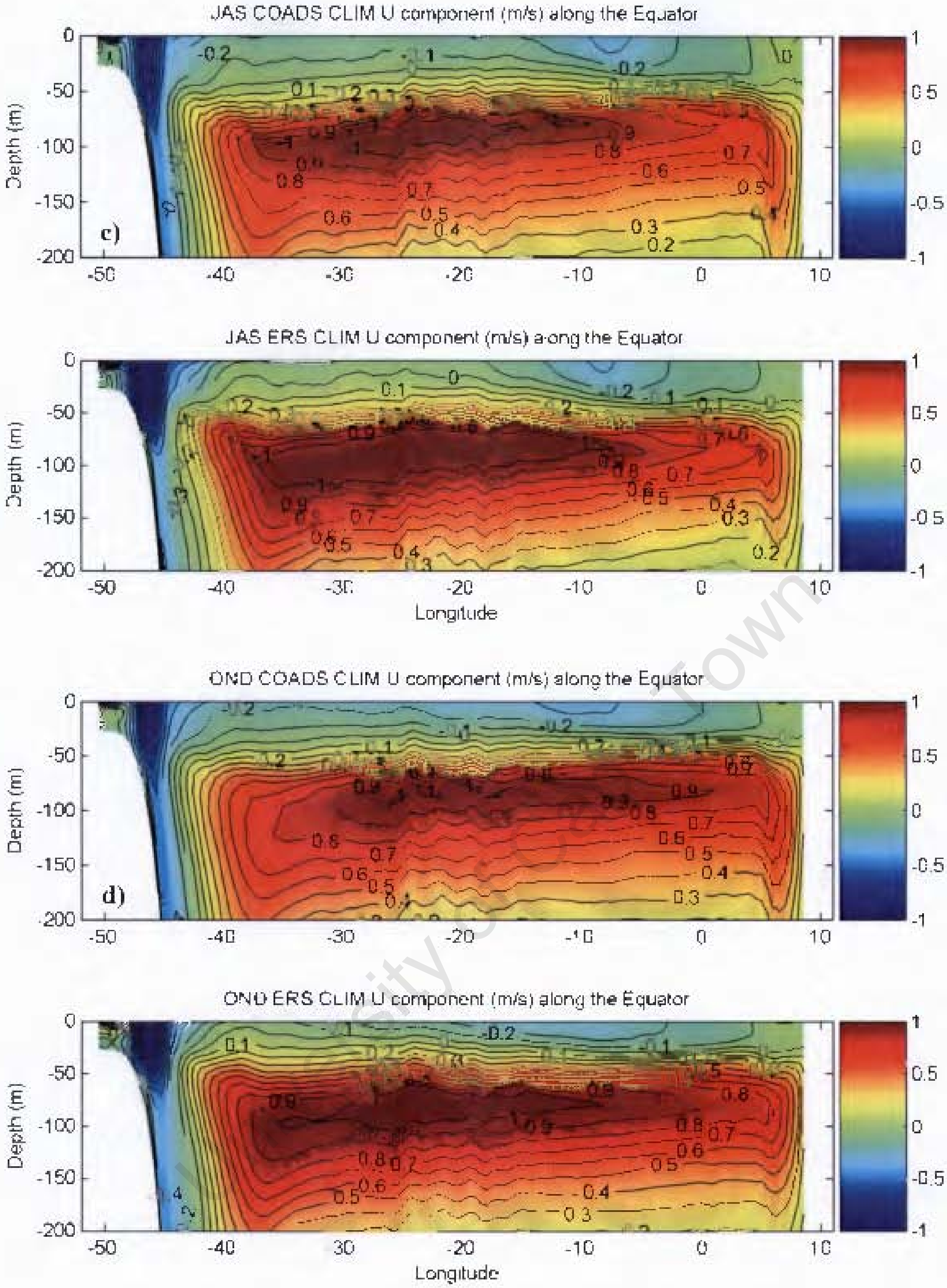

Figure 4.16: cont. c) JAS and d) OND. Top panel for COADS CLIM and bottom panel for ERS CLIM (contour interval 0.1ms^{-1}, positive values correspond to eastward or northward flow).

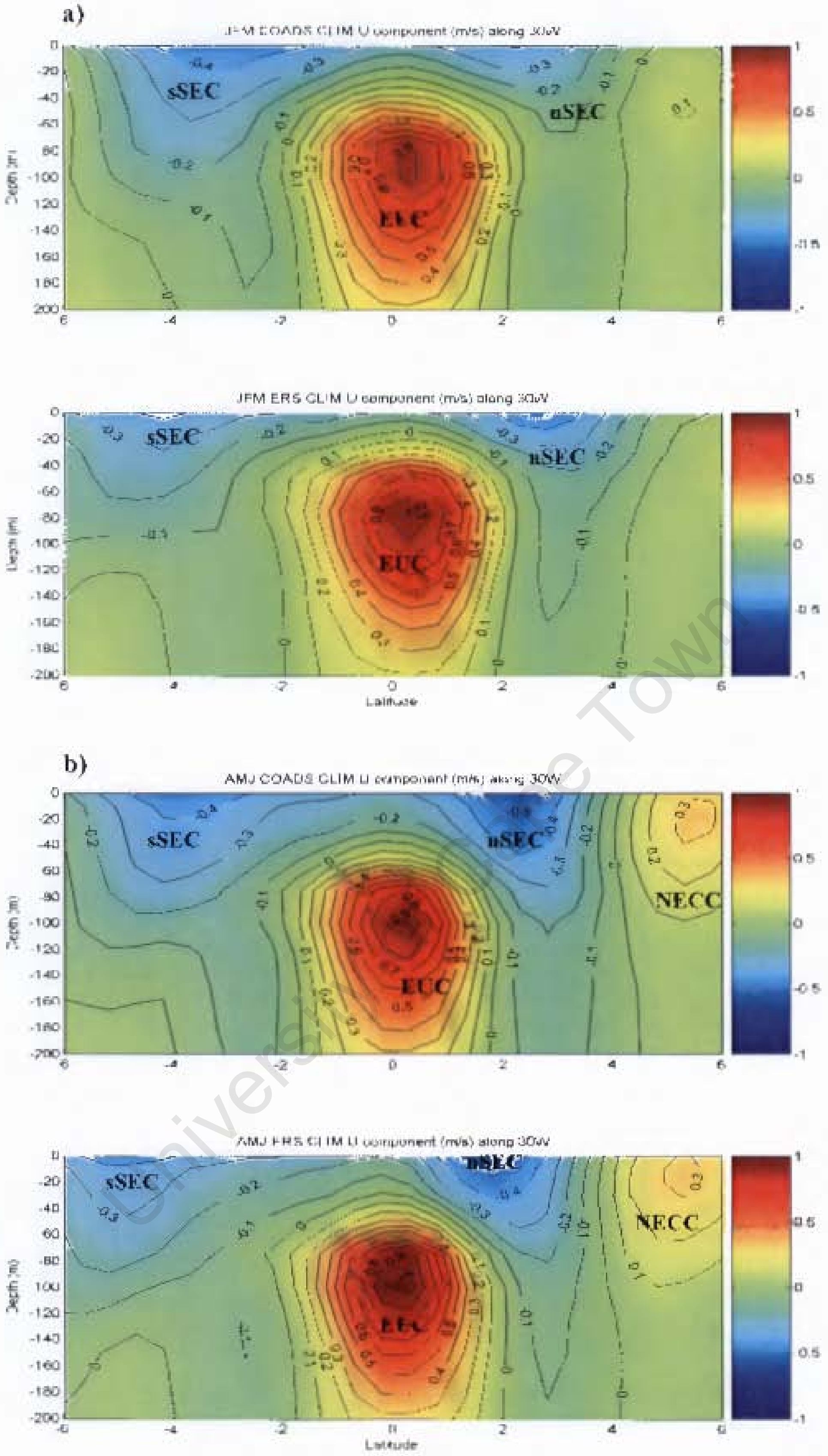

Figure 4.17: U component vertical section along 30°W, seasonal mean, a) JFM and b) AMJ. Top panel for COADS CLIM and bottom panel for ERS CLIM (contour interval 0.1ms^{-1}, positive values correspond to eastward flow). Shown are: Equatorial Undercurrent (EUC), North Equatorial Countercurrent (NECC), the South Equatorial Current (SEC) with the northern (nSEC) and southern branches (sSEC).

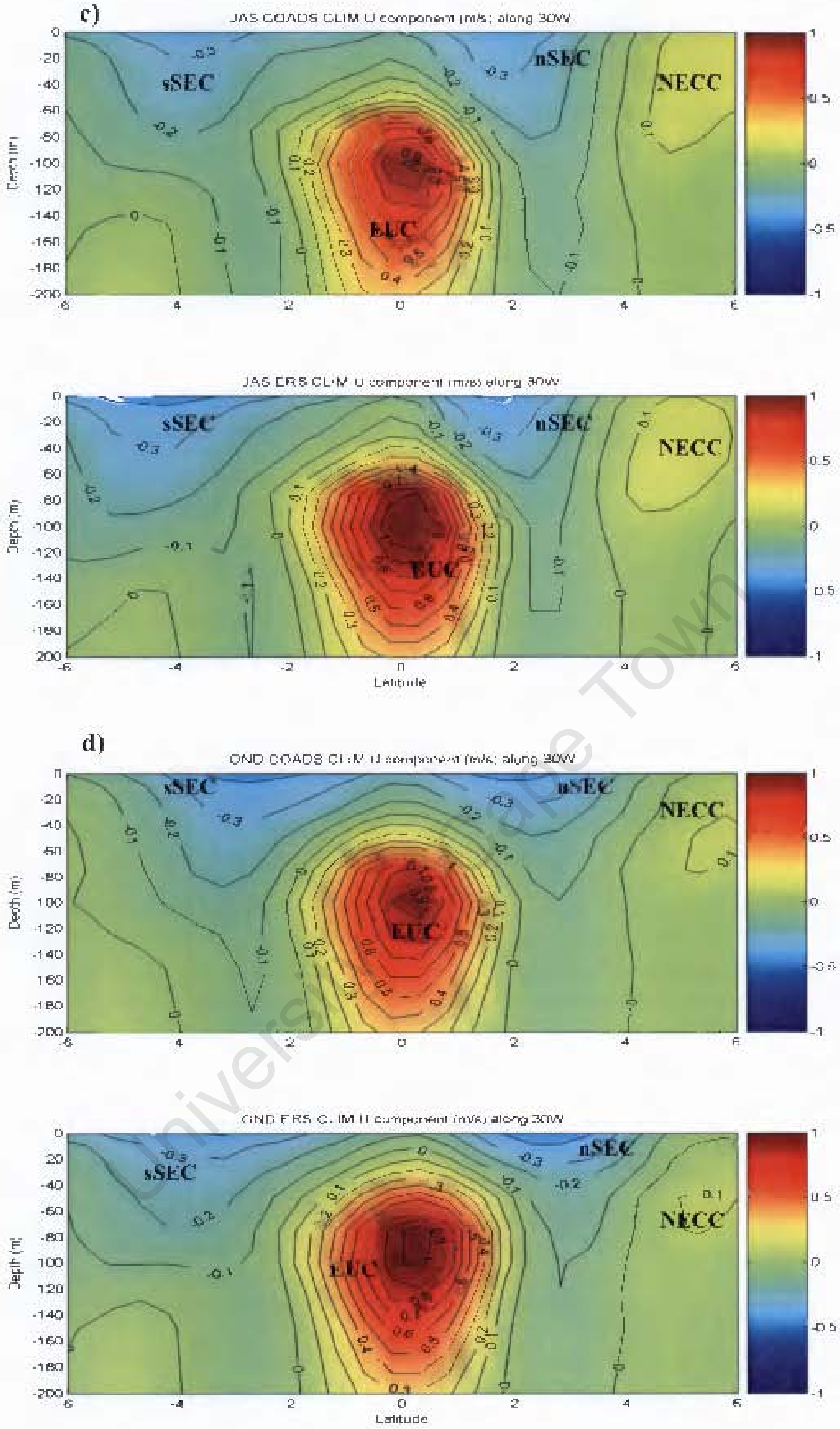

Figure 4.17: cont.. c) JAS and d) OND. Top panel for COADS CLIM and bottom panel for ERS CLIM (contour interval $0.1ms^{-1}$, positive values correspond to eastward flow). Shown are: Equatorial Undercurrent (EUC), North Equatorial Countercurrent (NECC), the South Equatorial Current (SEC) with the northern (nSEC) and southern branches (sSEC).

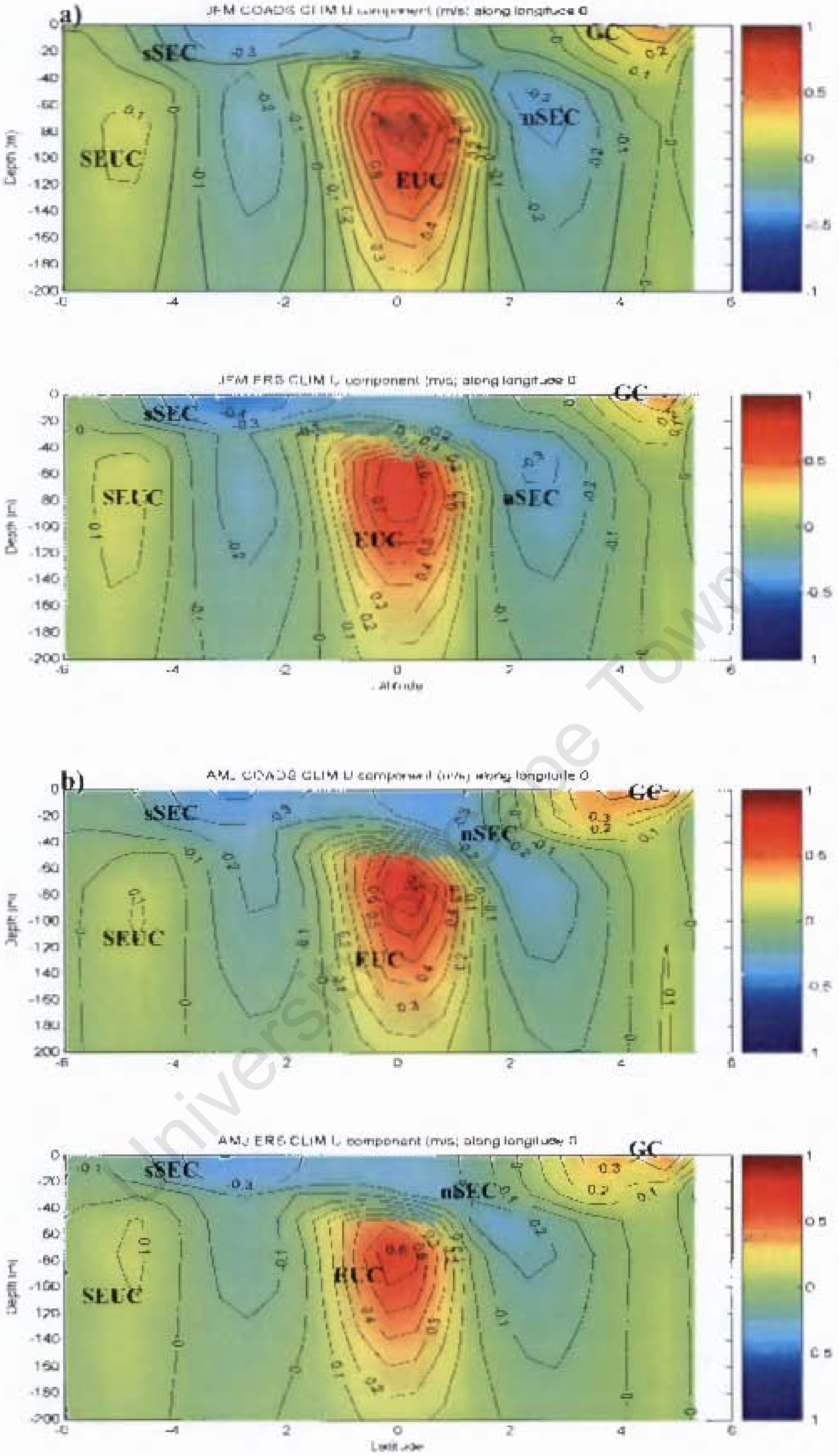

Figure 4.18: U component vertical section along 0E, seasonal mean, a) JFM and b) AMJ. Top panel for COADS CLIM and bottom panel for ERS CLIM (contour interval 0.1ms^{-1}, positive values correspond to eastward flow). Shown are: Equatorial Undercurrent (EUC), Gabon Current (GC), the South Equatorial Current (SEC) with the northern (nSEC) and southern branches (sSEC) and the South Equatorial Undercurrent (SEUC).

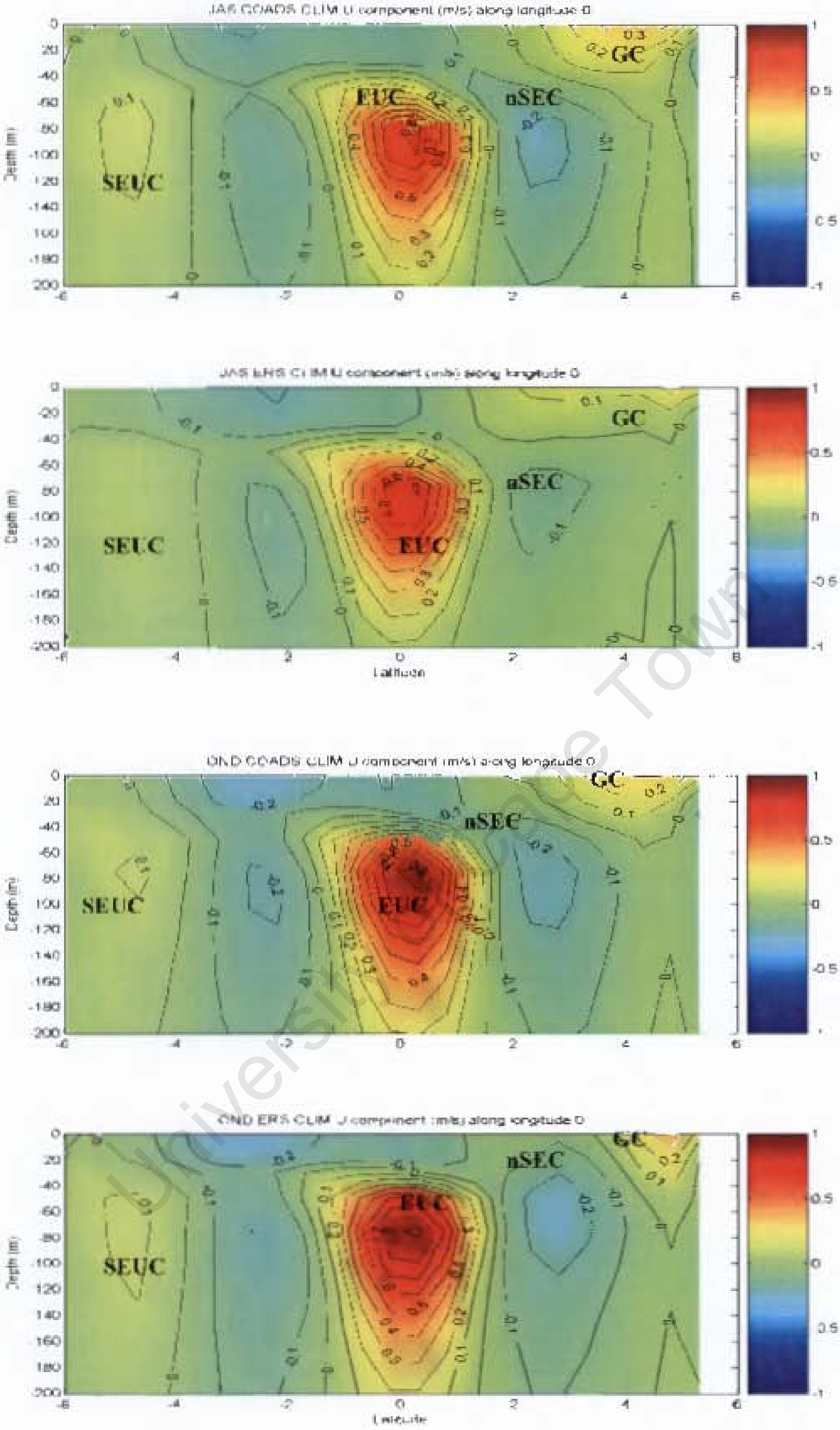

Figure 4.18: cont., seasonal mean, c) JAS and d) OND. Top panel for COADS CLIM and bottom panel for ERS CLIM (contour interval 0.1ms^{-1}, positive values correspond to eastward flow). Shown are: Equatorial Undercurrent (EUC), Gabon Current (GC), the South Equatorial Current (SEC) with the northern (nSEC) and southern branches (sSEC) and the South Equatorial Undercurrent (SEUC).

4.1.4 Discussion

The model approximately reproduces the SST annual cycle of the equatorial Atlantic. The main differences between the models and the observations concern the variability equatorial cold tongue. Both temporal and spatial variabilities are not in agreement with the observations and other studies. According to Carton and Zhou (1997) and WOA01 observations, one would expect the development of the cold tongue during the strong equatorial upwelling season (JAS). However, in the simulation results the cold tongue is clearly visible in AMJ (see **Figure 4.3(b)**). The cold tongue extends westward as far as 25°W, whereas the SST observations show a westward extension of this feature to 15°W (see **Figure 4.3(c)**). One possible explanation for the poor representation of the equatorial cold tongue could be the vertical mixing scheme parameterization implemented in ROMS. The K-profile planetary (KPP) parameterization boundary-layer scheme has a complex formulation and generally leads to non-linear results. The KPP uses the Richardson number to estimate the boundary layer depth (h) and the turbulent contribution to the vertical shear of a bulk Richardson number is also parameterized (Large *et al.*, 1994). In addition, the oceanic boundary layer can be forced from the interior through interior diffusivity and its vertical derivative at h. Along the equator this forcing can be significant since the Equatorial Undercurrent (EUC) can lead to shear instability near h (Large *et al.*, 1994). This would imply that the model mixed layer is constrained by the vertical mixing scheme and thus be very sensitive to changes on the surface forcing fields and on the EUC model behaviour (Dr. Pierrick Penven, personal communication).

Of the two simulations, ERS CLIM has the greatest spatial extension and coldest temperatures of the cold tongue, suggesting that the equatorial upwelling in this experiment is overestimated. Furthermore, the thermocline (20°C isotherm) is always deeper in the COADS CLIM results, suggesting that equatorial upwelling is stronger in ERS CLIM. These results are explained by the wind stress field over the equator being stronger in the ERS than in the COADS (see **Section 3.2** and **Figure 3.4(a)**). The wind stress differences and the vertical mixing scheme result in stronger upwelling in the ERS CLIM simulation during the boreal autumn and winter (AMJ and JAS).

The domain chosen for these experiments, 15°S, does not allow the model to study ABF dynamics. As a result the representation of the ABF is influenced by the boundary conditions. Colberg (2006) showed in his work that in order to simulate accurately the ABF dynamics the southward boundary of the model should at least extend until 30°S.

Carton and Zhou (1997) suggested three mechanisms controlling the SST seasonal cycle in the equatorial and tropical Atlantic (based on model sensitivity experiments on the tropical Atlantic). These mechanisms were coastal upwelling along the African coast in the austral winter, the zonal wind variability east of 28°W, which in turn drives equatorial upwelling and heat fluxes that have a greater impact north and south of 5°N and 5°S respectively. The disagreement between the model results and the observations could be explained by the dissimilarities in the three mechanisms. The different wind stress forcing between the two simulations (ERS wind stress being stronger than COADS wind stress, see **Section 3.2** and **Figure 3.4(a)**) and the vertical mixing scheme leads to errors in the SST cycle. It is important to note that the model is forced by heat fluxes and wind stress monthly means. The climatology fields do not fully represent the atmospheric and oceanic conditions of the Atlantic and are a potential source of errors in the SST cycle.

The seasonal cycle of the equatorial Atlantic currents is represented in both the COADS and ERS CLIM experiments results, but tends to be out of phase when compared with the observations. For example, the maximum deepening of the EUC and its bifurcation near the African coast occurs in JAS (Wacongne and Piton, 1992; Stramma and Peterson, 1999), whereas in the model the EUC maximum occurs during OND and JFM (see **Figure 4.15(d-a)** and **Figure 4.16(d-a)**). The seasonal cycle of the NECC reveals a season delay in relation to the observations and this is likely to be linked to an inaccurate representation of the NBC and its retroflection. The overestimation of the NBC impacts on its retroflection position, on the NECC seasonal cycle, and eventually on the salinity field of the Amazon River, which is strongly dependent on the advection factor.

Previous studies described the AC as a strong current ($0.4ms^{-1}$, Mohrholz *et al.* (2001)) from surface to 200m depth over the continental slope, but weaker during the austral winter (Shannon *et al.*, 1987). The model results clearly underestimate the AC and exhibit spatial but not velocity seasonal variability, which might influence the seasonal meridional migration of the ABF and its thermal gradients (see **Figure 4.14**). The AC also plays an important role in Benguela Niños and in low-oxygen events in the Benguela region. It is therefore important to obtain a good representation of the AC current, in order to predict these events.

The difficulties in representing coastal currents accurately are likely to be linked to two factors: the topography smoothing performed by the model when interpolating ETOPO2 to the model grid, and the horizontal grid resolution (0.5°) being insufficient to resolve narrow coastal currents. Therefore in order to improve the accuracy of the model, it is essential to carry out sensitivity tests to assess the optimal horizontal resolution and topography interpolation.

The seasonal and interannual variability of salinity in the Tropical Atlantic has been addressed in several studies (e.g., Levitus, 1986; Yoo and Carton, 1990; Dessier and Donguy, 1994; Masson and Delecluse, 2001; Delcroix *et al.*, 2005). Yoo and Carton (1990) argued that salinity variability impacts indirectly on the mixed layer depth. Delcroix *et al.* (2005) listed important issues related to SSS measurements, such as: understanding climate variability, assessing numerical model performance, determining the role of salinity on sea level and geostrophic currents, and modelling mixed-layer representation via data assimilation.

The SSS seasonal variability is captured by the model in both simulations but with some differences to the observations, particularly in the salinity spatial variability. Nevertheless, the model agrees with the observations in general, given that the model is not forced with surface flux climatologies and river runoffs. In fact, the fresh water plumes are forced by the surface restoring term in the salinity field. This implies that the there is a relaxation towards salinity climatology rather than an explicit simulation of the fresh river plumes by the model. Masson and Delecluse (2001) argued that when their model (TOTEM) was forced with realistic river runoff (the Amazon and

Congo River runoffs) the results showed better agreement with the observations. However, in the present study the differences in the salinity spatial variability are likely to be linked with the currents produced by the model. For example, during JFM the Amazon River freshwater plume is found further north-west than in the observations. Analysing the surface currents during the same time period (see **Figure 4.12(a)**) reveals that the model overestimates the North Brazilian current (NBC) and Guyana Current (GC), which results in the freshwater plume being advected north-westward earlier than in the observations. This mechanism would be supported by several studies that refer to advection as being the main process driving salinity spatial variability (Levitus 1986; Masson and Delecluse, 2001; Dessier and Donguy, 1994; Delcroix *et al.*, 2005). In addition, in order to obtain better results for salinity fields, it would be important to use river runoff forcing in ROMS simulations.

4.2 Sensitivity analyses: Benguela Niños/Niñas events

This section is dedicated to the description and discussion of the results obtained with the wind sensitivity experiments (hereafter referred to as ERS WEAK and ERS STRONG) described in **Section 3.2**. The aim of these sensitivity experiments was to assess the model response to different extreme wind forcing and, in the case of the ERS WEAK experiment, to investigate the origin and propagation of Benguela Niños. As mentioned in **Section 2.6**, according to several studies have suggested that Benguela Niño events are triggered by a relaxation of the easterlies off the Brazilian coast (Shannon *et al.*, 1986; Florenchie *et al.* 2003; Florenchie *et al.* 2004). By artificially reducing the wind field off the Brazilian coast, the model is expected to approximately reproduce the oceanic conditions during a Benguela Niño event. Such oceanic conditions would include:

- subsurface temperature anomalies along the equator;
- their eastward propagation along the thermocline (Florenchie *et al.* 2004);
- sea surface temperature anomalies in the ABF region roughly two months after the relaxation of the easterly winds (Florenchie *et al.* 2004);
- enhanced poleward flow along the Angolan coast during the event (Gammelsrød *et al.*, 1998).

It is important to keep in mind that only the wind stress field is artificially reduced in an area off the coast of Brazil. Other surface flux climatologies forcing the model are applied without modification. This implies that the oceanic and atmospheric conditions that are observed prior to and during a Benguela Niño event are not fully represented in this experiment. These conditions include the southward shift of the

ICTZ, enhanced equatorial convection, and enhanced rainfall over north-east Brazil and south-west Africa (Horel *et al.*, 1986).

In order to compare the results obtained by ERS WEAK and ERS STRONG with the control simulation ERS CLIM, the temperature, salinity and velocity monthly anomalies have been computed. The anomalies have been calculated by subtracting the ERS CLIM simulation from the sensitivity experiment (anomaly = ERS WEAK or STRONG - ERS CLIM), and have been analysed at the surface, along meridional sections at 30°W, 0°E and along zonal sections at the equator and at 10°S.

4.2.1 Temperature

In the third simulation (ERS WEAK), an artificial wind stress relaxation was induced during January, February and March. The wind stress was reduced by 50% in January and March and by 75% in February. Artificial wind anomalies were applied over an area extending from the Brazil coast to 8°W and from 6°N to 6°S (see **Section 3.2** and **Figure 3.4(b)**).

In **Figure 4.19(a-f)** comparisons of the temperature vertical section along the equator between ERS CLIM, ERS WEAK and ERS STRONG are shown. As a result of the wind relaxation, the thermocline is shallower in the western Atlantic and deeper in the eastern Atlantic, i.e. a thermocline tilt is evident in the model results. During March\April the thermocline structure is near horizontal due to adiabatic adjustment of the thermocline (**Figure 4.19(c-d)**). In contrast, when the model was forced with an artificial strengthening (fourth simulation), the results reveal a deepening of the thermocline in the western Atlantic and a shallowing in the eastern Atlantic, increasing the steep slope of the equatorial Atlantic thermocline (**Figure 4.19(c-d)**).

A positive subsurface temperature anomaly associated with the thermocline perturbation is evident (**Figure 4.19**). The numerical results suggest also an eastward propagation of the anomaly along the equatorial thermocline interface (**Figure 4.20(a-l)**). In addition, as the temperature anomalies reach the African coast, they turn southward and northward as far as the ABF and the Gulf of Guinea regions, where the model results show a westward propagation (probably as Rossby waves) of the anomalies (see **Figure 4.21** and **Figure 4.22**).

The simulation results also exhibit a fast response to wind anomalies, i.e. in January (with a 50% relaxation) the model produces a subsurface positive temperature anomaly (1°C) centred at 30°W and ranging from 60-100m in depth. In February (75% relaxation), this positive warm anomaly is well developed and is clearly seen along the entire equatorial Atlantic. It follows the thermocline depth to the African coast (**Figure 4.20(b)**). During March the warm anomaly core reaches its maximum value (3°C) and extends from 15°W to as far as 5°E (**Figure 4.20(c)**). In April the anomaly mainly affects the eastern Atlantic coast. From April to May the warm anomaly is replaced by a cold anomaly (**Figure 4.20(c-d)**) and this constitutes further evidence of the model's fast response to different wind forcing. The artificial relaxation of the wind stress and the wind stress strengthening (when the wind forcing returns to the original ERS wind climatology) triggers a chain of intercalated cold and warm events (anomalies replicated with gradually smaller strengths) during the remainder of the year (**Figure 4.20(f-h)**).

The cold anomalies produced when the model is forced with stronger winds have a different behaviour to the warm anomalies described above. The cold anomalies seem to be slightly weaker than their counterparts, they have a smaller impact on the ABF region, and a reduced life span (see **Figure 4.20(a-l)** and **Figure 4.21(a-l)**). As observed in the ERS WEAK simulation results, when the wind field returns to its climatological values, the model also shows a fast response to the new forcing. In this case the wind stress field transition from the artificial strengthening to the climatology wind stress field is equivalent to a wind stress reduction. As seen in **Figure 3.4(b)**, in March the artificial wind stress is 50% stronger than the climatology and in April it follows the usual seasonal wind relaxation (when forcing is back to normal climatology values). The model response is a clear, strong positive anomaly originating over the South American continental shelf and propagating along the equator as far as the African coast in just one month (see **Figure 4.20(d-e)**).

The temperature anomaly horizontal fields have been averaged from the surface to 100m depth and are shown in **Figure 4.20**. The generation of the warm and cold anomalies in the western Atlantic, their propagation along the equator, as well as their poleward propagation along the African coast as far as the ABF region, are clearly visible from February to June. The contrast between warm and cold anomalies is also evident, particularly their impact on the ABF region with the warm anomalies showing a greater impact. The ERS WEAK experiment results also reveal bands of negative anomalies north and south (around 5°S and 5°N) of the positive anomalies along the equator, which propagate north-westward from May to July (**Figure 4.21(e-g)**). The numerical results suggest that these bands of negative anomalies have a subsurface origin, since their surface signature is weak (0.5°C, **Figure 4.22**), whereas the temperature average between the surface and a depth of 100m shows a stronger negative anomaly (2°C, **Figure 4.21**). The same feature is evident (but with the opposite sign) in the results obtained by ERS STRONG, except that the warm anomaly is mainly evident north (5°N) of the cold anomaly.

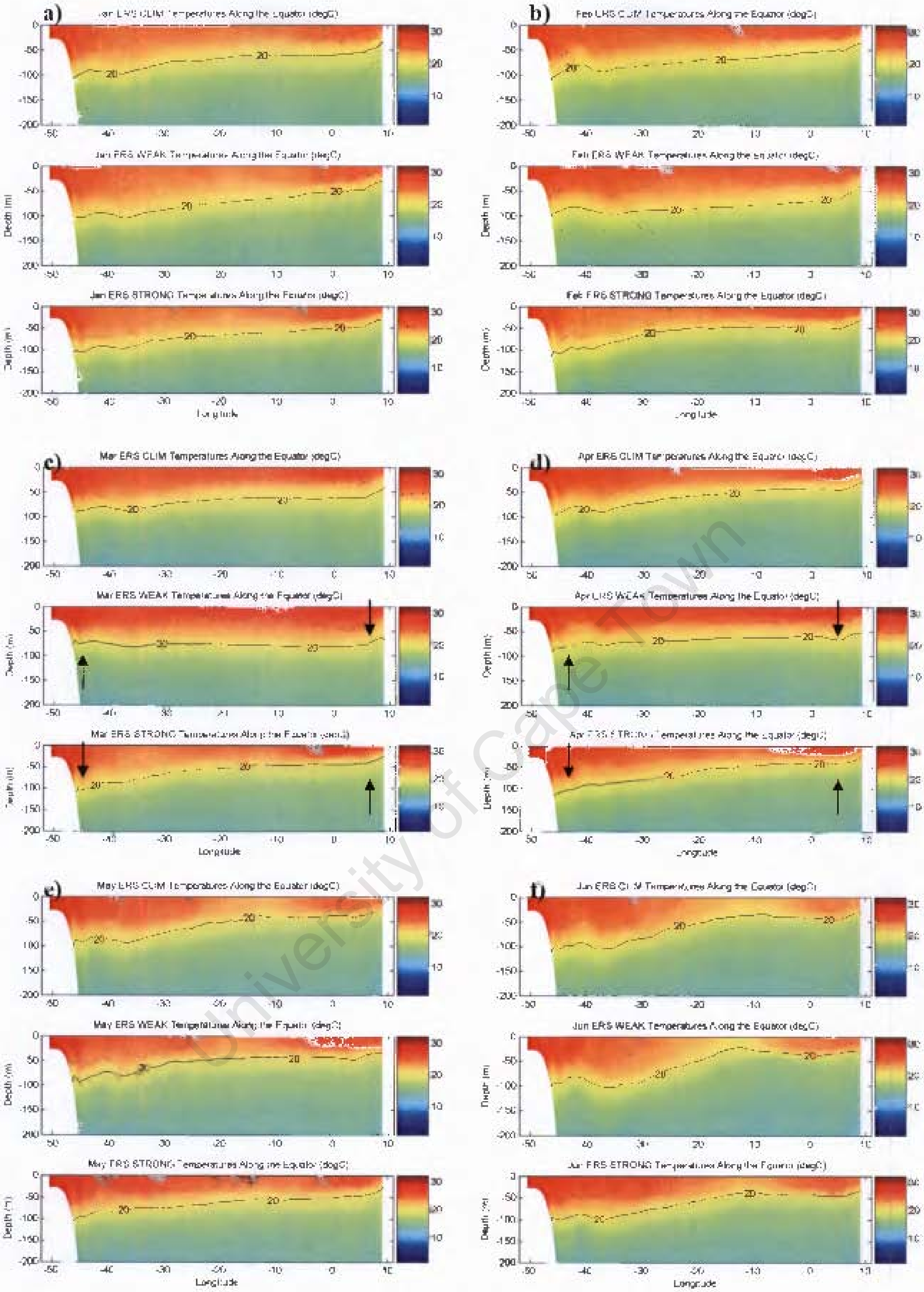

Figure 4.19: Vertical section of the temperature along the equator, monthly mean a) Jan., b) Feb., c) March, d) April, e) May and f) June. Top panel for ERS CLIM, middle panel for ERS WEAK and bottom panel for ERS STRONG. Black arrows highlight the thermocline deepening or shallowing (contour 20°C isotherm).

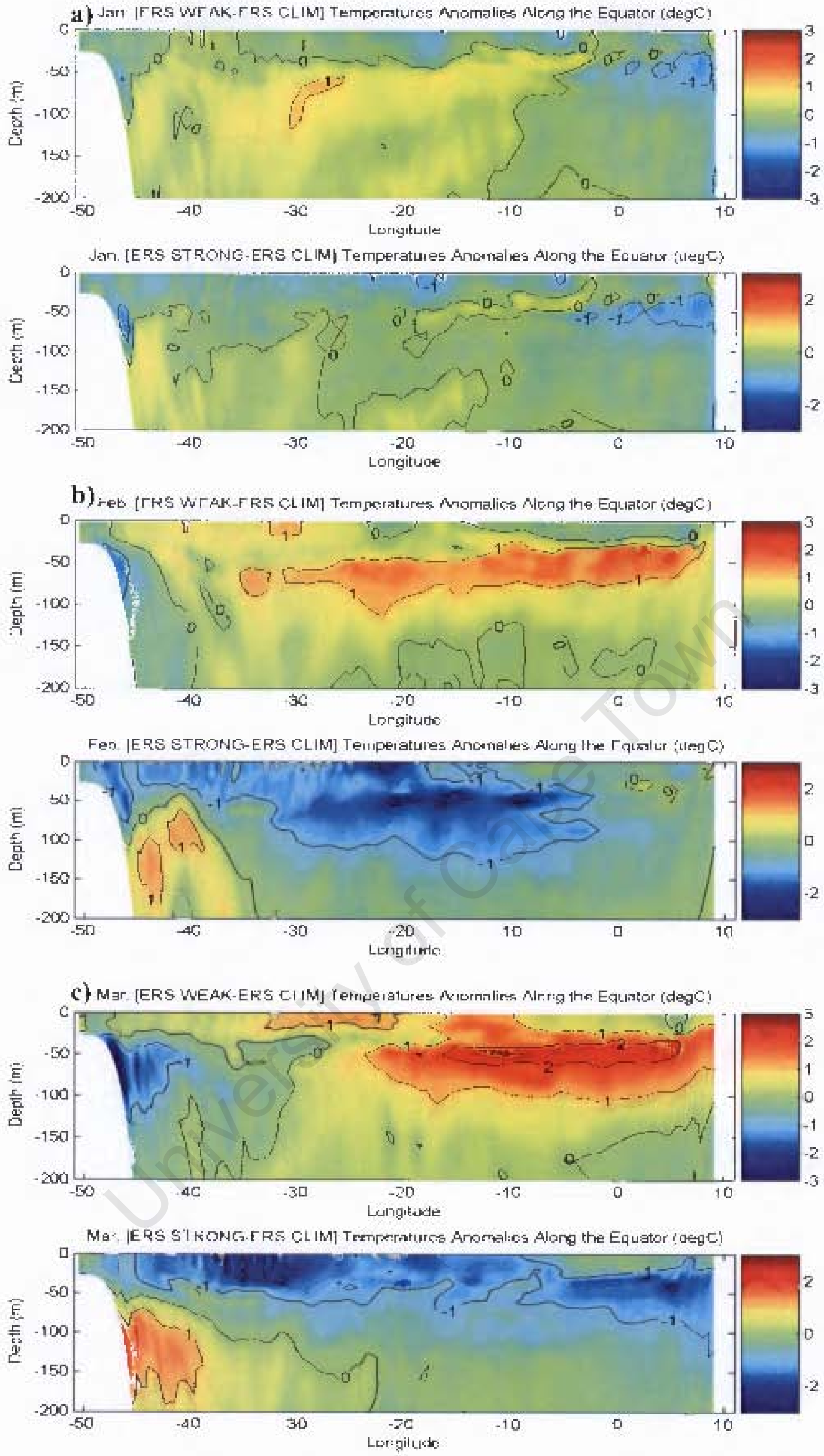

Figure 4.20: Vertical section of the temperature along the equator, monthly anomaly a) January, b) February and c) March. Top panel for ERS WEAK and bottom panel for ERS STRONG. (contour interval 1°C).

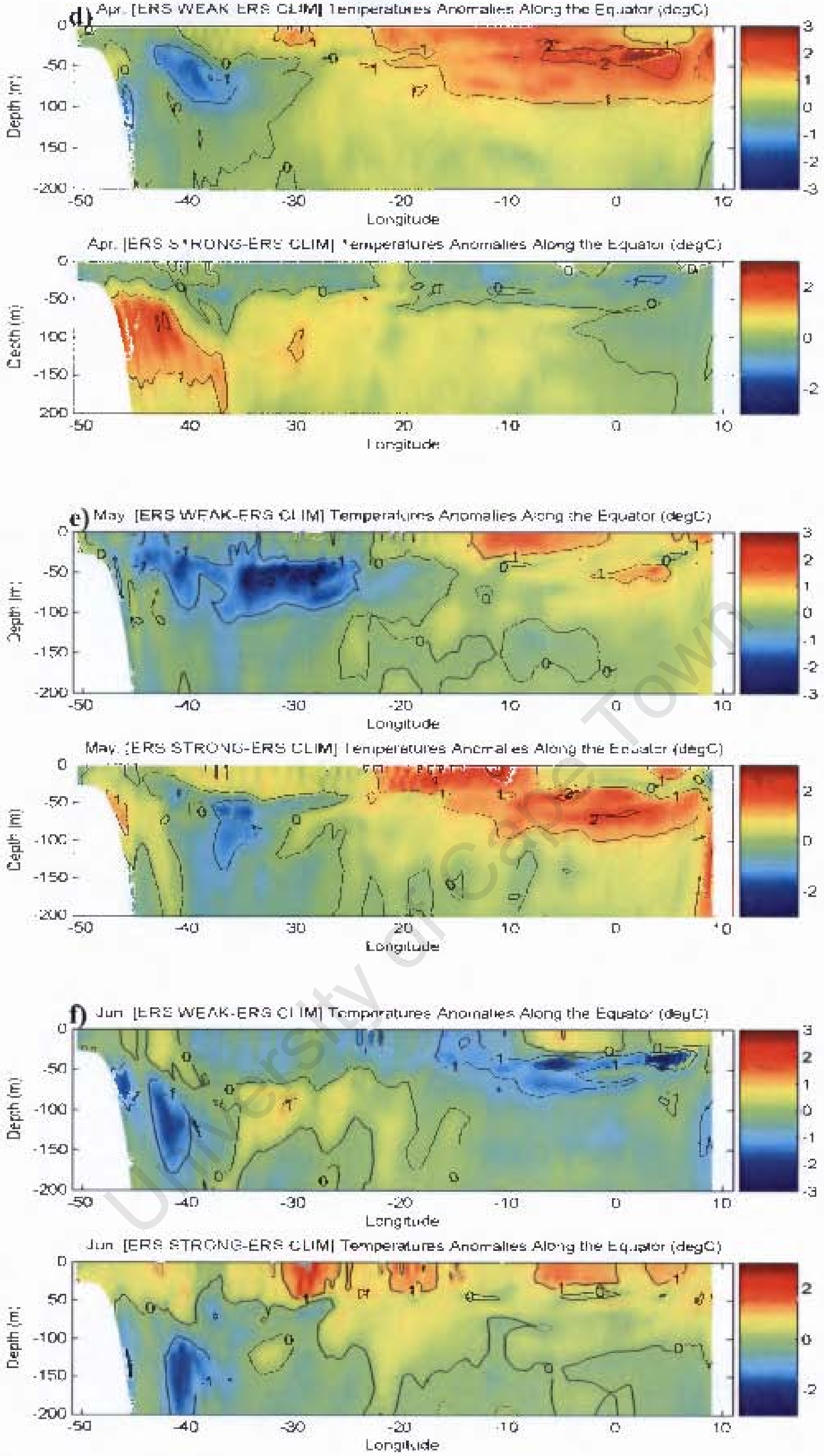

Figure 4.20: cont. d) April, e) May and f) June. Top panel for ERS WEAK and bottom panel for ERS STRONG. (contour interval 1°C).

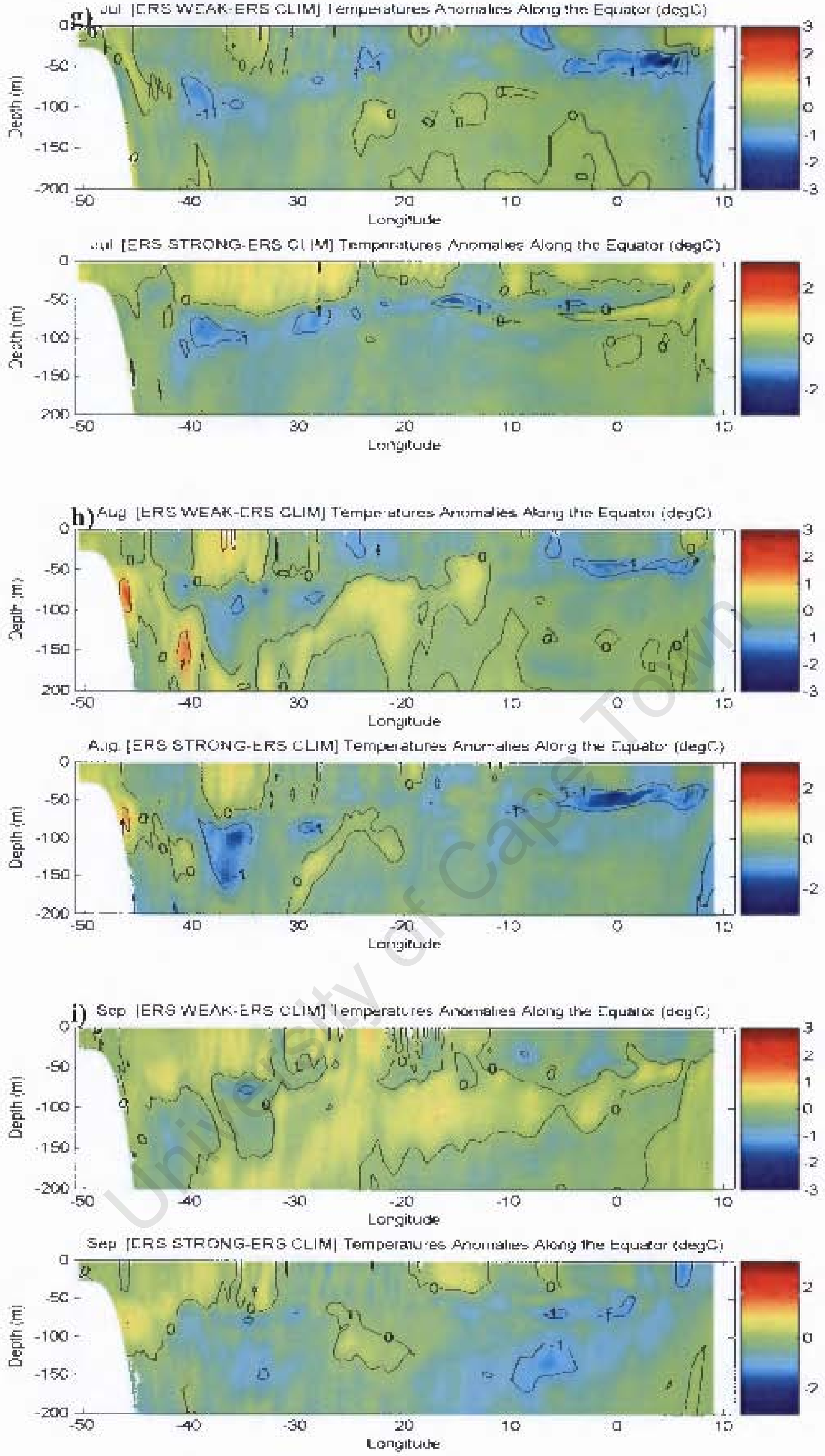

Figure 4.20: cont. g) July, h) August and i) September. Top panel for ERS WEAK and bottom panel for ERS STRONG. (contour interval 1°C).

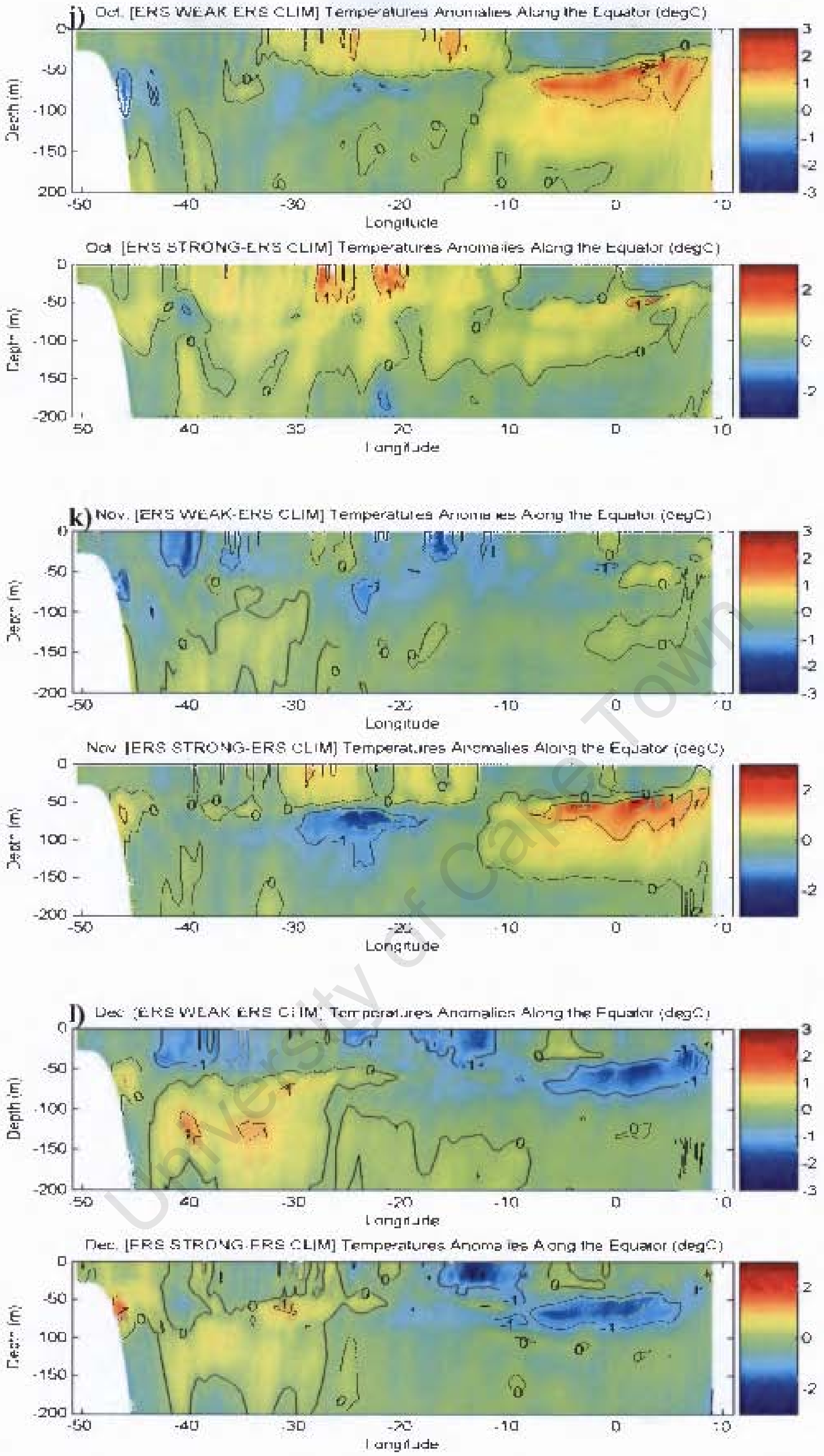

Figure 4.20: cont. j) October, k) November and l) December. Top panel for ERS WEAK and bottom panel for ERS STRONG. (contour interval 1°C).

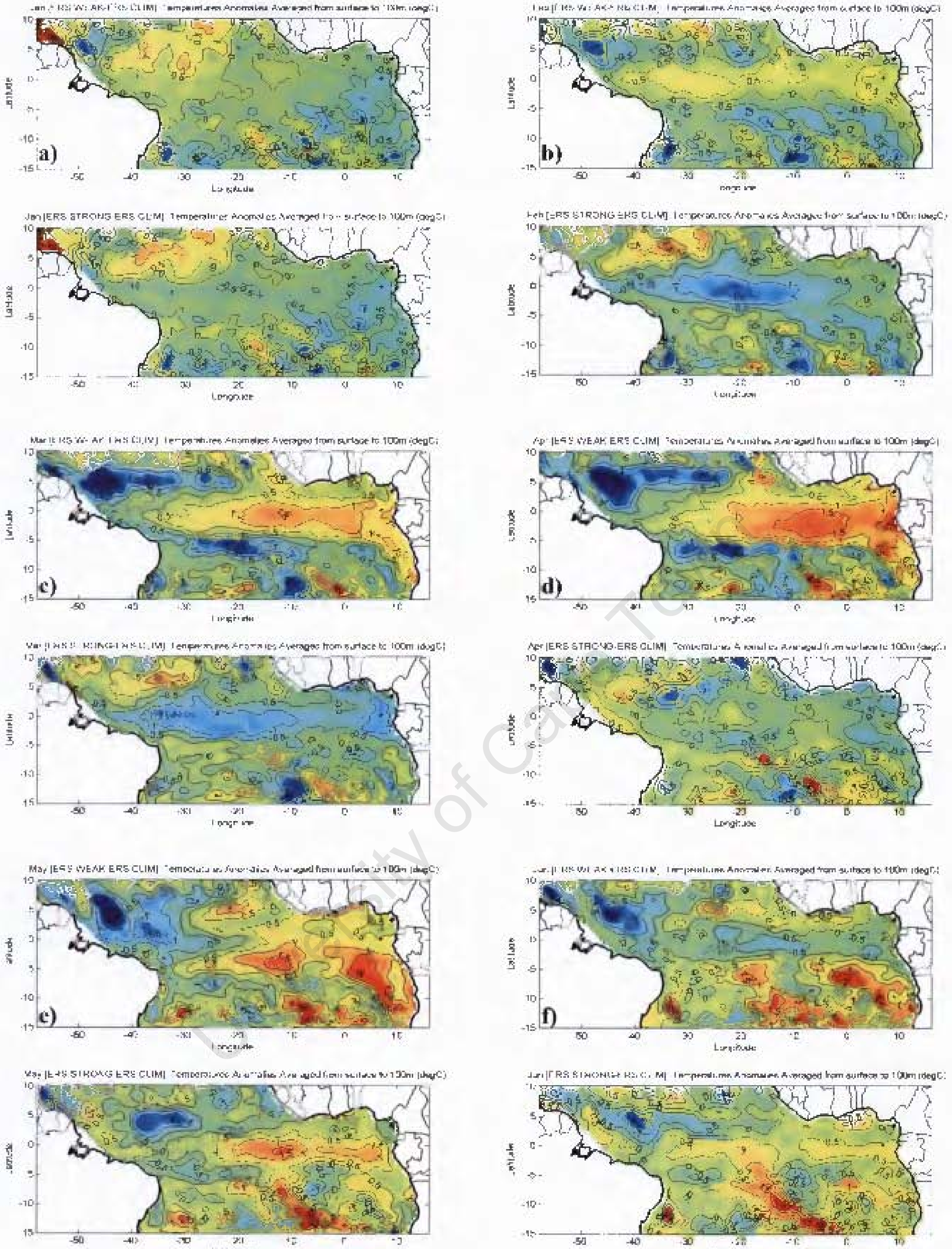

Figure 4.21: Temperature monthly mean anomaly averaged from surface to 100m depth. a) Jan., b) Feb., c) March, d) April, e) May and f) June. Top panel for ERS WEAK and bottom panel for ERS STRONG (contour interval 0.5°C).

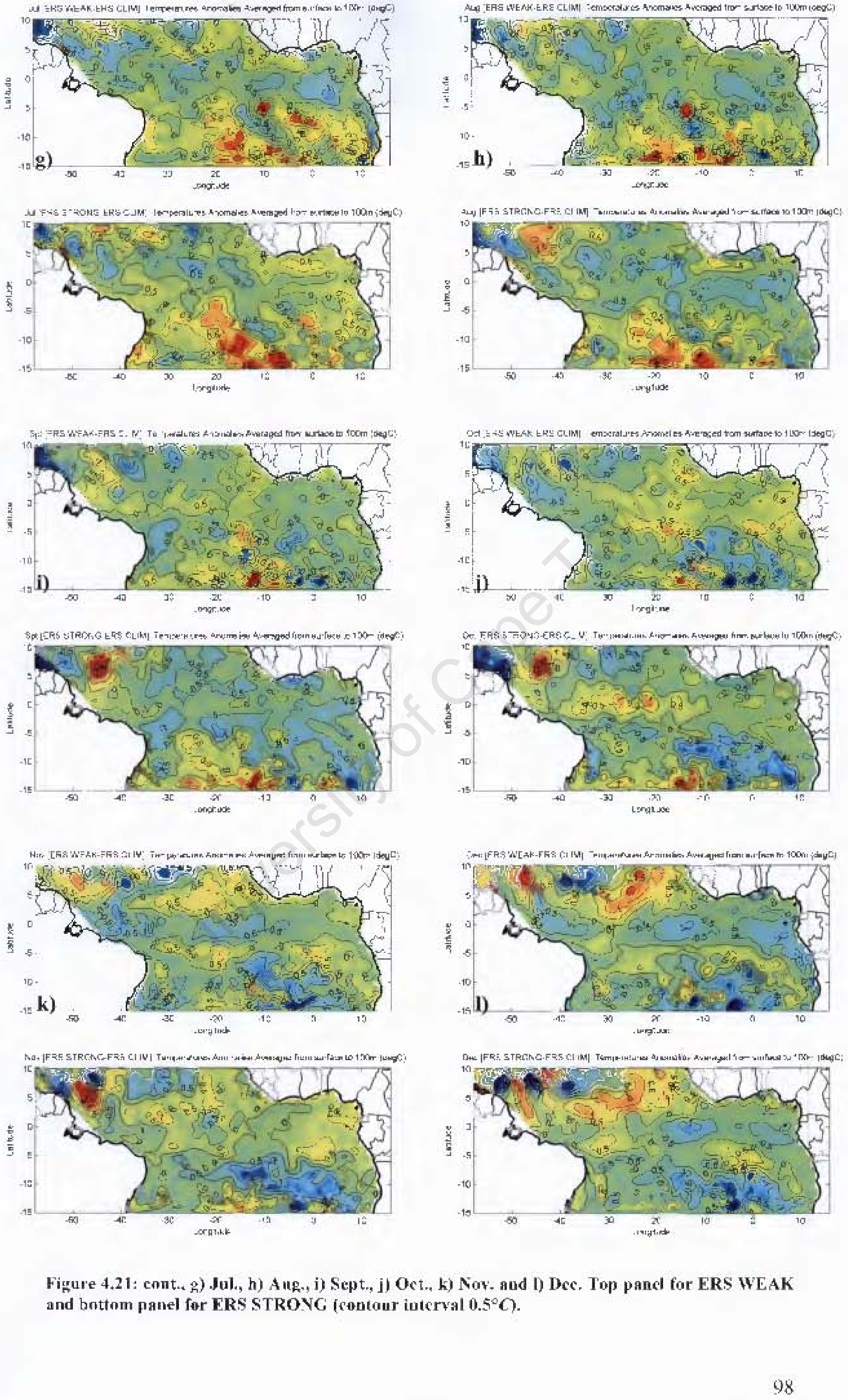

Figure 4.21: cont., g) Jul., h) Aug., i) Sept., j) Oct., k) Nov. and l) Dec. Top panel for ERS WEAK and bottom panel for ERS STRONG (contour interval 0.5°*C*).

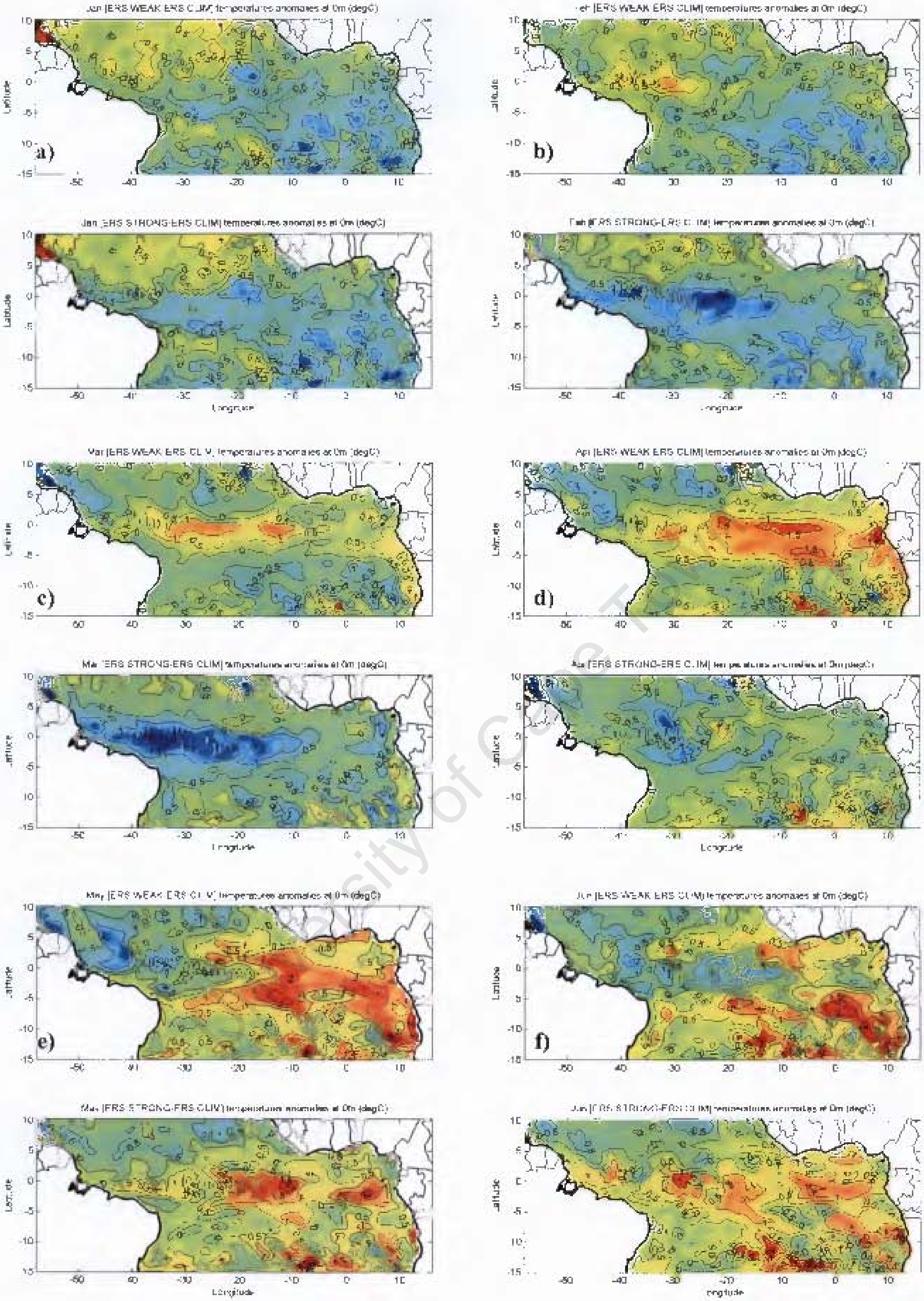

Figure 4.22: Sea surface temperature monthly mean anomaly, a) Jan., b) Feb., c) March, d) April, e) May and f) June. Top panel for ERS WEAK and bottom panel for ERS STRONG (contour interval 0.5°C).

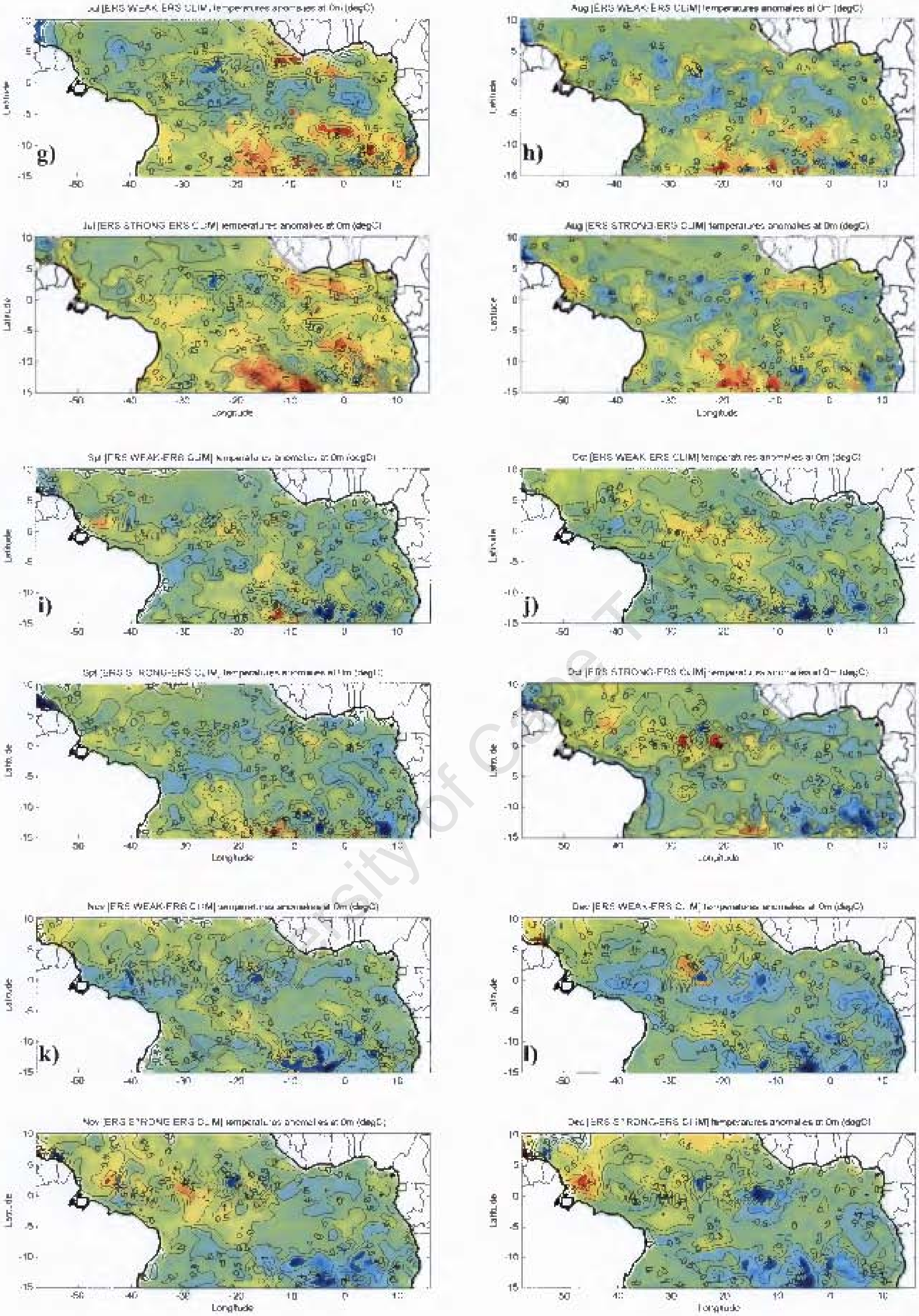

Figure 4.22: cont., g) Jul., h) Aug., i) Sept., j) Oct., k) Nov. and l) Dec. Top panel for ERS WEAK and bottom panel for ERS STRONG (contour interval 0.5°*C*).

4.2.2 Salinity

The comparison between the two sensitivity experiments (ERS WEAK and STRONG) shows that when the model is forced with stronger winds (ERS STRONG) the impact on the salinity field is higher than when the model is forced with weaker winds (see **Figure 4.23**).

ERS STRONG

The results obtained by ERS STRONG reveal a strong contrast in the sea surface salinity (SSS) anomalies between the north-western and eastern Atlantic. In the north-western Atlantic the strong SSS positive anomalies suggest the presence of more saline water in the region and this is likely to be linked to the strengthening of the cSEC/nSEC which will advect saline waters to the Amazon River mouth region (see **Figure 4.23(a-f)**). In July and August the appearance of negative salinity anomalies is linked to reduced advection of saline waters by the cSEC/nSEC (see **Figure 4.23(g-h)**). From September to the end of year the negative salinity anomalies linked to the stronger presence of the Amazon freshwater plume extend north-eastward (see **Figure 4.23(i-l))**). In the eastern Atlantic, however, the salinity anomalies are negative from February to June (see **Figure 4.23(a-f)**) and reach their maximum extension, from the equator to 10°S, during April/May. From September to October/November a strong positive anomaly is evident from the Gulf of Guinea to as far south as the Congo River region, suggesting the presence of more saline water advected by the GC (**Figure 4.23(i-k)**). In November/December the region seems to be under the influence of the fresh water originating in Biafra Bay, resulting in negative anomalies in the Gulf of Guinea (**Figure 4.23(k-l)**).

ERS WEAK

The results from the simulation ERS WEAK reveal salinity anomalies in the region of the Amazon River mouth but these anomalies have a smaller spatial extension compared to those from ERS STRONG. During January and February a positive anomaly is evident but spatially constrained to the Amazon River mouth (**Figure 4.23(a-b)**). In March this positive anomaly is advected north-westward and is replaced by a strong negative anomaly at the river mouth (**Figure 4.23(c)**). From April to July the numerical outputs show weak positive anomalies near the river mouth area and to the north-west of the river mouth (**Figure 4.23(d-g)**). In August a pronounced surface salinity negative anomaly is evident just north of the Amazon River mouth, suggesting a significant influence of the Amazon River freshwater plume (**Figure 4.23(h)**). During the remainder of the year, the salinity anomalies reach their minimum values and spatial extension (**Figure 4.23(i-l)**).

In the eastern Atlantic the ERS WEAK results have weak anomaly values (0.5 *psu*) throughout the year. The salinity anomalies in this region exhibit shifts between positive and negative anomalies, i.e. in January/February they are mainly positive, from March to June they become negative, and then in the austral spring the negative anomalies are replaced by positive anomalies originating from the Biafra Bay region.

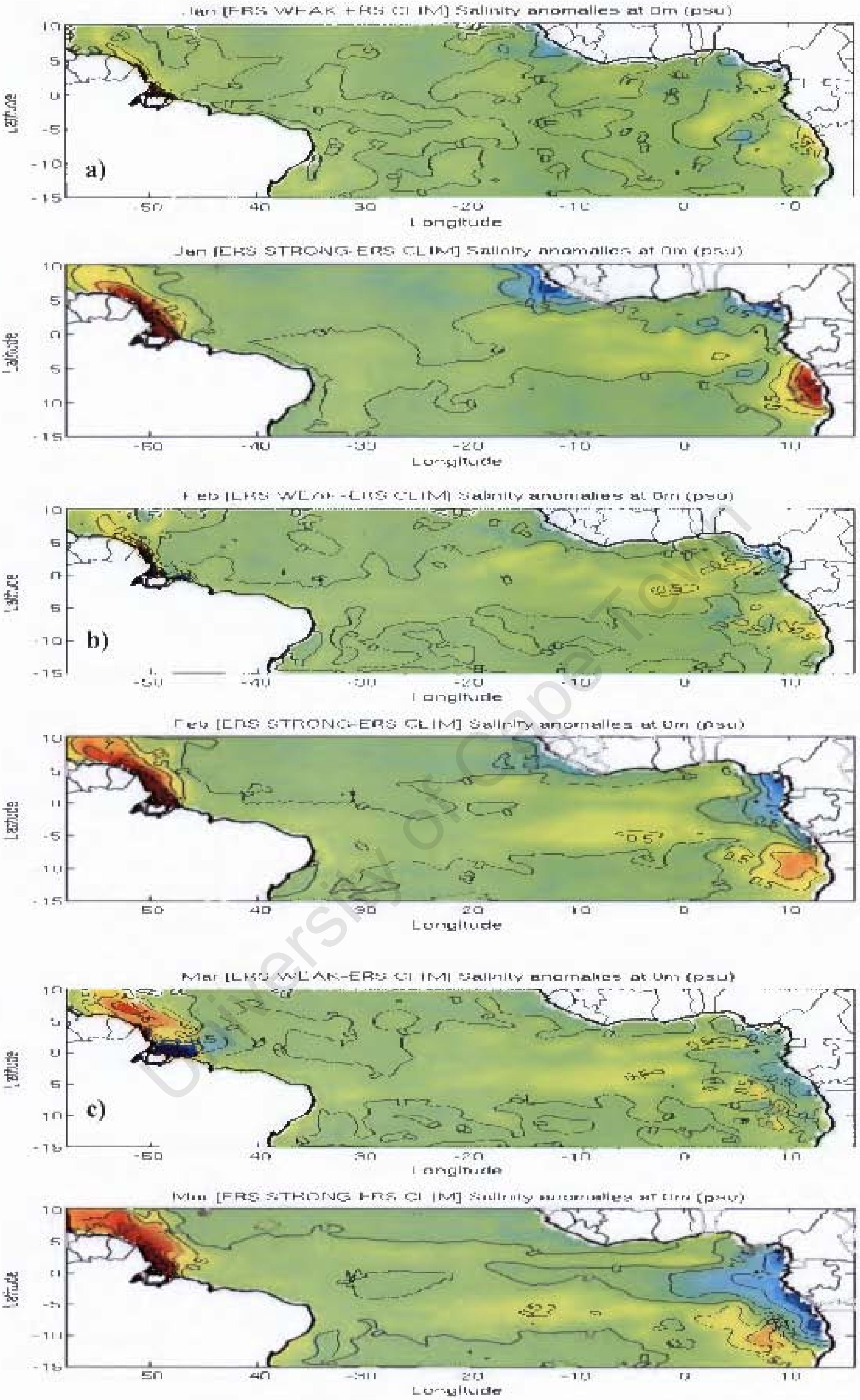

Figure 4.23: Sea surface salinity monthly mean anomaly, a) January, b) February and c) March. Top panel for ERS WEAK and bottom panel for ERS STRONG (contour interval 0.5 *psu*).

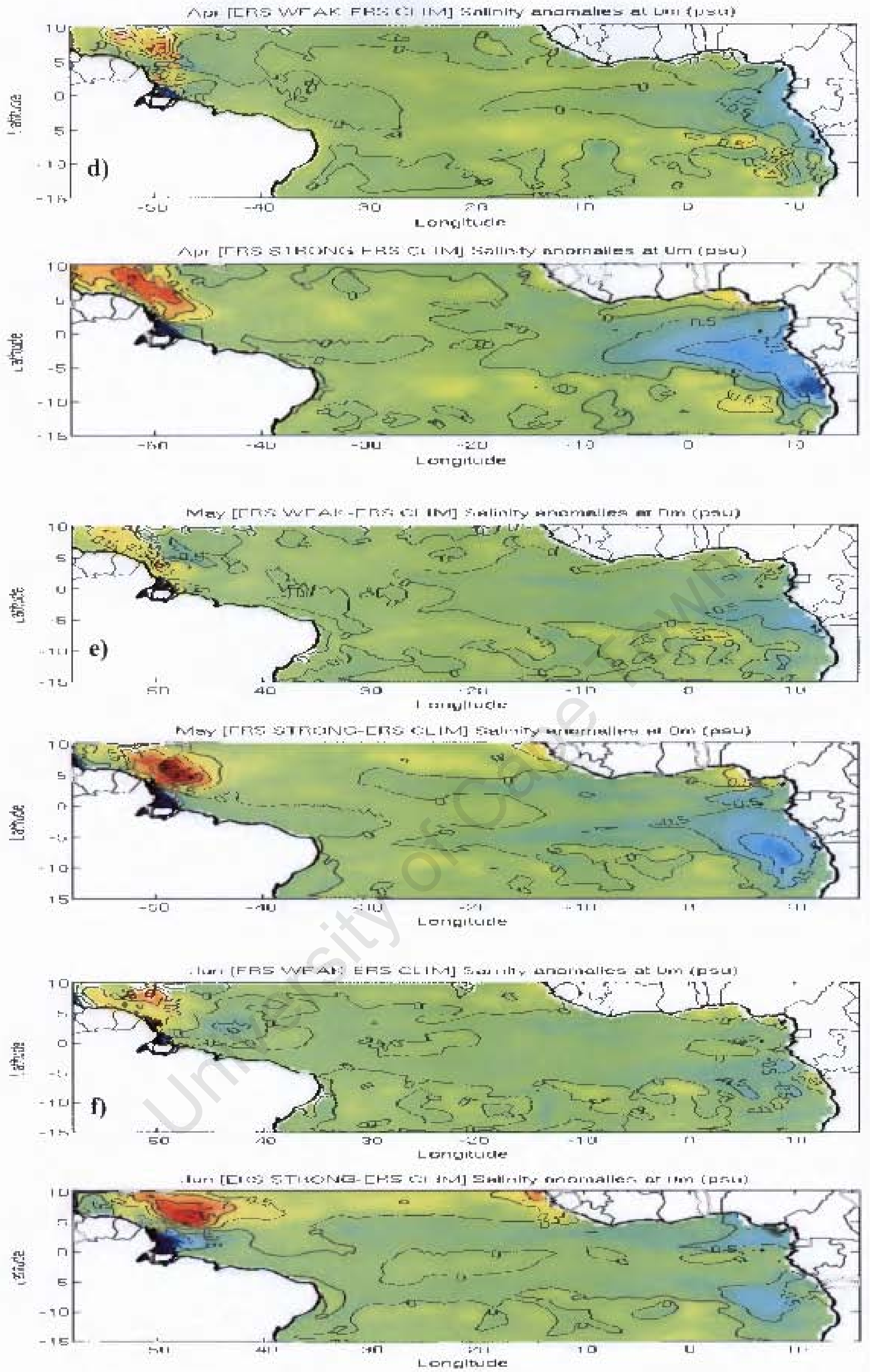

Apr [ERS WEAK-ERS CLIM] Salinity anomalies at 0m (psu)

Apr [ERS STRONG-ERS CLIM] Salinity anomalies at 0m (psu)

May [ERS WEAK-ERS CLIM] Salinity anomalies at 0m (psu)

May [ERS STRONG-ERS CLIM] Salinity anomalies at 0m (psu)

Jun [ERS WEAK-ERS CLIM] Salinity anomalies at 0m (psu)

Jun [ERS STRONG-ERS CLIM] Salinity anomalies at 0m (psu)

Figure 4.23: cont., d) April, e) May and f) June. Top panel for ERS WEAK and bottom panel for ERS STRONG (contour interval 0.5 *psu*).

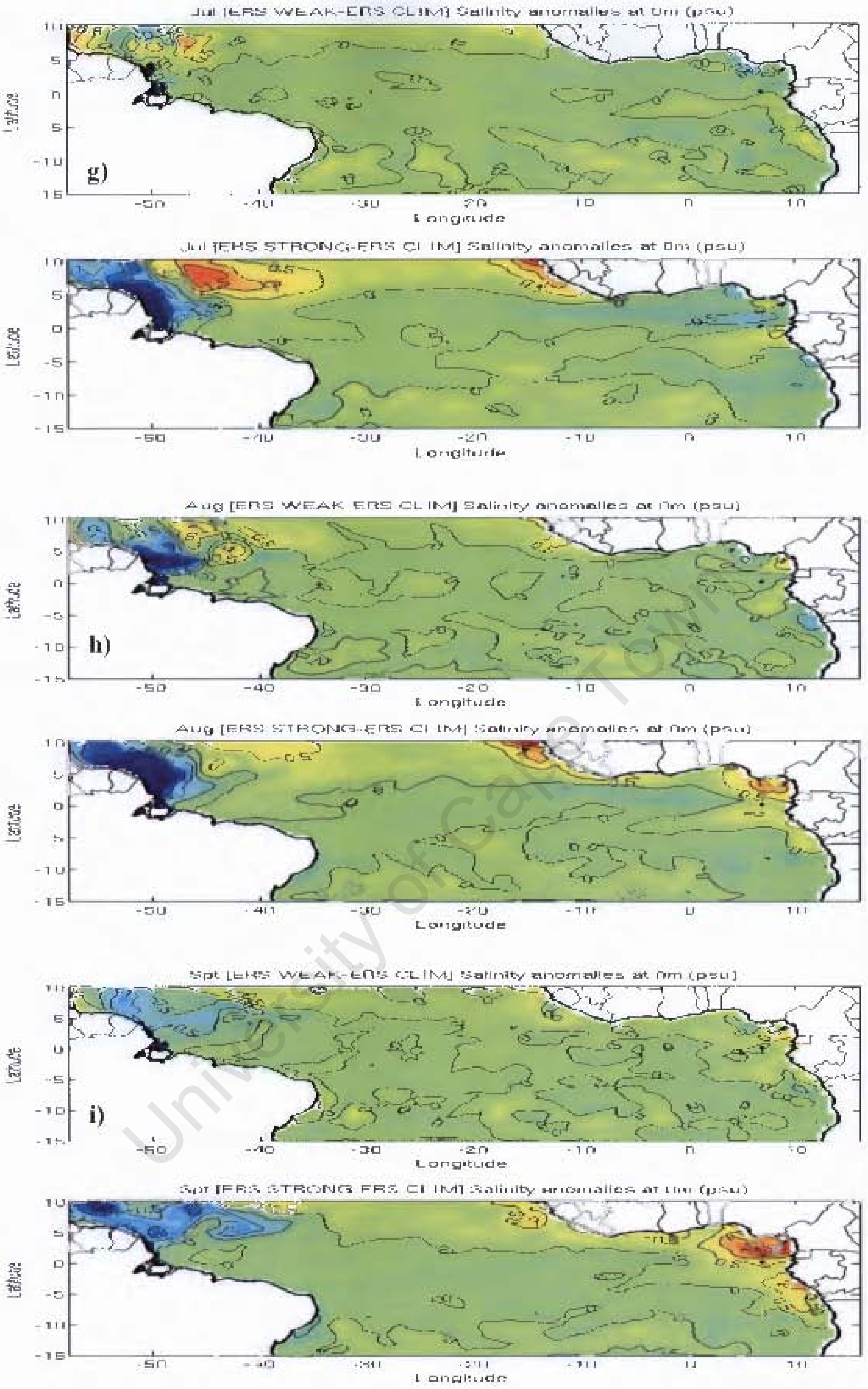

Figure 4.23: cont., g) July, h) August and i) September. Top panel for ERS WEAK and bottom panel for ERS STRONG (contour interval 0.5 *psu*).

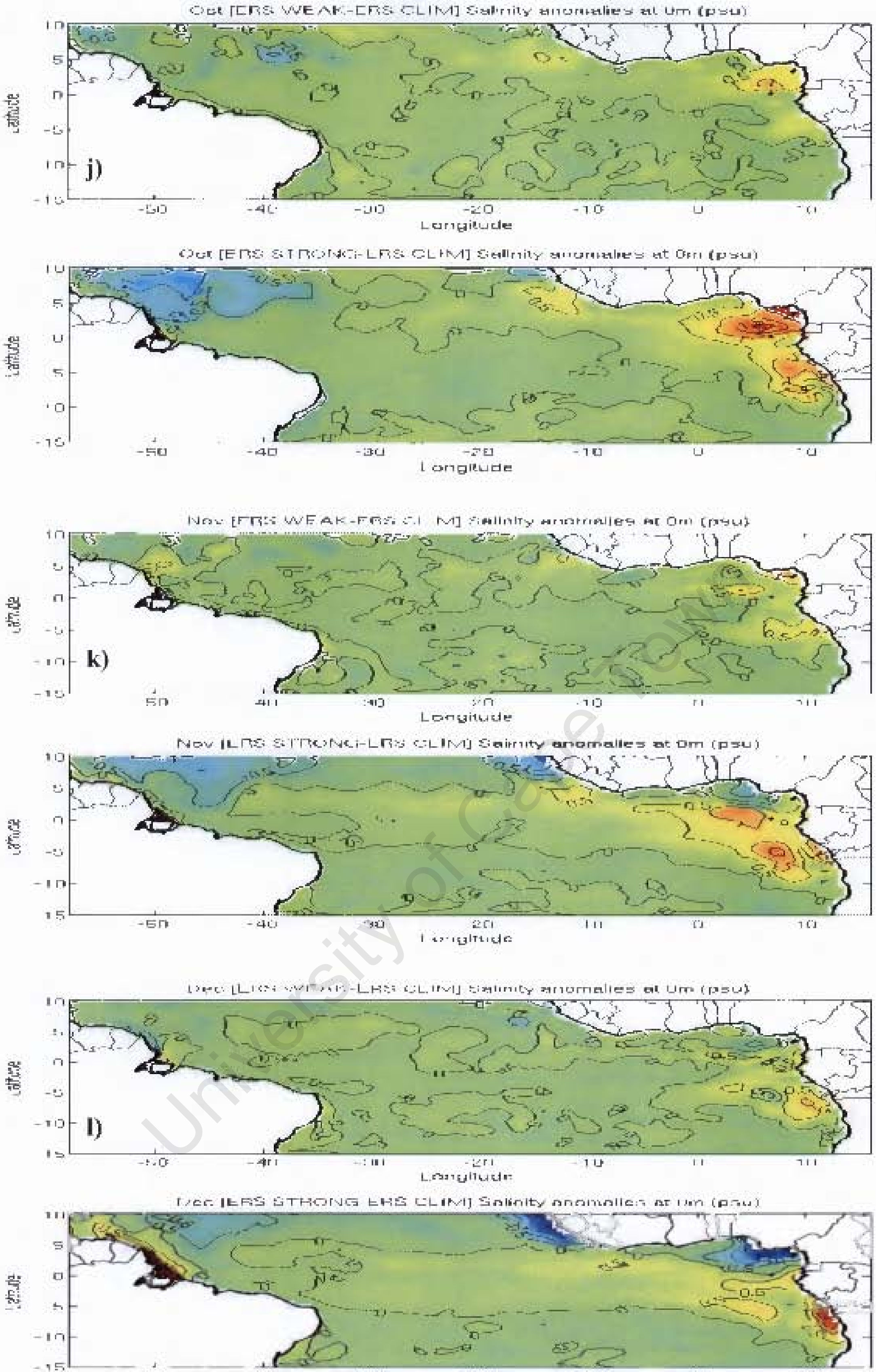

Figure 4.23: cont., j) October, k) November and l) December. Top panel for ERS WEAK and bottom panel for ERS STRONG (contour interval 0.5 *psu*).

4.2.3 Velocity

Comparing the surface currents of the three simulations (ERS CLIM, WEAK and STRONG), it is clear that as a result of the artificial strengthening, the ERS STRONG simulation shows stronger currents during January and February than ERS CLIM and ERS WEAK. In the ERS STRONG simulation, the cSEC/nSEC system doubles its zonal velocity (0.6ms^{-1}) compared to the ERS CLIM (0.3ms^{-1}). The strengthening of the cSEC/nSEC system has a strong impact on the NBC, which becomes faster (0.9ms^{-1}) than ERS CLIM (0.6ms^{-1}) during these months (see **Figure 4.24(a-b)** and **Figure 4.25(a-b)**). In contrast, the ERS WEAK simulation reveals a reversal of the nSEC along and to the north of the equator, whereas the cSEC is present but slightly weaker than in the ERS CLIM experiment. As the NBC is fed by the cSEC, and to some extent by the nSEC, the reduction and reversal of these currents reduces the NBC flow (see **Figure 4.24(a-b)** and **Figure 4.25(a-b)**).

During January and February in the eastern Atlantic, the results from ERS STRONG show a stronger cSEC/nSEC system than the other two simulations. In March, with the onset of the trade winds, there is an evident acceleration of the cSEC/nSEC in ERS CLIM and WEAK, whereas in ERS STRONG the cSEC/nSEC is disrupted by an eastward flow near the equator, extending from the South American coast to as far as 15°W (see **Figure 4.24(c)** and **Figure 4.25(c)**). In April the cSEC/nSEC is fully developed in both ERS CLIM and WEAK and consequently, the NBC accelerates and becomes a steady strong flow along the entire north Brazilian coast (see **Figure 4.24(d)** and **Figure 4.25(d)**). However, in the ERS STRONG simulation, the eastward flow disrupting the cSEC/nSEC strengthens in April, then weakens in May, when it reaches its maximum extension along the equator, and in June it is no longer visible along the equator. The results suggest that this eastward flow is fed by the recirculation of the cSEC and nSEC near the north Brazilian coast.

It is important to note that in the ERS WEAK results, from April to June (see **Figure 4.24(d-f)** and **Figure 4.25(d-f)**) and south of the cSEC, near 5°S, there is an evident eastward flow crossing the entire Atlantic that turns south-east as it arrives near 0°E and terminates in the ABF region.

From May to June and north of 5°N, the NECC flow takes shape to become fully developed in July across the entire Atlantic basin (see **Figure 4.24(e-f)** and **Figure 4.25(e-f)**). The NECC signature is evident in all three simulations but the results of ERS STRONG exhibit a one-month delay compared to the other two simulations. In other words, the NECC strongest values in the ERS CLIM and WEAK experiment occur during July; by September/October the NECC is no longer present. In the ERS STRONG experiment the NECC reaches its maximum values in August and remains present until October/November (see **Figure 4.24(i-l)** and **Figure 4.25(i-l)**).

Although the AC modelled by ERS CLIM is not accurately represented, the sensitivity simulations reveal some variations of this current. As seen in **Figure 4.26**, one month after the wind relaxation, in both ERS WEAK (actual artificial relaxation) and ERS STRONG (when wind stress returns to climatological values) there is an evident strengthening of the AC. In the ERS WEAK results (see **Figure 4.26(b-c)**), the strengthening of the AC is visible during February and March and coincides with the January- March relaxation of the artificial winds. In contrast, the ERS STRONG results show similar strengthening of the AC during April and May (see **Figure 4.26(b-c)**) which is linked to the wind relaxation that occurs when the wind stress forcing returns to the original values.

Analysing the zonal volume transport at the different locations along the equator reveals that greatest changes in the EUC transport occur during the months of anomalous winds. This is particularly true in the section along 30°W, which lies in the area where the artificial winds were applied. As seen in **Figure 4.27(b)**, from February to May the EUC undergoes a strong strengthening and weakening for ERS STRONG and ERS WEAK respectively. The biggest difference between the simulations is found in March, with ERS STRONG reaching a maximum transport value of 17.5Sv, ERS CLIM reaching 14Sv, and ERS WEAK reaching a minimum value of 11Sv. From April to July the results of ERS STRONG exhibit a drastic decrease in the EUC transport, which in September it drops to a minimum value of ~13Sv. In contrast, the EUC resulting from the ERS WEAK experiment undergoes a steady increase in transport from April to August, reaching a maximum value of 17Sv. The major changes in the EUC transport are a result of the artificial wind forcing from January to March, as well as the return of the forcing to the original climatological wind field. The influence of the different wind stress forcing is also clear at the surface, and the cSEC and nSEC show high variability between the three simulations (see **Figure 4.27(a**).

The impact of the artificial wind stress on the transport of both EUC and cSEC/nSEC are clearky evident in the eastern Atlantic. As seen in **Figure 4.28,** the zonal mean transport at 0°E is lower than at 30°W and the transport anomalies are more obvious from April to June, whereas at 30°W changes in the transport were visible from February. Comparing ERS STRONG to ERS CLIM, the EUC transport at 0°E is generally stronger in ERS STRONG until May, with a maximum difference of 6Sv. In contrast, the ERS CLIM results show that the EUC is on average 2Sv stronger than ERS STRONG from June to December (see **Figure 4.28(b)**). The EUC transport in ERS WEAK is very similar to ERS CLIM until May, weaker from June to August (with a maximum difference of 4Sv in June), stronger between September and October (2Sv difference) and, finally, weaker again for the rest of the year (with a maximum difference of 4Sv in November) (see **Figure 4.28(b)**).

At the surface, the transport associated with the cSEC/nSEC system also reveals stronger difference amplitudes from April to June (see **Figure 4.28(a)**). During this period the transport values in ERS STRONG are weaker than ERS CLIM by 4Sv, whereas the transport in ERS WEAK is stronger than ERS CLIM by 3Sv. From July to August there is an evident reduction of the transport in all three simulations. In September, the numerical results from ERS CLIM exhibit a reversal of the flow (very weak flow), and the transport values in ERS WEAK and ERS STRONG are respectively ~ 2Sv and~0.1Sv (see **Figure 4.28(a)**). The results of ERS CLIM show abrupt strengthening of transport in October, a reduction/reversal in November, and finally a minimum transport value of 0Sv in December. However, the transport in ERS STRONG gradually increases until December, reaching a value of 2Sv, while in the ERS WEAK experiment the transport increases until November and then de]creases drastically, reaching a minimum value of 0Sv in December.

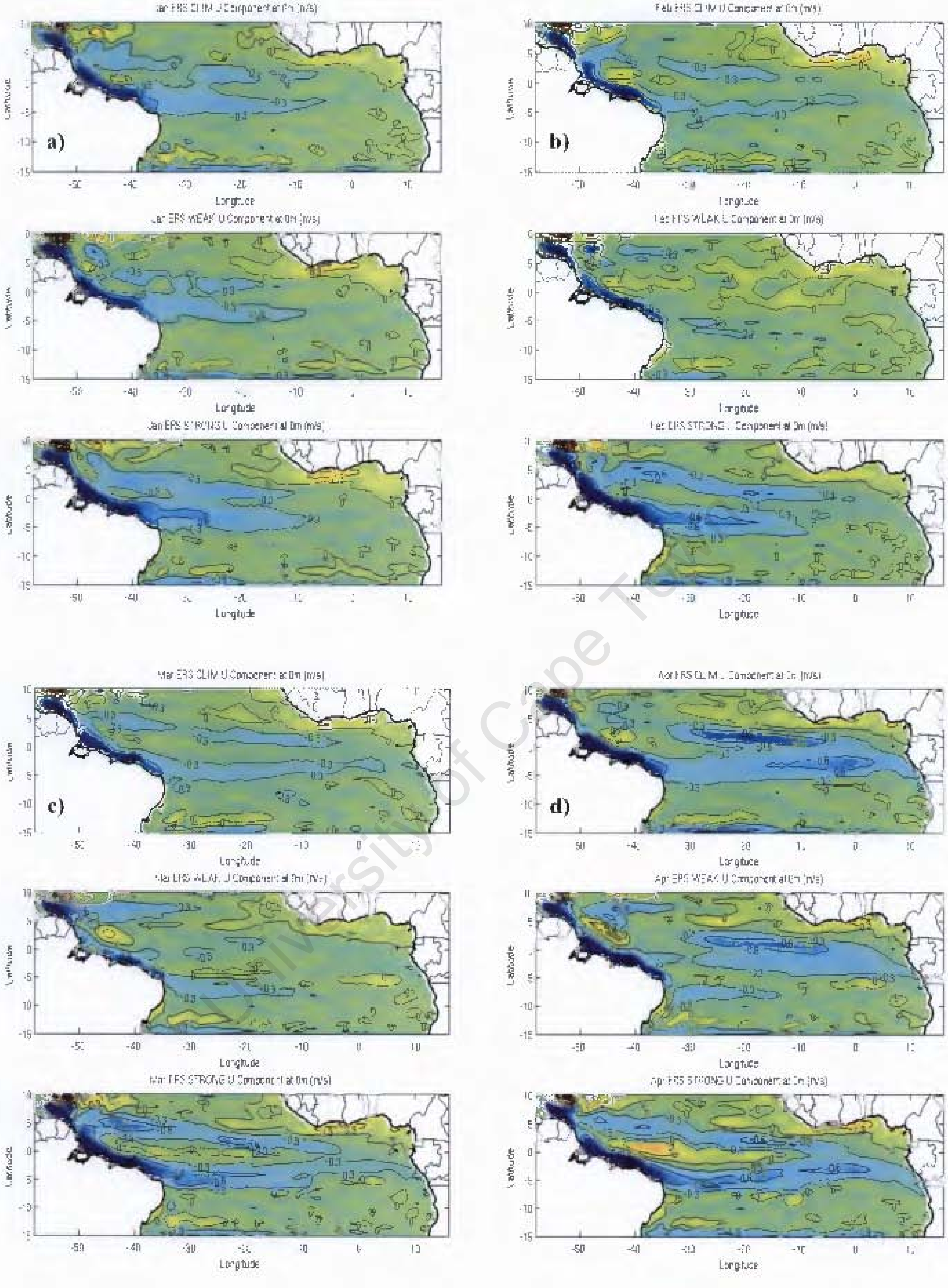

Figure 4.24: Surface U component monthly mean, a) January, b) February, c) March and d) April. Top panels for ERS CLIM, middle panels for ERS WEAK and bottom panels for ERS STRONG (contour interval $0.1 ms^{-1}$).

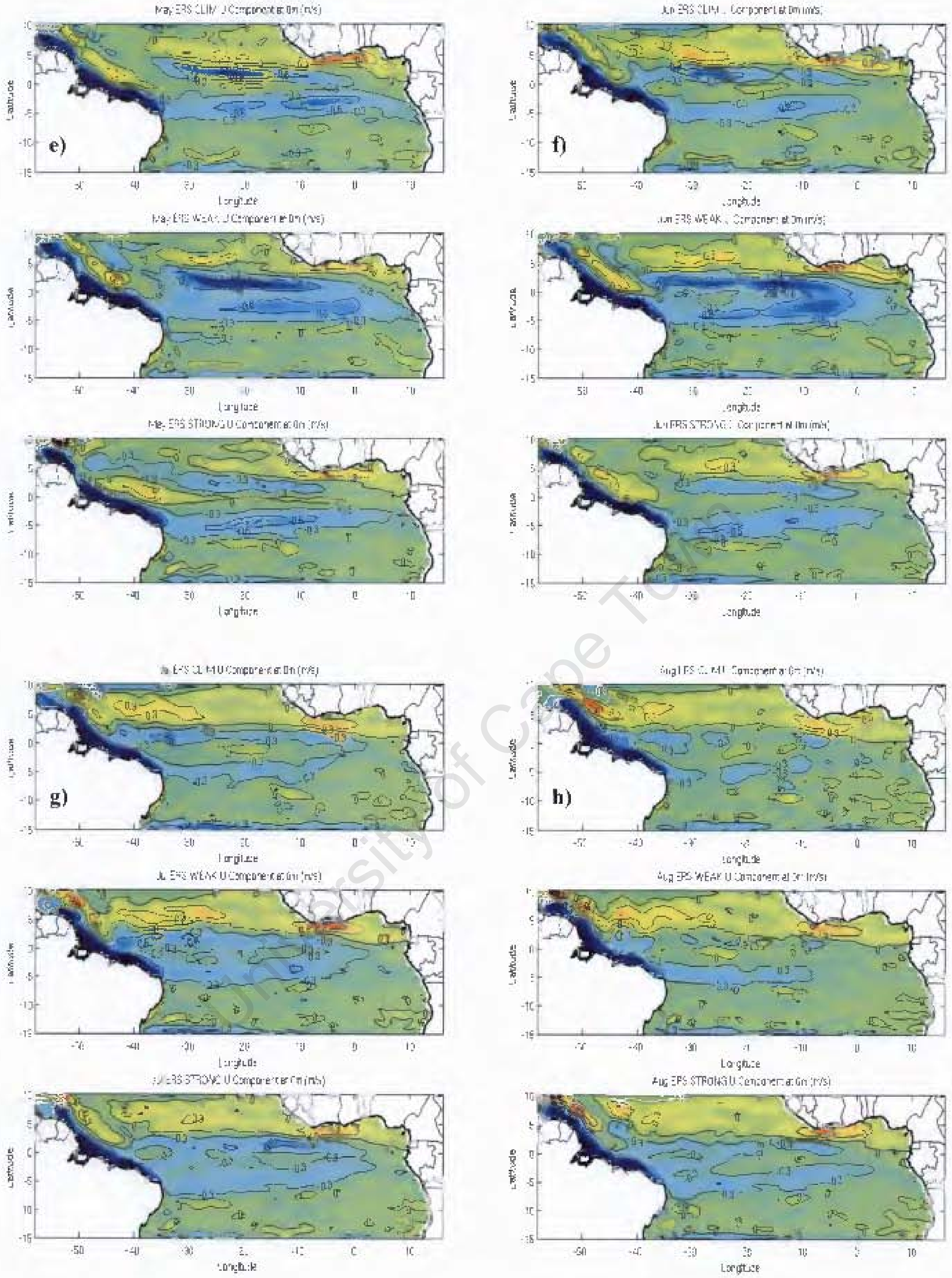

Figure 4.24: cont., e) May, h) June, f) July and g) August. Top panels for ERS CLIM, middle panels for ERS WEAK and bottom panels for ERS STRONG (contour interval 0.1ms^{-1}).

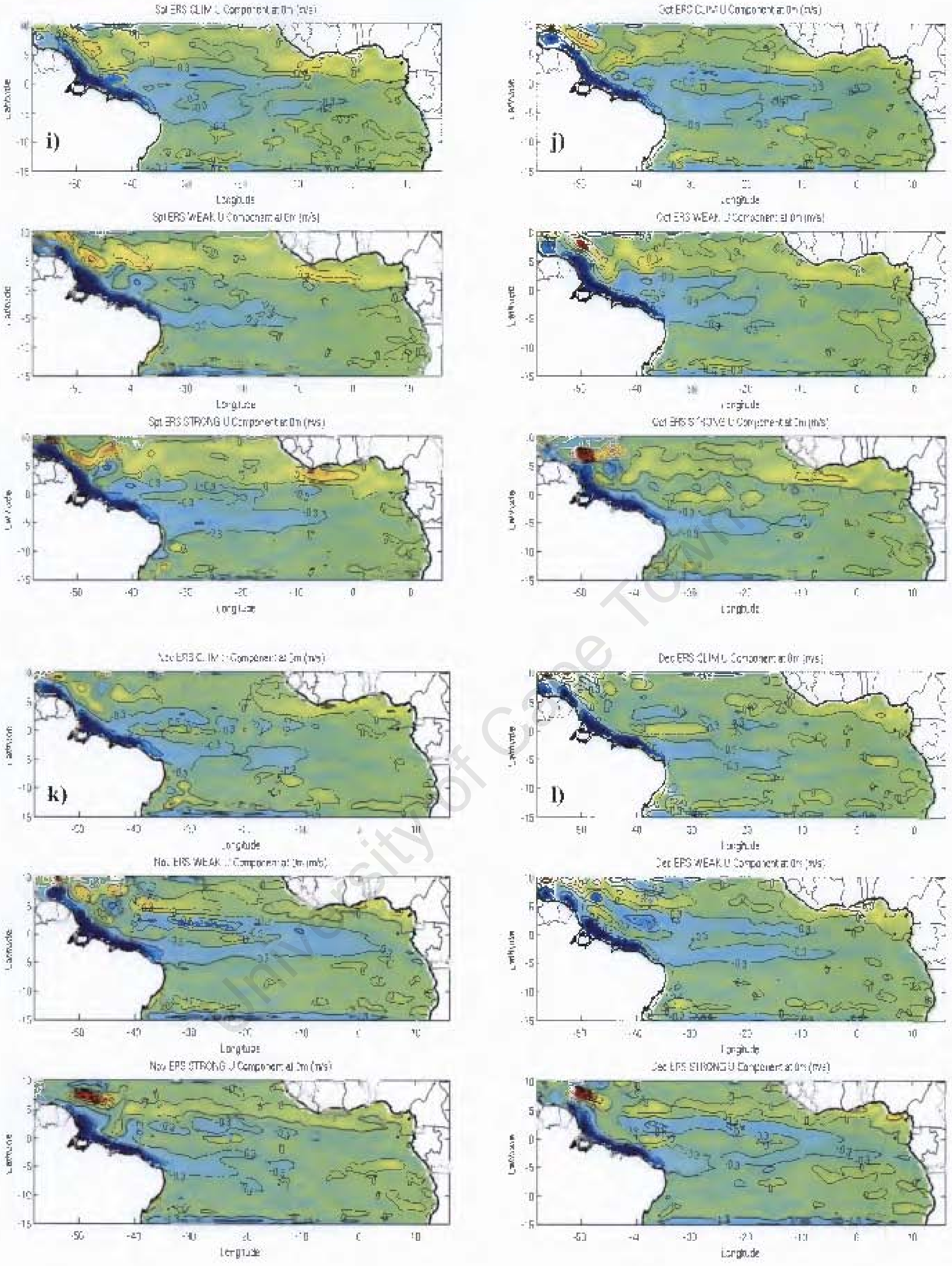

Figure 4.24: cont., i) September, j) October, k) November and l) December. Top panels for ERS CLIM, middle panels for ERS WEAK and bottom panels for ERS STRONG (contour interval $0.1 ms^{-1}$).

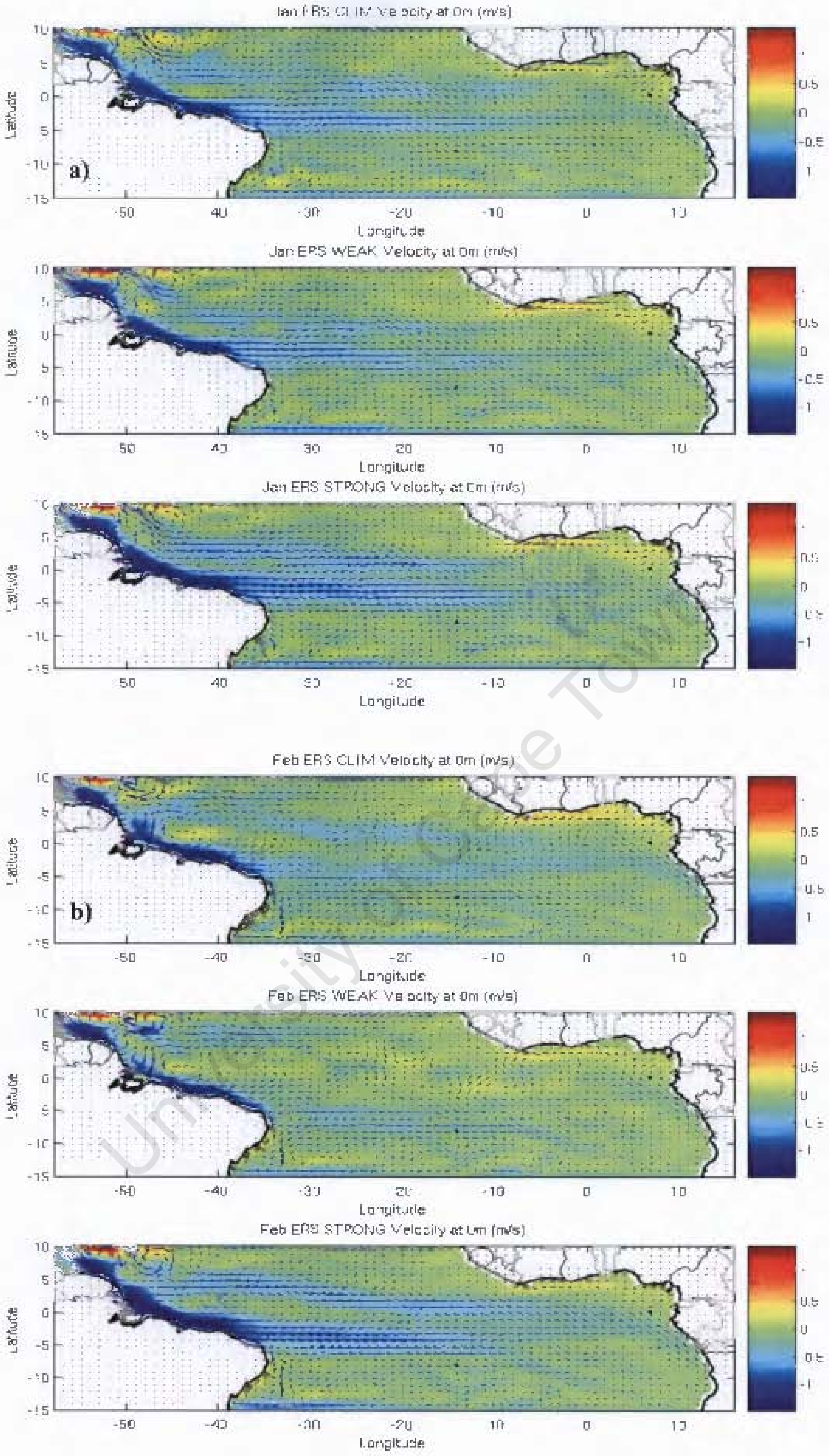

Figure 4.25: Surface Velocity monthly mean quiver, a) January and b) February. Top panels for ERS CLIM, middle panels for ERS WEAK and bottom panels for ERS STRONG (ms^{-1}).

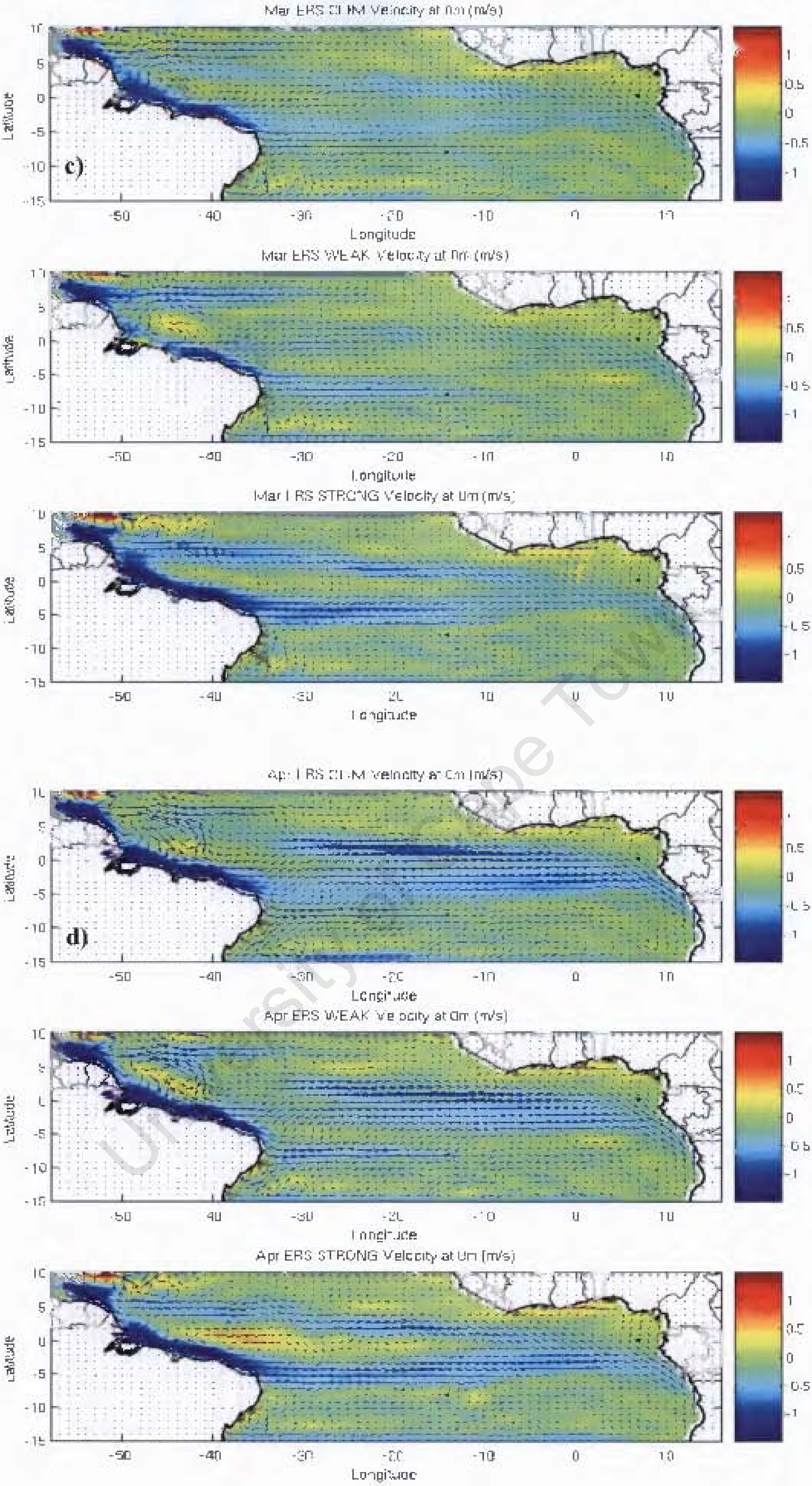

Figure 4.25: cont., c) March and d) April. Top panels for ERS CLIM, middle panels for ERS WEAK and bottom panels for ERS STRONG (ms^{-1}).

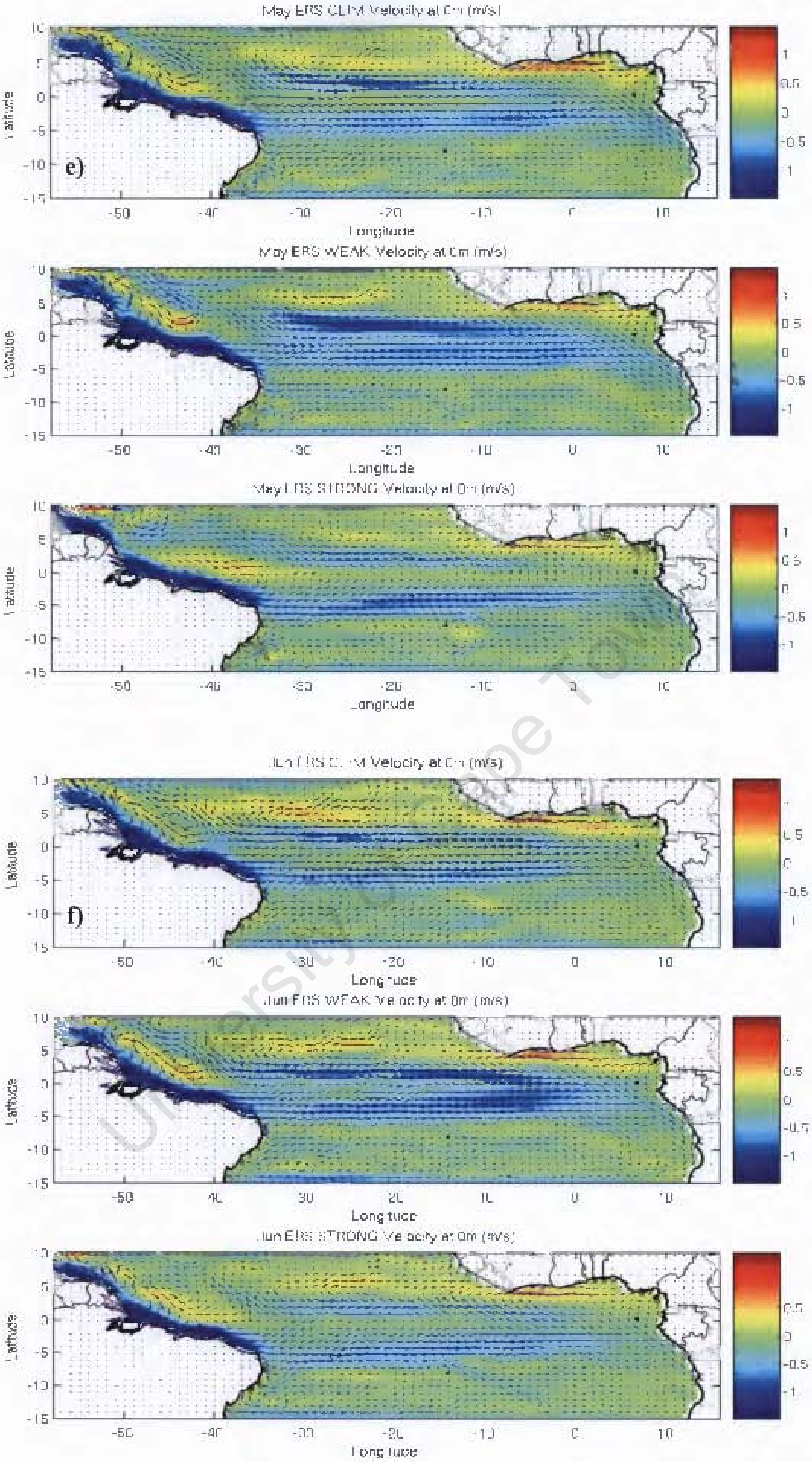

Figure 4.25: cont., e) May and f) June. Top panels for ERS CLIM, middle panels for ERS WEAK and bottom panels for ERS STRONG (ms^{-1}).

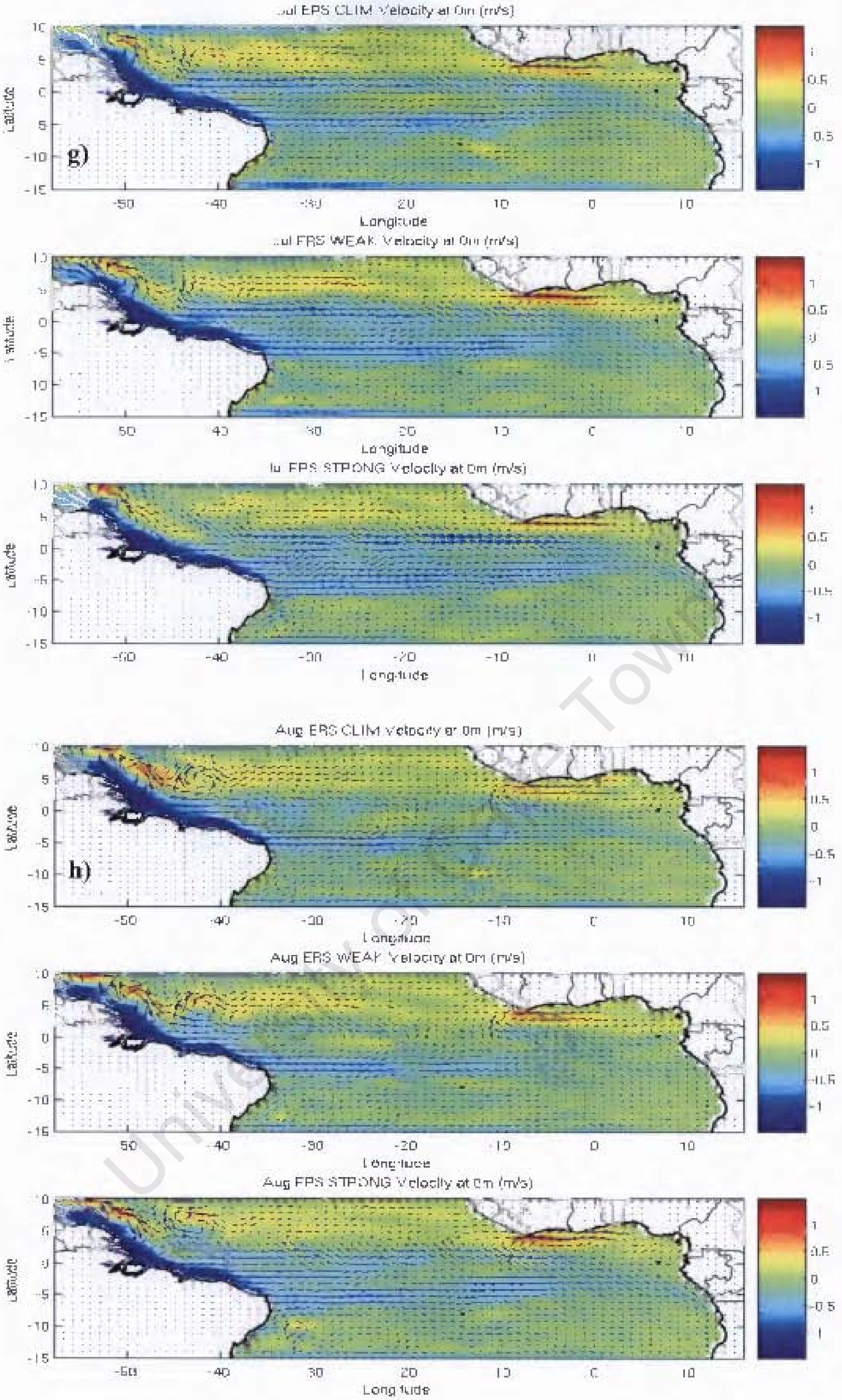

Figure 4.25: cont., g) July and h) August, Top panels for ERS CLIM, middle panels for ERS WEAK and bottom panels for ERS STRONG (ms^{-1}).

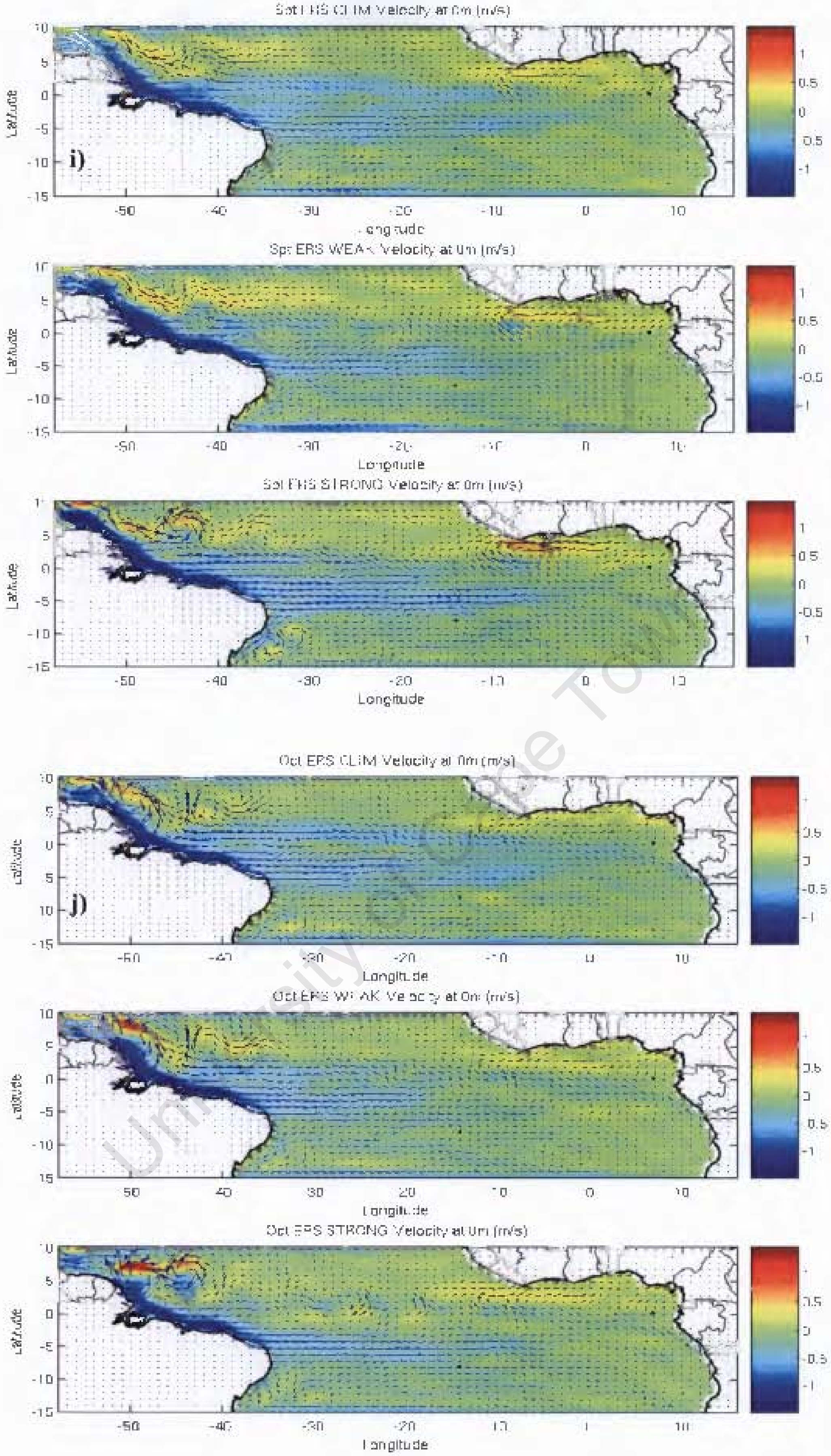

Figure 4.25: cont., i) September and j) October. Top panels for ERS CLIM, middle panels for ERS WEAK and bottom panels for ERS STRONG (ms^{-1}).

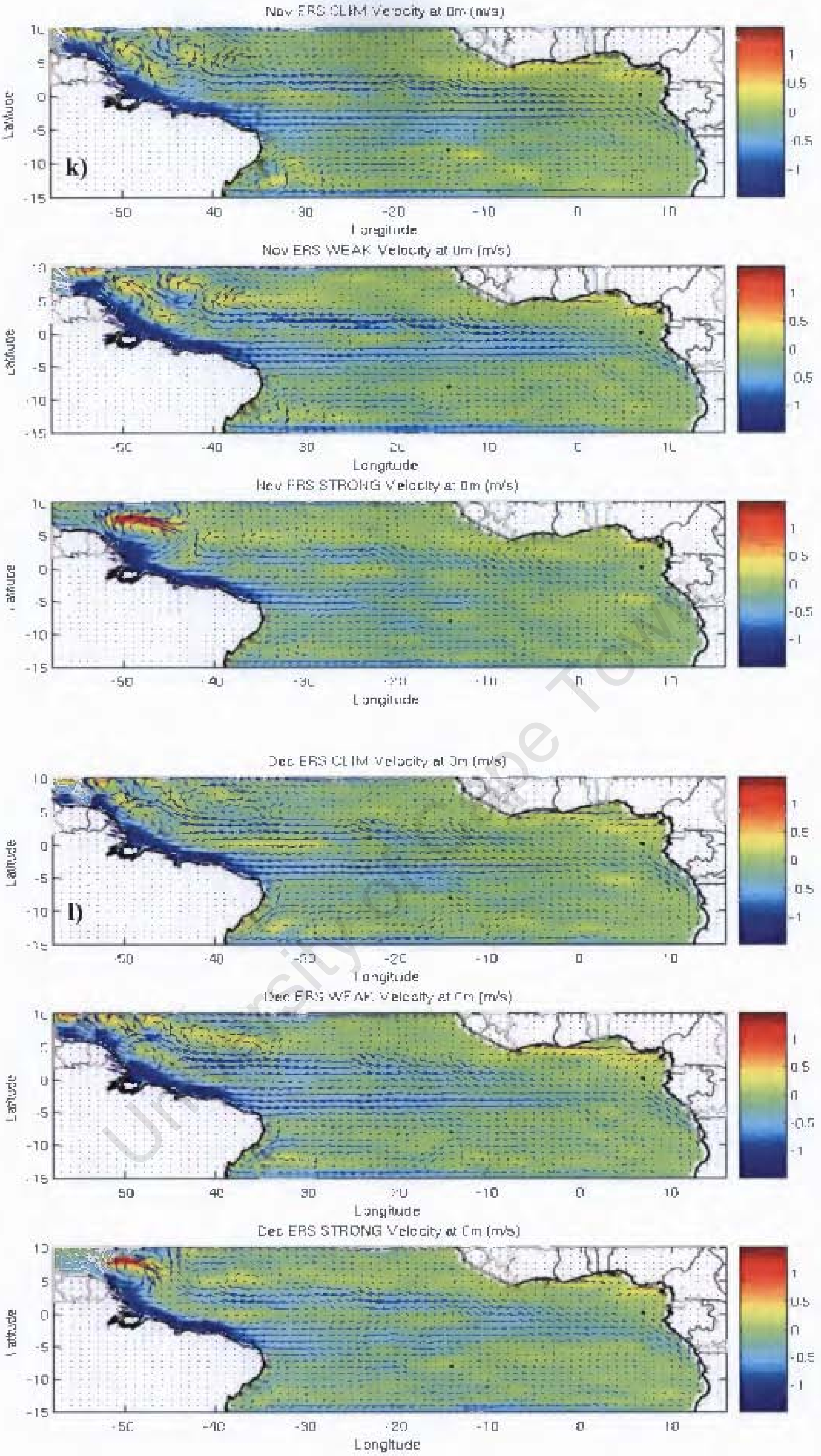

Figure 4.25: cont., k) November and l) December. Top panels for ERS CLIM, middle panels for ERS WEAK and bottom panels for ERS STRONG (ms^{-1}).

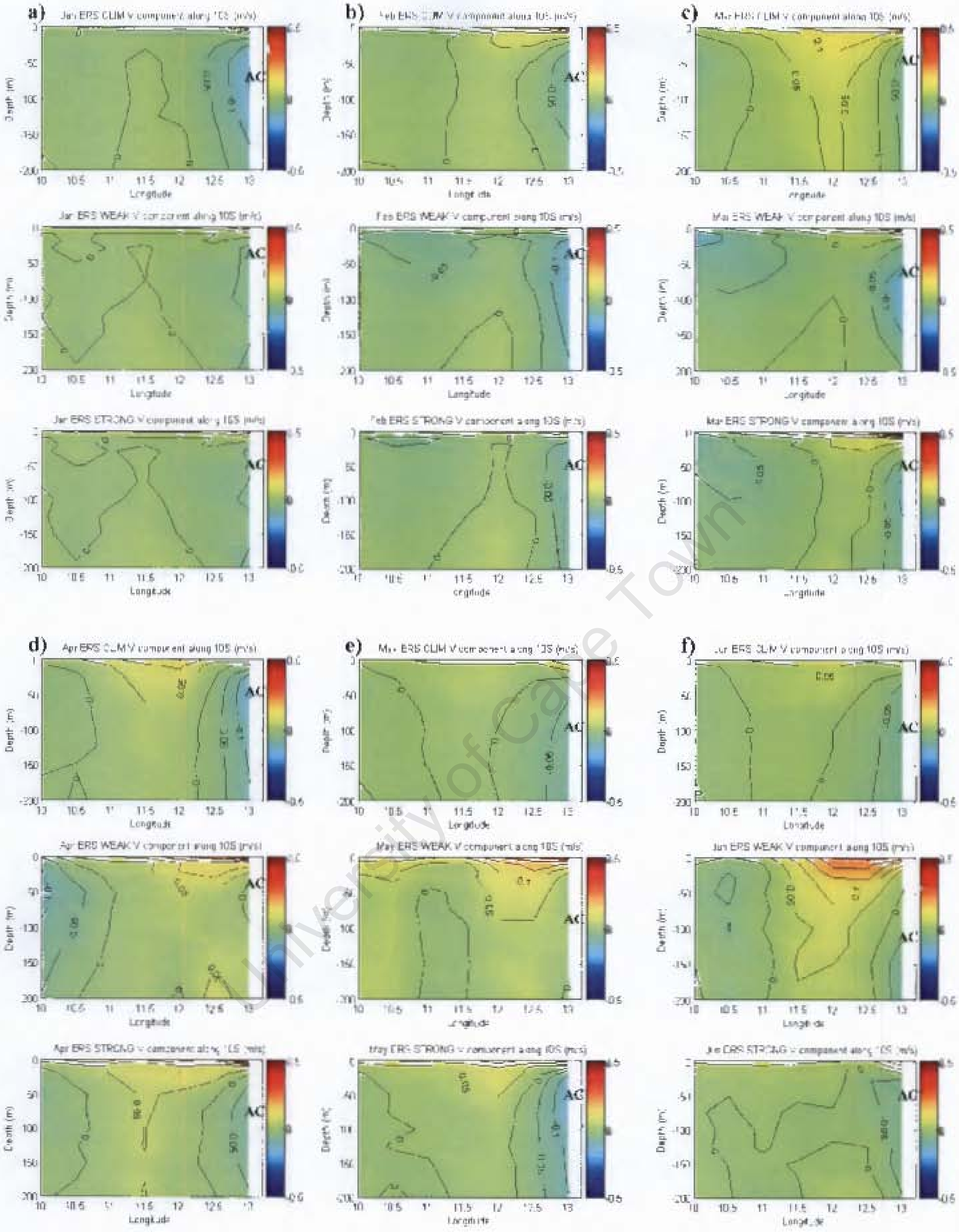

Figure 4.26: V component vertical section along 10°S, monthly mean, a) January, b) February, c) March, d) April, e) May and f) June. Top panel for COADS CLIM and bottom panel for ERS CLIM (contour interval 0.1ms^{-1}, positive values correspond to eastward flow). Shown is: Angola Current (AC).

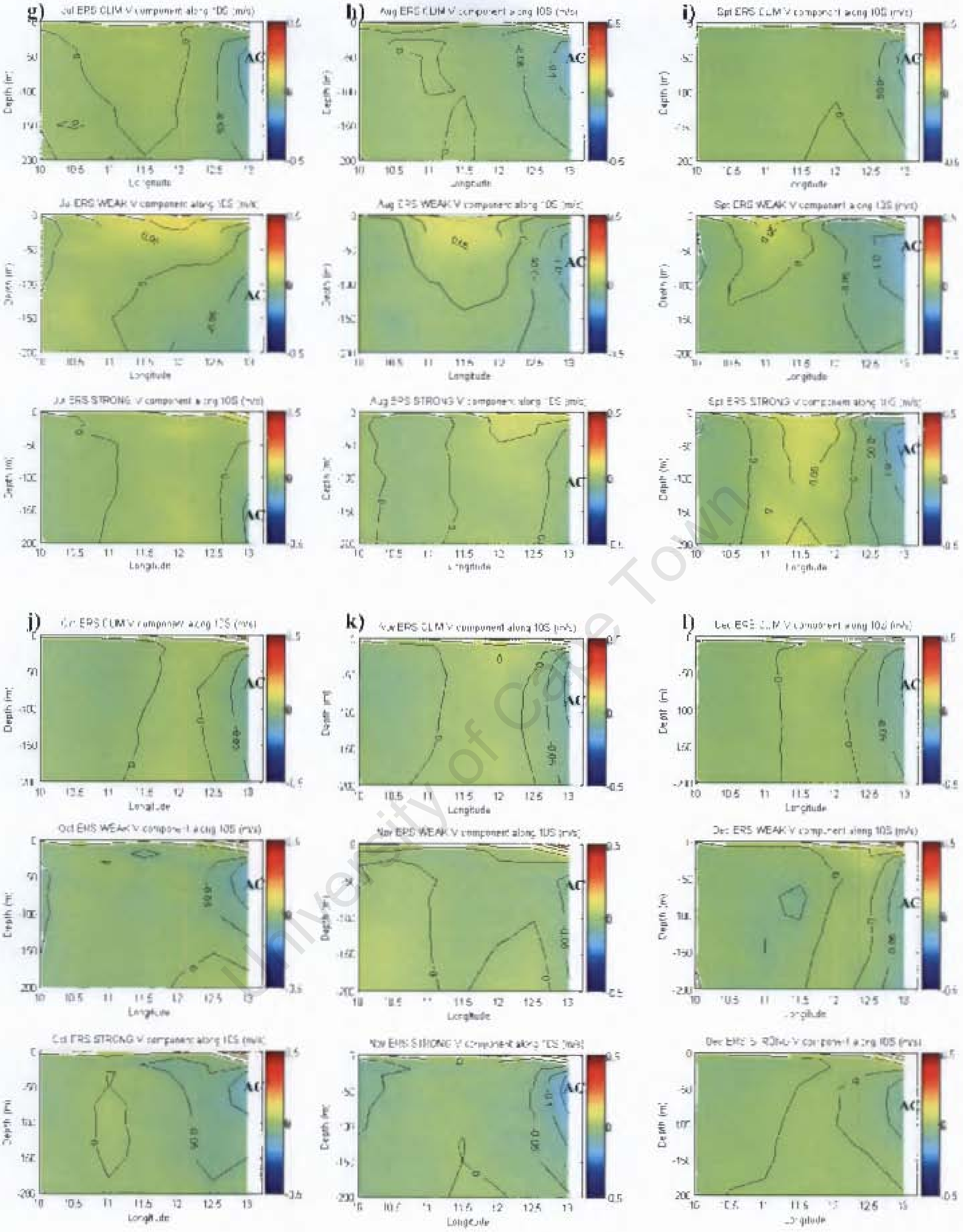

Figure 4.26: cont., g) July, h) August, i) September, j) October, k) November and l) December. Top panel for COADS CLIM and bottom panel for ERS CLIM (contour interval 0.1ms^{-1}, positive values correspond to eastward flow). Shown is: Angola Current (AC).

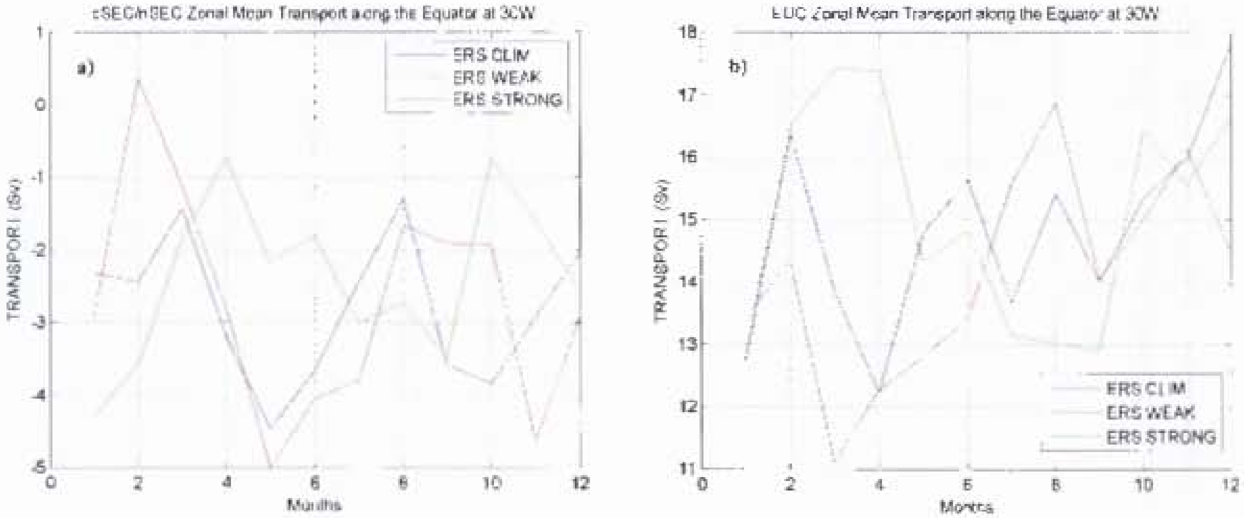

Figure 4.27: Zonal mean transport time series at 30°W, a) cSEC/nSEC and b) EUC.

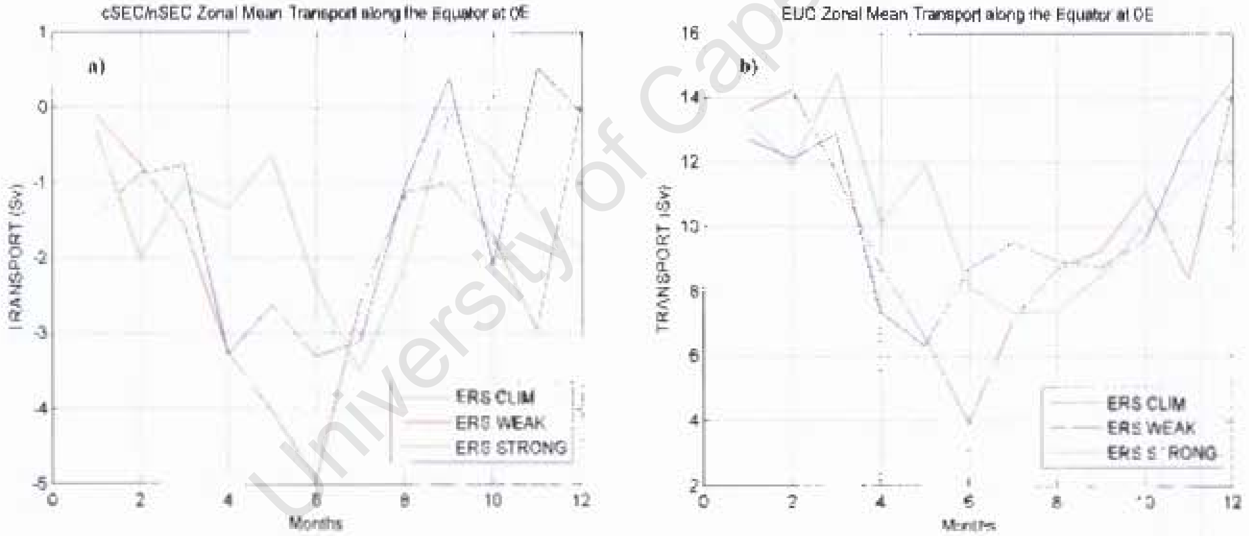

Figure 4.28: Zonal mean transport time series at 30°W, a) cSEC/nSEC and b) EUC.

4.2.4 Discussion

The model is responding as expected to different wind forcing, i.e. when wind relaxation in the western Atlantic is induced, the equatorial thermocline is deeper in the eastern Atlantic and vice versa (see **Figure 4.19(c-d)**). During the 1984 Benguela, Niño Hisard *et al.* (1986) reported a similar thermocline structure along the equator, i.e. the thermocline was systematically deeper than in 1983, particularly in the eastern Atlantic. Conversely, when strengthening is induced the model responds with a deeper thermocline in the western Atlantic and vice versa.

Under a wind stress relaxation, a strong positive anomaly is evident along the equator and in the ABF region, whereas when wind stress strengthening results in negative anomalies are evident along the equator but with a smaller impact on the ABF region (**Figure 4.20(a-l)** and **Figure 4.21(a-d)**). The eastward propagation of the temperature anomalies is in agreement with previous studies (e.g. Florenchie *et al.*, 2003; Florenchie *et al.*, 2004). However, according to the previous studies the temperature anomalies were expected to be subsurface, to propagate along the equator and to outcrop only in the ABF region. The numerical results are not in agreement with these studies, i.e. the positive temperature anomalies resulting from the sensitivity experiments are observed at the surface over the entire equatorial Atlantic before they reach the ABF region. It is important to note that the presence of the warm anomalies at the surface could be explained by shallower than expected thermocline depth in ERS CLIM (i.e. the WOA01 shows a thermocline depth ranging between 50-80m during AMJ from 20°W to the African coast, compared to 30-40m in the ERS CLIM results), thus allowing the temperature anomalies to outcrop in the equatorial region.

In contrast, the cold anomalies are induced by a shallowing of the equatorial thermocline (driven by upwelling Kelvin waves), and could be regarded as a remotely forced equatorial upwelling. The temperature anomalies observed in both ERS WEAK and ERS STRONG after the wind stress forcing returns to its climatological values have not been documented during real Benguela Niños/Niñas events. However, it is necessary to take into account that the artificial wind stress does not fully represent the conditions during Benguela Niño/Niña events, particularly the fast and marked increase/decrease on the wind stress field when the forcing returns to its climatological values.

From the analysis of the velocity components at the surface and 100m depth and the zonal transport time series at different locations along the equator (30°W and 0°E), it is evident that the model is sensitive to the artificial changes induced in the wind forcing. The equatorial current system response is clear, particularly north of the equator where the greatest changes are observed. These results are consistent with previous studies that suggested a greater variability of the surface currents north of the equator (Merle and Arnault, 1985).

The monthly variability of the zonal volume transport shows dramatic changes in the cSEC/nSEC and EUC currents during the months of induced artificial winds and restored original wind forcing. Furthermore, from the volume transport analysis it is clear that the changes induced in the wind field during January, February, March (artificial field) and April (return to original field) affect the entire oceanic circulation throughout the year. The response of the EUC to the different wind forcing is in agreement with the EUC driving mechanism suggested by Arthur (1960), which linked the EUC to the zonal field over the western equator. According to this theory, the accumulation of water on the western boundary due to frictional action of the easterlies over this area creates a subsurface eastward pressure gradient. When the wind increases (ERS STRONG) or decreases (ERS WEAK) over the western Atlantic there is an evident strengthening or weakening of the EUC due to an enhanced or reduced eastward pressure gradient.

The appearance of the eastward flow south of 5°S in the ERS WEAK results is consistent with Hisard *et al.* (1986), who observed an unusual eastward flow near 5°S during the 1984 Benguela Niño. According to Hisard *et al.* (1986) and Shannon *et al.* (1986), this a flow would be responsible for the advection of warm, saline waters into the northern Benguela system, thus disrupting the ABF. The eastward flow observed in the ERS WEAK results, in association with warm anomalies being propagated as Kelvin waves, could thus be responsible for the warm anomalies observed along the Angolan coast.

The AC shows a strengthening one month after wind reductions and this feature is seen in both ERS WEAK (February) and STRONG (May) simulations. The strengthening of the AC persists for two months and this short term change in the AC flow could also be regarded as the signature of a Kelvin wave propagating along the African coast. Nevertheless, the strengthening of the AC would be enough to propagate surges of warm saline water of equatorial origin and disrupt the ABF region. These results would be in agreement with Gammelsrød *et al.* (1998) who, during the 1995 Benguela Niño, observed a stronger than usual poleward flow along the Angolan coast.

As discussed in **section 4.1.2,** the regions that reveal stronger salinity variability in the equatorial Atlantic are Biafra Bay and the coastal areas near the Amazon and the Congo River mouth. The spatial extension of their freshwater plumes strongly depends on advection factors. Since the equatorial current system is coupled to the variability of the trade winds, the artificial changes induced on the wind stress field trigger changes on the equatorial current system, and consequently impact on the advection of the freshwater plumes which is evident in both sensitivity experiments.

During the months of artificial stronger wind stress (January, February and March) the cSEC\nSEC transport is enhanced, and responsible for the advection of more saline water from the equator to the region of the Amazon River mouth, thus disrupting the freshwater plume (see **Figure 4.23(a-f)**). In July and August the ERS STRONG surface velocity field is weaker, and consequently causes the advection of saline waters to be reduced, which leads to the appearance of negative anomalies (see **Figure 4.23(g-h)**). Between September and the end of the year, the ERS STRONG results indicate the development of a cyclonic ring associated with the NBC retroflection, which advects the Amazon freshwater plume north-eastward (see **Figure 4.23(i-l)**).

The surface velocity fields from ERS CLIM and ERS WEAK do not differ significantly in January and February, so significant changes (due to advection) would not be expected in the salinity field. In March the surface velocity fields reveal some differences, i.e. those of ERS WEAK exhibit a weaker NBC and a stronger westward flow north of 5°N. This explains the salinity anomalies observed during March comprising a north-westward advection of the positive anomaly and appearance of a strong negative anomaly in the river mouth area (see **Figure 4.23(c)**). During austral autumn and winter (April-July), the appearance of a weak positive salinity anomaly is linked to a stronger velocity field in ERS WEAK than in ERS CLIM (see **Figure 4.23(d-g)**). From September to December the low salinity anomaly values observed in the north-western Atlantic are consistent with the similar velocity fields observed over this region in both ERS CLIM and ERS WEAK, which lead to similar salinity fields and consequently weak salinity anomalies (see **Figure 4.23(i-l)**). The salinity anomalies evident in the eastern Atlantic are linked to changes in the AC and GC. By analysing the velocity in this region, it is evident that the AC from ERS STRONG is slightly stronger than ERS CLIM in May, resulting in the advection of the freshwater plume from the Congo River to the ABF region (see **Figure 4.23(e-f)**).

The results from ERS WEAK show negative anomalies in the ABF region from March to June and these anomalies coincide with a strengthening of the AC in March and April. During the 1995 Benguela Niño, Gammelsrød *et al.* (1998) recorded negative salinity anomalies along the Angolan coast, which were attributed to the southward displacement of the Congo River freshwater plume. In both sensitivity experiments the presence of surface negative salinity anomalies is clearly visible along the Angolan coast (particularly in the ERS STRONG results) and they seem to be linked to a strengthening of the AC, which in turn enhances the advection of the Congo River freshwater plume along the Angolan coast.

5 Conclusions

The first objective of this investigation was to assess ROMS capabilities in reproducing the seasonal cycle of the upper ocean equatorial Atlantic. The second objective was to investigate the equatorial remote forcing of Benguela Niños, i.e. to determine whether wind stress anomalies in the western Atlantic generate the observed conditions for Benguela Niños? In other words, how does it remote forcing changes the characteristics of the seasonal variability of the equatorial Atlantic and of the ABF?

In order to investigate the seasonal cycle of the equatorial Atlantic as well as the model sensitivity to different wind forcing fields, two wind stress forcing fields were used, namely ERS and COADS. The results show that the model has some problems resolving the equatorial thermocline structure. This is related to the vertical mixing scheme (KPP parameterization), which only gives an estimation of the vertical mixing layer (h) through the Richardson number vertical shear (which is also parameterized). Another related issue is the fact that the oceanic boundary layer can also be forced from the interior ocean. This implies that Equatorial Undercurrent can lead to shear instability near h, thus impacting on the thermocline depth. Along the equator the ERS wind stress field is stronger than that of COADS, and as a result, the thermocline is shallower in the ERS CLIM results than for COADS CLIM. A comparative analysis of ocean climatology fields revealed that in both experiments (COADS and ERS CLIM) the equatorial upwelling is overestimated, i.e. it occurs from AMJ and JAS rather than only in JAS, along the equator the cold tongue extends further west than observed, and both numerical results show colder SST values than expected.

The surface equatorial current system is reasonably reproduced by the model. The North Brazilian Current (NBC) and the Angola Current (AC) are overestimated and underestimated respectively in both experiments. The poor representation of coastal currents can be explained by the 0.5° model resolution, which is not sufficient to resolve narrow coastal currents. Furthermore, since coastal currents are strongly dependent on bathymetry features, thus the model bathymetry interpolation could also explain the inaccurate representation of coastal currents.

Since the salinity field is relaxed towards climatology using a restoring term in salinity, the SSS results are in agreement with the observations. The freshwater plume variability associated with the Amazon River, Biafra Bay and Congo River are captured by the model in both COADS and ERS CLIM simulations.

The secondary objective of this thesis was to investigate the linkage between wind anomalies in the western Atlantic and Benguela Niños/Niñas. In order to investigate this, two sensitivity experiments were performed. In the first, ERS WEAK, the wind stress was artificially reduced by 50% during January and March and reduced by 75% in February. The wind stress anomalies were applied between 6°S-6°N and from the Brazilian coast to as far as 8°W. Conversely, in the second sensitivity experiment, ERS STRONG, the wind stress was enhanced using the same method.

The ERS WEAK results revealed that the model is able to reproduce the observed positive temperature anomalies, their subsurface propagation along the equator following the thermocline depth, and the southward propagation as a Kelvin wave along the African coast as far as the ABF area. The numerical results show that the warm anomalies take two months to propagate from the western Atlantic to the ABF region, which is consistent with the baroclinic wave propagation speed. The model results show an anomaly propagation speed of 1.7ms^{-1} which is consistent with the propagation of the baroclinic Kelvin wave. Analysis of the velocity field shows a strengthening of the Angola Current (AC), as a result of the baroclinic field adjustment, during the artificial relaxation of the wind stress, which is in agreement with previous observations conducted during the 1995 Benguela Niño event (Gammelsrød, 1998). In March and April an eastward surface current crosses the entire Atlantic basin near 5°S, advecting warm waters of equatorial origin into the ABF region. A similar feature was observed during the 1984 Benguela Niño (Hisard *et al.*, 1986). The impact of the artificial wind stress weakening is also evident in the nSEC/cSEC and EUC transport, which show a reduction in the transport associated with these currents during the wind stress relaxation period. The SSS field shows negative anomalies in the ABF area from March to May, suggesting that the Congo River freshwater plume is displaced southwards during the artificial Benguela Niño event and is probably linked to the strengthening of the AC observed in March.

When the model is forced with stronger wind stress (ERS STRONG) it reproduces negative temperature anomalies. In contrast with the warm anomalies, the cold anomalies have a minimal impact on the ABF region and their signature is mainly visible along the equator. The transport time series show that during the artificial wind stress strengthening the nSEC/cSEC and EUC transport increases, and that the impact of the wind stress is more evident in the western Atlantic area, i.e. in the area where the artificial wind anomalies were induced.

In order to improve ROMS capability of simulating the seasonal cycle of the equatorial Atlantic, future work could include sensitivity experiments regarding the horizontal resolution and bathymetry interpolation of the model. These sensitivity experiments would provide the optimal horizontal resolution and bathymetry interpolation parameter, required to improve the representation of coastal currents. Finally, another experiment could include the use of realistic surface fluxes and wind stress instead of climatology fields. This could generate a more complete picture of the full capabilities of ROMS regarding the representation of the equatorial Atlantic seasonal cycle and interannual variability, particularly with respect to Benguela Niños and Niñas events.

REFERENCES

Artamonov, Y. V., N. P. Bulgakov and P. D. Lomakin (2002). Intrayear variability of geostrophic zonal currents in the tropical zone of the South Atlantic. *Phys. Oceanogr.*, **12**, NO. 6, 341-352.

Arthur, R. S. (1960). A review of the calculation of the ocean currents at the equator. *Deep-Sea Res.*, **6**, 287-297.

Blanke, B., C. Roy, P. Penven, S. Speich, J. C. McWilliams and G. Nelson (2002). Linking wind and upwelling interannual variability in a regional model of the southern Benguela. *Geophys. Res. Lett.*, **29**, 2188-2191.

Boyer, D.C. and I. Hampton (2001). An overview of the living marine resources of Namibia. *S. Afr. J. Mar. Sci.,* **23**, 5-35.

Brandt, P., F. A. Schott, C. Provost, A. Kartavtseff, V. Hormann, B. Bourlès and J. Fischer (2006). Circulation in the central equatorial Atlantic: Mean and intraseasonal to seasonal variability. *Geophys. Res. Lett.*, **33**, L07609.

Carton, J. A. and B. Huang (1994). Warm events in the tropical Atlantic. *J. Phys. Oceanogr.,* **24**, 888-903.

Carton, J. A., X. Cao, B. S. Giese and A. M. da Silva (1996). Decadal and Interannual SST Variability in the Tropical Atlantic Ocean. *J. Phys. Oceanogr.,* **26**, 1165-1175.

Carton, J. A. and Z. Zhou (1997). Annual cycle of sea surface temperature in the tropical Atlantic Ocean. *J. Geophys. Res.*, **102 (C13)**, 27,813-27,824.

Colberg, F. (2006). An Analysis of Variability in the South Atlantic. *PhD. thesis, Department of Oceanography, University of Cape Town.*

Delcroix, T., M. J. McPhaden, A. Dessier and Y. Gouriou (2005). Time and space scales for sea surface salinity in the tropical oceans. *Deep-Sea Res. I*, **52**, 787-813

Dessier, A. and J. R. Donguy (1994). The sea surface salinity in the tropical Atlantic between 10°S and 30°N – seasonal and interannual variations (1977-1989). *Deep-Sea Res. I*, **41**, 81-100.

Düing, W. P., P. Hisard, E. Katz, J. Meinke, L. Miller, K. V. Moroshkin, G. Philander, A. A. Ribnikov, K. Voigt and R. Weisberg (1975). Meanders and long waves in the equatorial Atlantic. *Nature*, **257**, 280-284.

Florenchie, P., J.R.E. Lutjeharms, C.J.C. Reason, S. Masson and M. Rouault (2003). The source of Benguela Niños in the South Atlantic Ocean. *Geophys. Res. Lett.*, **30**, 12-1 12-4.

Florenchie, P., J.R.E. Lutjeharms, C.J.C. Reason, M. Rouault and C. Roy (2003). Evolution of interannual warm and cold events in the south-east Atlantic Ocean. *J. Climate*, **17**, 2318-2334.

Gammelsrød, T.C., C.H. Bartholomae, D.C. Boyer, V.L.L. Filipe and M.J. O'Toole (1998). Intrusion of warm surface water along the Angolan-Namibian coast in February-March 1995: The 1995 Benguela Niño. *S. Afr. J. Mar. Sci.*, **19**, 41-56.

Gordon, A. L. (1986). Interocean exchange of thermocline water. *J. Geophys. Res.*, **91**, 5037-5046.

Gordon, A. L. and K. T. Bosley (1991). Cyclonic gyre in the tropical South Atlantic. *Deep-Sea Res.*, **38**, Suppl. 1, S323-S343.

Hardman-Mountford, N. J., A. J. Richardson, J. J. Angebag, E. Hagen, L. Nykjaer, F. A. Shillington and C. Villacastin (2003). Ocean Climate of the South East Atlantic observed from satellite data and wind models. *Prog. Oceanog.*. **59**, 181-221.

Hart, T. J. and R. I. Currie (1960). The Benguela Current. *"Discovery" Rep.*, **31**, 123-298.

Hisard, P., C. Henin, R. Houghton, B. Piton and P. Rual (1986). Oceanic conditions in the tropical Atlantic during 1983 and 1984. *Nature* **322**, 243-245.

Horel, J. D., V. E. Kousky and M. T. Kagano (1986). Atmospheric conditions in the Atlantic sector during 1983 and 1984. *Nature* **322**, 248 - 251.

Johns, W. E., T. N. Lee, R. C. Beardsley, J. Candela, R. Limeburner and B. Castro (1998). Annual cycle and variability of the north Brazil current. *J. Phys. Oceanogr.*, **28**, 103-128.

Katz, E. J., S. G. H. Philander and P. L. Richardson (1989). Report on SEQUAL/FOCAL; a study of the equatorial Atlantic ocean. *EOS Trans.,* **70**(2), 18.

Katz, E. J., P. Hisard, J.-M. Verstraete and S. L. Garzoli (1986). Annual change of sea surface slope along the Equator of the Atlantic Ocean in 1983 and 1984. *Nature* **322**, 245 – 247.

Kostianoy, A. G. and J.R.E. Lutjeharms (1999). Atmospherics effects in the Angola-Benguela frontal zone. *J. Geophys. Res.*, **104**, 20, 963-20, 970.

Large, W. G., J. C. McWilliams and S. C. Doney (1994). Oceanic vertical mixing: a review and a model with a non local boundary layer parameterization. *Reviews in Geophysics*, **32**, 363-403.

Lazar, A., R. Murtugudde and A. J. Busalacchi (2001). A model study of temperature anomaly propagation from the subtropics to tropics within the South Atlantic thermocline. *Geophys. Res. Lett.*, **28**, 1271-1274.

Levitus, L. (1986). Annual Cycle of Salinity and salt Storage in the World Ocean. *J. Phys. Oceanogr.*, **16**, 322-343.

Lumpkin, R. and Z. Garraffo (2005). Evaluating the Decomposition of Tropical Atlantic Drifter Observations. *J. Atmos. Oceanic Techn.* **I 22,** 1403-1415.

Lumpkin, R. and S. L. Garzoli (2005). Near-surface circulation in the Tropical Atlantic Ocean. *Deep-Sea Res. I*, **52**, 495-518.

Marchesiello, P., J. C. McWilliams and A. Shchepetkin (2003). Equilibrium structure and dynamics of the California Current System. *J. Phys. Oceanogr.*, **33**, 753-783.

Marchesiello, P., J. C. McWilliams and A. Shchepetkin (2001). Open boundary conditions for a long-term integration of regional oceanic models. *Ocean Modelling*, **3**, 1-21.

Masson, S. and P. Delecluse (2001). Influence of the Amazon river runoff on the tropical Atlantic. *Physics and Chemestry of Earth*, **26**, 137-142.

Mazeika, P. A. (1967). Thermal domes in the eastern tropical Atlantic Ocean. *Limnology and Oceanography*, **12**, 537-539.

Meeuwis, J. M. and J. R. E. Lutjeharms (1990). Surface thermal characteristics of the Angola-Benguela front. *S. Afr. J. Sci.*, **9**, 261-279.

Mercier, H., M. Arhan and J. R. E. Lutjeharms (2003). Upper-layer circulation in the eastern Equatorial and South Atlantic Ocean in January-March 1995. *Deep-Sea Res. I*, **50**, 863-887.

Merle, J. and S. Arnault (1985). Seasonal variability of the surface dynamic topography in the tropical Atlantic Ocean. *J. Mar. Res.*, **43**, 267-288.

Mohrholz, V., M. Schmidt and J. R. E. Lutjeharms (2001). The hydrography and dynamics of the Angola-Benguela Frontal Zone and environment in April 1999. *S. Afr. J. Sci.*, **97**, 199-208.

Molinari, R. L. (1982). Observations of eastward currents in the tropical South Atlantic Ocean. *J. Geophys. Res.*, **87**, 9707-9714.

Monteiro, P. M. S. and A. K. van der Plas (2006). Low Oxygen Water (LOW) Variability in the Benguela System: Key Processes and Forcing Scales Relevant to Forecasting. *In The Benguela: predicting a large marine ecosystem*, Shannon, V., G. Hempel, P. Malanotte-Rizzoli, C. Moloney and J. Woods, eds. Elsevier, Amsterdam, pp. 71-90.

Monteiro, P. M. S., A. K. van der Plas, G. W. Bailey, P. Malanotte-Rizzoli, C. M. Duncombe Rae, D. Byrnes, G. Pitcher, P. Florenchie, P. Penven, J. Fitzpatrick and H. U. Lass (2006). Low oxygen water (LOW) forcing scales amenable to forecasting in the Benguela ecosystem. *In The Benguela: predicting a large marine ecosystem*, Shannon, V., G. Hempel, P. Malanotte-Rizzoli, C. Moloney and J. Woods, eds. Elsevier, Amsterdam, pp. 295-308.

Monteiro, P. M. S., A. K. van der Plas, Mélice, J.-L., Florenchie, P. (2006). Dynamical characteristics of interannual hypoxia variability in a coastal upwelling system: climate and ecosystem state implications. *Submitted to Deep Sea Research.*

Monteiro, P. M. S., A. K. van der Plas, G. W. Bailey and Q. Fidel (2004). Low oxygen variability in the Benguela System: a review and new understanding. *CSIR Report (Internationally Peer Reviewed)*, ENV-S-C 2004-075, 67pp.

Moroshkin, K. V., V. A. Bobnov and R. P. Bulatov (1970). Water circulation in the eastern South Atlantic Ocean. *Oceanology*, **10**, 27-34.

Peterson, R. G., L. Stramma (1991). Upper-level circulation in the South Atlantic Ocean. *Prog. Oceanog.*. **26**, 1-73.

Penven, P., J. R. E. Lutjeharms and P. Florenchie (2006). Madagascar: A pacemaker for the Agulhas Current system?. *Geophys. Res. Lett.*, **33**, L17609.

Penven, P., C. Roy, G. B. Brundrit, A. Colin de Verdière, P. Fréon, A. S. Johnson, J. R. E. Lutjeharms and F. A. Shillington (2001). A Regional hydrodynamic model of the upwelling in the Southern Benguela. *S. Afr. J. Sci.*, **97**, 472-475.

Penven, P., C. Roy, A. Colin de Verdière and J. Largier (2000). Simulation of a coastal jet retention process using a barotropic model. *Oceanologia Acta*, **23** (no. 5), 615-634.

Philander, S. G. H. (1986). Unusual conditions in the tropical Atlantic Ocean in 1984. *Nature*, **322**, 236 – 238.

Philander, S. G. H. and R. C. Pacanowski (1986). A model of the seasonal cycle in the tropical Atlantic Ocean. *J. Geophy. Res.,* **91**, 14,192-14,206.

Pichevin, L., M. Cremer, J. Giraudeau and P. Bertrand (2005). A 190 ky record of lithogenic grain-size on the Namibian slope: Forging a tight link between past wind-strength and coastal upwelling dynamics. *Mar. Geology*. **218**, 81-96.

Reason, C. J. C. (2001). Subtropical Indian Ocean SST dipole events and southern African rainfall. *Geophys. Res. Lett.*. **28**, 2225-2227.

Rahmstorf, S. (2006). Thermocline Ocean Circulation. *In: Encyclopedia of Quartenary Sciences*, edited by S. A. Elias. Elsevier, Amsterdam 2006. pp 10.

Reid, J. L., W. D., Nowlin, Jr. and W. C. Patzert (1977). On the characteristics and Circulation of the Southwestern Atlantic Ocean. *J. Phys. Oceanogr.*, **7**, 62-91.

Reid, J. L. (1989). On the total geostrophic circulation of the South Atlantic Ocean: Flow patterns, tracers and transports. *Prog. Oceanog.*. **23**, 149-244.

Reverdin, G., P. Rual, Y. du Penhoat and Y. Gouriou (1991). Vertical structure of the seasonal cycle in the central equatorial Atlantic Ocean: XTB sections form 1980 to 1988. *J. Phys. Oceanogr.*, **21**, 277-291.

Richardson, P. L. and G. Reverdin (1986). Seasonal cycle of velocity in the Atlantic North Equatorial Countercurrent as measured by surface drifters current meters and ship drift. . *Geophy. Res.*, **92**, 3691-3708.

Rouault, M., P. Florenchie, N. Fauchereau and C. J. C. Reason (2003). South East Atlantic warm events and southern African rainfall. *Geophys. Res. Lett.*. **30**, 8009.

Rouault, M., S. Illig, C. Bartholomae, C. J. C. Reason and A. Bentamy (2007). Propagation and origin of warm anomalies in the Angola Benguela upwelling system in 2001. *J. Mar. Syst., in press.*

Schott, F. A., L. Stramma and J. Fischer (1995). The warm water inflow into the western tropical Atlantic boundary regime, spring 1994. *J. Geophys. Res.*, **100**, 24745-24760.

Schott, F. A., J. Fischer and L. Stramma (1998). Transports and pathways of the upper-layer circulation in the western tropical Atlantic. *J. Phys. Oceanogr.*, **28**, 1904-1928.

Schott, F. A., M. Dengler, P. Brandt, K. Affler, J. Fischer, B. Bourlès, Y. Gouriou, R. L. Molinari and M. Rhein (2003). The zonal currents transports at 35°W in the tropical Atlantic. *Geophys. Res. Lett.*, **30** , NO. 7, 1349.

Schott, F. A., J. Carton, W. Hazeleger, W. Johns, Y. Kushnir, C. Reason and S.-P. Xie (2004). Tropical Atlantic Climate Experiment. *CLIVAR panel white paper* (1^{st} draft). 27 pp..

Shannon, L.V., A.J. Boyd, G.B. Brundrit and J. Taunton-Clark (1986). On the existence of an El Niño-type phenomenon in the Benguela system. *J. Mar. Res.*, **44**, 495-520.

Shannon, L. V. and J. J. Angebag (1987). Some aspects of the physical oceanography of the boundary zone between the Benguela and Angola Current systems. *Colln scient. Pap. Int. Commn SE. Atl. Fish*, **14**(2), 249-261.

Shannon, L. V., J. J. Angebag and M. E. L. Buys (1987). Large and meso-scale features of the Angola-Benguela Front. *S. Afr. J. Mar. Sci.*, **5**, 11-34.

Shannon, L. V. and G. Nelson (1996). The Benguela: large scale feature and processes and system variability. In *The South Atlantic: Present and Past Circulation,* G. Wefer, W. H. Berger, G. Siedler and D. J. Webb, eds. Springer-Berlag, Berlin Heidelberg, pp163-210.

Shchepetkin, A. F. and J. C. McWilliams (2005). The regional oceanic modelling system (ROMS): a split-explicit, free-surface, topography-following-coordinate oceanic model. *Ocean Modelling*. **9**, 347-404.

Shillington, F. A., C. J. C. Reason, C. M. Duncombe-Rae, P. Florenchie and P. Penven (2006). Large scale physical variability of the Benguela Current Large Marine Ecosystem (BCLME). *In The Benguela: predicting a large marine ecosystem*, Shannon, V., G. Hempel, P. Malanotte-Rizzoli, C. Moloney and J. Woods, eds. Elsevier, Amsterdam, pp. 49-70.

Speich, S., J. R. E. Lutjeharms, P. Penven and B. Blanke (2006). Role of bathymetry in Agulhas Current configuration and behavior. *Geophys. Res. Lett.*. **33**, L23611.

Stramma, L., Y. Ikeda and R. G. Peterson (1990). Geostrophic transport in the Brazil Current region north of 20°S. *Deep-Sea Res. I.*

Stramma, L. and F. Schott (1996). Western equatorial circulation and interhemispheric exchange. In: *The Warmwatersphere of the North Atlantiv Ocean*, Krauss, W., eds. Gebr. Borntraeger, Berlin, Stuttgart, pp. 195-227.

Stramma, L. and F. Schott (1999). The Mean flow field of the tropical Atlantic Ocean. *Deep-Sea Res. II.,* **46**, 279-303.

Stramma, L. and M. England (1999). On the water masses and mean circulation of the South Atlantic Ocean. *J. Geophy. Res.,* **104 (C9)**, 20,863-20,883.

Stramma, L., Fischer, J., Brandt, P., Schott, F. (2003). Circulation, variability and near-equatorial meridional flow in the central tropical Atlantic. In *Interhemispheric Water Exchange in the Atlantic Ocean*, Goni, G. J., Malanotte-Rizzoli, P., eds. Elsevier, Amsterdam, pp. 1–22.

Tomczak, M. and J. S. Godfrey (2003). Regional Oceanography: An Introduction, 2nd edition. Daya Publishing House, Dehli, 390pp.

Tsuchiya, M. (1986). Thermostads and circulation in the upper layer of the Atlantic Ocean. *Prog. Oceanog..* **16**, 235-267.

Tyson P. D. (1986). Climate change and Variability in Southern Africa. Cape Town; Oxford University Press: 220 pp.

Veitch, J. A. (2004). Numerical model investigation of near-surface circulation features the Angola Basin. *MSc. thesis, Department of Oceanography, University of Cape Town.*

Veitch, J. A., P. Florenchie, F. A. Shillington (2006). Seasonal and interannual fluctuations of the Angola–Benguela Frontal Zone (ABFZ) using 4.5 km resolution satellite imagery from 1982 to 1999. *International Journal of Remote Sensing*, **27**, Number 05, 987 – 998.

Voituriez, B. (1981). Les sous-courants équatoriaux nord et sud et la formation des dômes thermiques tropicaux. *Oceanologica Acta*, **4**, 497-506.

Voituriez, B. and A. Herbland (1982). Comparaison des systèmes productifs de l'Atlantique Tropical Est: dômes thermiques, upwellings côtiers et upwelling equatorial. *Rapports et Procès-Verbaux des Réunions Conseil International pour l'Exploration de la Mer*, **180**, 114-130.

Wacongne, S. and B. Piton (1992). The near-surface circulation in the northeastern corner of the South Atlantic ocean. *Deep-Sea Res.*, **7/8**, 1273-1298.

Weisberg, R. H. and C. Colin (1986). Equatorial Atlantic Ocean temperature and current variations during 1983 and 1984. *Nature* **322**, 240 – 243.

Wilson, W. D., E. Johns, R. L. Molinari (1984). Upper layer circulation in the western tropical North Atlantic Ocean during August 1989. *J. Geophy. Res.,* **99**, 22,513-22,523.

Yoo, J.-M. and J. A. Carton (1990). Annual and Interannual Variation of the Freshwater Budget in the Tropical Atlantic Ocean and the Caribbean Sea. *J. Phys. Oceanogr.*, **20**, 831-845.

http://www.aoml.noaa.gov/phod/dac/drifter_climatology.html

http://www.brest.ird.fr/Roms_tools/

http://www.cdc.noaa.gov/cdc/data.noaa.oisst.v2.html

http://www.nodc.noaa.gov/OC5/WOA01/pr_woa01.html

http://seis.sea.uct.ac.za/index.php